



Terms and Conditions of Use of Digitised Theses from Trinity College Library Dublin

Copyright statement

All material supplied by Trinity College Library is protected by copyright (under the Copyright and Related Rights Act, 2000 as amended) and other relevant Intellectual Property Rights. By accessing and using a Digitised Thesis from Trinity College Library you acknowledge that all Intellectual Property Rights in any Works supplied are the sole and exclusive property of the copyright and/or other IPR holder. Specific copyright holders may not be explicitly identified. Use of materials from other sources within a thesis should not be construed as a claim over them.

A non-exclusive, non-transferable licence is hereby granted to those using or reproducing, in whole or in part, the material for valid purposes, providing the copyright owners are acknowledged using the normal conventions. Where specific permission to use material is required, this is identified and such permission must be sought from the copyright holder or agency cited.

Liability statement

By using a Digitised Thesis, I accept that Trinity College Dublin bears no legal responsibility for the accuracy, legality or comprehensiveness of materials contained within the thesis, and that Trinity College Dublin accepts no liability for indirect, consequential, or incidental, damages or losses arising from use of the thesis for whatever reason. Information located in a thesis may be subject to specific use constraints, details of which may not be explicitly described. It is the responsibility of potential and actual users to be aware of such constraints and to abide by them. By making use of material from a digitised thesis, you accept these copyright and disclaimer provisions. Where it is brought to the attention of Trinity College Library that there may be a breach of copyright or other restraint, it is the policy to withdraw or take down access to a thesis while the issue is being resolved.

Access Agreement

By using a Digitised Thesis from Trinity College Library you are bound by the following Terms & Conditions. Please read them carefully.

I have read and I understand the following statement: All material supplied via a Digitised Thesis from Trinity College Library is protected by copyright and other intellectual property rights, and duplication or sale of all or part of any of a thesis is not permitted, except that material may be duplicated by you for your research use or for educational purposes in electronic or print form providing the copyright owners are acknowledged using the normal conventions. You must obtain permission for any other use. Electronic or print copies may not be offered, whether for sale or otherwise to anyone. This copy has been supplied on the understanding that it is copyright material and that no quotation from the thesis may be published without proper acknowledgement.

Modification and Analysis of Layered Materials with Charged Particle Beams

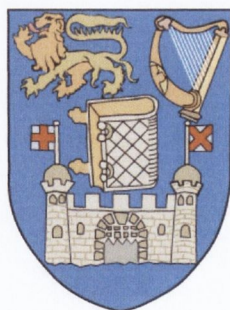
*A thesis submitted in fulfilment of the requirements
for the degree of Doctor of Philosophy*

in the

School of Physics

TRINITY COLLEGE DUBLIN

2014

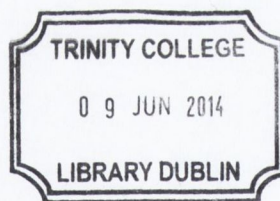


Author:

Daniel FOX

Supervisor:

Dr. Hongzhou ZHANG



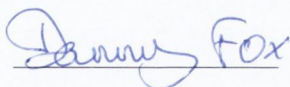
Thesis 10385

Declaration

I declare that this thesis has not been submitted as an exercise for a degree at this or any other university and it is entirely my own work.

I agree to deposit this thesis in the University's open access institutional repository or allow the library to do so on my behalf, subject to Irish Copyright Legislation and Trinity College Library conditions of use and acknowledgement.

Elements of this work that have been carried out jointly with others or by collaborators have been duly acknowledged in the text wherever included.

A handwritten signature in blue ink that reads "Daniel Fox". The signature is written in a cursive style with a horizontal line underneath the name.

Daniel Fox

Summary

In this work a range of highly focused charged particle beams were used to modify the structure and geometry of materials. Recently discovered two-dimensional (2D) materials were the focus of the work. Fundamental studies on the beam-sample interactions were conducted. This knowledge was then used to achieve nanoscale control of the modification.

Graphene consists of a single atomic layer of carbon in a hexagonal lattice. It was first isolated in 2004[1] and has since been the focus of an intense research effort[2] due to its unique properties. A low-energy electron beam was used to etch carbon atoms from a graphene sample in a nitrogen environment. The etching was observed to produce nanopores within the graphene. The localised generation of nanopores in graphene can be used for gas filtration[3], hydrogen storage[4] or DNA sequencing[5].

A direct modification approach was developed using a sub-nanometre beam of helium ions. This beam has only been made available by the recently developed helium ion microscope[6]. The helium ions were found to produce defects in the graphene structure. The relationship between the ion irradiation and the structural modification was studied by Raman spectroscopy. The beam was also shown to be capable of removing material from the graphene with nanometre precision. Nanostructures such as ribbons were produced. The isolation of graphene into nanoribbons is a known means to tailor its electronic band structure[7].

The technique of nanostructuring by a helium ion beam was extended to another 2D material, molybdenum disulfide (MoS_2). This material also exhibits unique properties when isolated at the nanoscale[8]. A model for the milling process was used to determine the values of the experimental parameters required. The model was found to agree very well with the experimental data. Milling was demonstrated on the MoS_2 . The edge structure of the milled features has a strong influence on their properties. Scanning transmission electron microscopy (STEM) was used to determine the extension of the damage from the milled edges. Under optimised milling conditions no damage was observed at the fabricated edges. A well-defined edge could be created.

Helium ion beam fabricated holes in MoS_2 flakes were filled with carbon. The electron beam within a transmission electron microscope (TEM) was used to deposit the carbon into the holes. The beam was then used to anneal the carbon to crystallize its structure. This technique can be used to create a range of heterostructures with unique properties.

The ion beam induced modification was then extended to a 3D sample. A gallium ion beam was used to demonstrate the arbitrary geometries into which a sample can be patterned. The fabrication of a thin sample for TEM analysis was used as an example. A helium ion beam was then used to further control the geometry and surface structure of the sample. The combination of the two beams facilitates both the micro and nanoscale structuring and modification of a broad range of materials.

Abstract

Modification and Analysis of Layered Materials with Charged Particle Beams

Daniel Fox

In this work the controlled modification of 2D nanomaterials in order to tune their structure and control their geometry was demonstrated. This was achieved using a range of highly focused beams of electrons and ions.

The localised generation of nanopores within a sample using electron-beam activated gas etching was first described. The material used was graphene, a honeycomb lattice of carbon just one atom thick. A model of the etching was developed. Systematic investigations of the effect of the various parameters in the system were used to support the model. Structural modification of graphene was then demonstrated using a focused beam of helium ions (He^+). Raman spectroscopy was used to correlate the ion irradiation parameters with the sample damage. It was found that a desired density of defects can be introduced into graphene by this method. He^+ irradiation was also shown to be capable of fabricating nanostructures within graphene flakes.

The He^+ fabrication was then extended to thin (<3 layer) flakes of molybdenum disulfide (MoS_2). The irradiation of MoS_2 was modelled and this data was used to design an experiment. The experiment showed that nanostructures can be milled into these flakes. The damage produced at the edges of the milled features was investigated by high resolution scanning transmission electron microscopy (STEM). It was found that the extent of the damage can be controlled such that no observable edge damage was created. The nanostructures milled within the MoS_2 flakes were then filled with carbon and annealed with an electron beam. This shows that it is possible to use this technique to create unique new heterostructures.

Finally, the ion beam-induced modification technique was extended to a 3D material system. A focused beam of gallium ions was used to tailor the geometry of a section of silicon. This was shown to have applications in the preparation of samples for transmission electron microscopy (TEM). A He^+ beam was then used to provide further sample modification control, producing samples that reveal smaller feature sizes during TEM observation and less beam-induced damage than can be achieved by a gallium ion beam alone.

Publications

1. **D. Fox**, Y. B. Zhou, A. O'Neill, S. Kumar, J. J. Wang, J. N. Coleman, G. S. Duesberg, J. F. Donegan and H. Z. Zhang. Helium ion microscopy of graphene: beam damage, image quality and edge contrast. *Nanotechnology*, 24:335702, 2013.
2. **D. Fox**, A. O'Neill, D. Zhou, M. Boese, J. N. Coleman, and H. Z. Zhang. Nitrogen assisted etching of graphene layers in a scanning electron microscope. *Applied Physics Letters*, 98(24):243117-3, 2011.
3. **D. Fox**, Y. Chen, C. C. Faulkner, and H. Zhang. Nano-structuring, surface and bulk modification with a focused helium ion beam. *Beilstein Journal of Nanotechnology*, 3:579-585, 2012.
4. **D. Fox**, R. Verre, B. J. O'Dowd, S. K. Arora, C. C. Faulkner, I. V. Shvets, and H. Z. Zhang. Investigation of coupled cobalt & silver nanoparticle system by plan view TEM. *Progress in Natural Science: Materials International*, 22(3): 186-192, 2012.
5. **D. Fox** and H. Z. Zhang. *Progress in Nanoscale Characterization and Manipulation*, Helium ion microscopy. Book chapter, *In Press*.
6. **D. Fox**, Y. Zhou and H. Z. Zhang. *Functional Nanotubes and Nanosheets*, Helium-ion microscopy for graphene characterisation and modification. Book chapter, *In Press*.

7. S. Bagheri-Kazemabad, **D. Fox**, Y. Chen, L. M. Geever, A. Khavandi, R. Bagheri, C. L. Higginbotham, H. Z. Zhang and B. Chen. Morphology, rheology and mechanical properties of polypropylene/ethylene–octene copolymer/clay nanocomposites: Effects of the compatibilizer. *Composites Science and Technology*, 72(14):1697-1704, 2012.
8. D. McCloskey, **D. Fox**, N. O'Hara, V. Usov, D. Scanlan, N. McEvoy, G. S. Duesberg, G. L. W. Cross, H. Z. Zhang, J. F. Donegan. Helium ion microscope generated nitrogen-vacancy centres in type Ib diamond. *Applied Physics Letters*, 104(3):031109, 2014.
9. Y. Chen, H. Z. Zhang, **D. Fox**, C. C. Faulkner, D. Jeng and M. Bari. Microstructural and chemical variation of TiO₂ electrodes in DSSCs after ethanol vapour treatment. *Materials Science and Engineering: B*, 178(1):71-76, 2013.
10. K. Wang, J. Wang, J. Fan, M. Lotya, A. O'Neill, **D. Fox**, Y. Feng, X. Zhang, B. Jiang, Q. Zhao, H. Z. Zhang, J. N. Coleman, L. Zhang and W. J. Blau. Ultrafast saturable absorption of two-dimensional MoS₂ nanosheets. *ACS Nano*, 7(10):9260, 2013.
11. H. Luo, R. Wang, Y. Chen, **D. Fox**, R. O'Connell, J. J. Wang and H. Z. Zhang. Enhanced photoluminescence from SiO_x-Au nanoflowers. *CrystEngComm*, 15:10116, 2013.
12. R. Verre, K. Fleischer, J. F. McGilp, **D. Fox**, G. Behan, H. Zhang, and I. V. Shvets. Controlled in situ growth of tunable plasmonic self-assembled nanoparticle arrays. *Nanotechnology*, 23(3):035606, 2012.
13. M. J. Santos-Martinez, I. Inkielewicz-Stepniak, C. Medina, K. Rahme, D. M. D'Arcy, **D. Fox**, J. D. Holmes, H. Z. Zhang, and M. W. Radomski. The use of quartz crystal microbalance with dissipation (QCM-D) for studying nanoparticle-induced platelet aggregation. *International Journal of Nanomedicine*, 2012(7):243-255, 2012.

-
14. R. Verre, M. Modreanu, O. Ualibek, **D. Fox**, K. Fleischer, C. Smith, H. Z. Zhang, M. Pemble, J. F. McGilp and I. V. Shvets. General approach to the analysis of plasmonic structures using spectroscopic ellipsometry. *Physical Review B*, 87:235428, 2013.
 15. R. Verre, R. G. S. Sofin, V. Usov, K. Fleischer, **D. Fox**, G. Behan, H. Z. Zhang and I. V. Shvets. Equilibrium faceting formation in vicinal Al_2O_3 (0001) surface caused by annealing. *Surface Science*, 606(23-24):1815-1820, 2012.

Acknowledgements

First and foremost I would like to express my sincere gratitude to my supervisor Prof. Hongzhou Zhang for his guidance and supervision. Your inspiring words, and especially your critical comments, have been instrumental in shaping my progress over the past four years.

I would like to thank Dr. Gavin Behan, Dr. Markus Boese, Dr. Colm Faulkner, Mr. Clive Downing, Dr. Jing Jing Wang, Dr. Alan Bell, Mr. Dermot Daly and Mr. Cathal McAuley for helping me to gain the practical skills and knowledge required throughout my PhD.

Many members have come and gone through our research group over the years. I would like to thank all of these people for their support and encouragement: Ms. Dan Zhou, Ms. Yanhui Chen, Mr. Abbas Khalid, Mr. Robert O'Connell, Dr. Yangbo Zhou, Mr. Pierce Maguire and Mr. Junfeng Zhou. The contribution to this work and to our group in general by many visiting and summer students is also greatly appreciated.

I would like to thank Prof. Igor Shvets, Prof. Jonathan Coleman and Dr. Arlene O'Neill for their contributions to this work. Arlene has been a wonderful collaborator for the past four years and her unwavering enthusiasm is nothing short of remarkable.

I would like to thank the members of Prof. Nicolosi's group for their contributions to this work, whether providing assistance at a microscope, or insight in our office. Finally I would like to thank my family for all of their support and love over the years.

Contents

Declaration	ii
Summary	iv
Abstract	vii
Publications	viii
Acknowledgements	xii
List of Figures	xix
List of Tables	xxi
List of Abbreviations	xxiii
1 Introduction	1
1.1 Introduction and Motivation	1
1.2 Outline of Thesis	2
2 Layered Two-Dimensional Materials	5
2.1 Overview of Layered 2D Materials	5
2.1.1 Graphene	5
2.1.2 Molybdenum Disulfide & Other 2D Materials	7
2.2 Production of Graphene	8
2.2.1 Mechanical Exfoliation	8
2.2.2 Epitaxy and Chemical Vapour Deposition	10
2.2.3 Liquid Phase Exfoliation	11
2.3 Properties of Graphene	12
2.4 Applications of Graphene	14

2.5	Modification of Graphene	15
2.5.1	Tuning the Transport Properties	16
2.5.2	Tailoring the Geometry	17
2.5.3	Graphene Nanoribbons	19
2.5.3.1	Chemical Production of GNRs	20
2.5.3.2	Physical Production of GNRs	24
3	Modification Methodologies	29
3.1	Focused Electron Beam	30
3.1.1	Beam-Sample Interaction	30
3.1.2	Low Energy E-beam Activated Gas Etching	33
3.1.2.1	Control of the E-beam Modification	37
3.2	Focused Gallium Ion Beam	39
3.2.1	Beam-Sample Interaction	39
3.2.2	Control of the Gallium Ion Beam Milling	39
3.3	Focused Helium Ion Beam	41
3.3.1	Beam-Sample Interaction	41
3.3.2	Helium Ion Beam Milling	45
3.3.2.1	Control of the Ion Beam Milling	47
4	Characterisation Techniques	51
4.1	Scanning Electron Microscopy	52
4.1.1	Transmission SEM	54
4.2	Transmission Electron Microscopy	55
4.2.1	Scanning Transmission Electron Microscopy	58
4.2.2	Electron Energy Loss Spectroscopy	59
4.2.3	Energy-Dispersive X-ray Spectroscopy	61
4.3	Helium Ion Microscopy	62
4.4	Raman Spectroscopy	63
5	Gas Assisted E-beam Etching of Graphene	67
5.1	Etching Experiment	67
5.2	Results and Analysis of the Etching Process	68
5.2.1	Temperature Effect	80
5.2.2	Gas Assisted E-beam Etching of MoS ₂	82
6	Graphene Imaging & Modification with a Helium Ion Beam	85
6.1	Defect Density vs. He ⁺ Dose	86
6.1.1	Defects vs. Dose Experiment	86
6.1.2	Defects vs. Dose Results	87
6.2	Image Quality vs. He ⁺ Dose	91
6.2.1	Image Quality vs. Dose Experiment	91
6.2.2	Image Quality vs. Dose Results	92

6.3	HIM Imaging vs. SEM and STEM	94
6.3.1	Image Contrast Experiment	94
6.3.2	Image Contrast Results	94
6.4	Graphene Nanoribbon Fabrication	96
6.4.1	GNR Experiment	96
6.4.2	GNR Results	96
7	Milling & Refilling of MoS₂ Nanoflakes	101
7.1	Helium Ion Milling	102
7.1.1	Milling Dose Calculation	102
7.1.2	Ion Milling Experiment	104
7.1.3	Results and Analysis of Ion Milling	105
7.1.4	Outstanding Issues	107
7.2	E-beam Annealing	109
7.2.1	Annealing Dose	109
7.2.2	Annealing Experiment	110
7.2.3	Results and Analysis of Annealing	111
8	3D Sample Modification With Focused Ion Beams	115
8.1	FIB Preparation of TEM Lamellae	117
8.1.1	Plan View Lift-Out	117
8.1.2	Cross Section vs. Plan View Results	120
8.2	HIM Modification of Silicon Lamella	123
8.2.1	Results and Analysis of Silicon Modification	124
9	Conclusion & Future Work	135
A	Tool Specifications	139
B	Source Building Procedure for the Helium Ion Microscope	141
B.1	Forming a Trimer	142
B.2	Aligning the Upper Column	144
B.3	Aligning the Lower Column	145
C	FIB Lift-Out Procedure	147
	Bibliography	151

List of Figures

2.1	The allotropes of carbon.	6
2.2	MoS ₂ structure.	7
2.3	Graphene flakes prepared by different methods.	9
2.4	Graphene's dispersion relation.	13
2.5	Etching of graphene	18
2.6	Graphene nanopores	19
2.7	Graphene nanoribbon edge orientations.	20
2.8	Unzipping of a carbon nanotube.	22
2.9	Graphene nanoribbons.	25
3.1	Electron beam energy simulations.	32
3.2	Electron beam simulations in different Z.	32
3.3	N ₂ ionisation vs. E-beam energy.	35
3.4	Gallium ion interaction volume.	40
3.5	Different energy helium ions in a carbon sample.	41
3.6	Helium ions in different Z samples.	42
3.7	Interaction volumes in SEM and HIM.	42
3.8	Stopping power versus energy.	43
3.9	Stopping power versus velocity.	44
3.10	Electronic and nuclear stopping power.	45
3.11	Range and damage production depth.	45
3.12	The helium ion microscope column.	48
3.13	HIM Irradiation of Graphene Illustration.	49
3.14	Scanning strategy.	50
4.1	SEM interaction volume.	53
4.2	TEM illumination system.	56
4.3	TEM projection system.	57
4.4	EELS spectrum.	60
4.5	Secondary electron energies in HIM.	63
4.6	Raman spectra of different thicknesses of graphene.	65
4.7	Raman spectra of defective graphene.	65
5.1	Graphene etching in SEM.	70

5.2	Etching rate versus nitrogen gas pressure graph.	71
5.3	Etching versus dwell time graph.	72
5.4	Etching rate versus beam current graph.	72
5.5	Etching rate versus beam energy.	73
5.6	N ₂ ionisation cross section versus beam energy fitting.	76
5.7	Etching rate versus beam energy fitting.	78
5.8	TEM images of etched graphene.	79
5.9	Illustration of graphene etching process.	80
5.10	Temperature Dependence of Graphene Etching.	82
5.11	MoS ₂ Etching.	83
6.1	CVD graphene residual contamination.	87
6.2	Raman spectra of He ⁺ irradiated graphene.	89
6.3	I _D vs I _G ratio vs log of dose.	90
6.4	SRIM simulation.	91
6.5	HIM images of graphene.	93
6.6	SEM, STEM and HIM images of graphene.	95
6.7	HIM Fabricated Graphene Nanoribbons.	97
6.8	GNR Fabrication Issues.	98
7.1	MoS ₂ Milling	106
7.2	Arbitrary Milling Directions and Nanoribbons	107
7.3	Outstanding Milling Issues	108
7.4	Filling and Annealing of an MoS ₂ flake	112
8.1	SEM of Al ₂ O ₃ Sample.	118
8.2	Plan View Sample Preparation.	119
8.3	Cross Section Sample Results.	121
8.4	Plan View Sample Results.	122
8.5	HIM Modification of Silicon Lamella.	126
8.6	HRTEM and Diffraction of Silicon.	127
8.7	HIM modification of tilted silicon lamella.	129
8.8	TEM of HIM modification.	130
8.9	Silicon thickness map.	131
8.10	EELS and HRTEM of HIM modified silicon	132
B.1	HIM Trimer.	143
C.1	Cross Section Sample Preparation.	148

List of Tables

2.1	Graphene production techniques.	12
5.1	Nitrogen ionisation cross-section values.	75
8.1	Preparation methods used on the two Si samples.	124
A.1	Tool Specifications.	140

List of Abbreviations

2D	Two-Dimensional
AFM	Atomic Force Microscope
BN	Boron Nitride
CCD	Charge-Coupled Device
CVD	Chemical Vapour Deposition
DNA	DeoxyRibonucleic Acid
EBL	Electron Beam Lithography
EDX	Energy-Dispersive X-ray Spectroscopy
EELS	Electron Energy Loss Spectroscopy
ELNES	Energy-Loss Near-Edge Structure
EXELFS	EXtended Energy-Loss Fine Structure
FET	Field-Effect Transistor
FFT	Fast Fourier Transform
FIB	Focused Ion Beam
GFIS	Gas Field Ion Source
GIS	Gas Injection System
GNR	Graphene NanoRibbon
HAADF	High-Angle Annular Dark-Field
HIL	Helium Ion Lithography
HIM	Helium Ion Microscope
HSQ	Hydrogen SilsesQuioxane
IPA	IsoPropAnol

ITO	I ndium T in O xide
ITRS	I nternational T echnology R oadmap for S emiconductors
LED	L ight- E mitting D iode
LMIS	L iquid M etal I on S ource
MoS₂	M olybdenum D isulfide
MoSe₂	M olybdenum D iselenide
MoTe₂	M olybdenum D itelluride
NbSe₃	N iobium T riselenide
PMMA	P oly(M ethyl M eth A crylate)
RPM	R evolutions P er M inute
SAED	S electe d A rea E lectron D iffraction
SEM	S canning E lectron M icroscope
SiO₂	S ilicon D ioxide
STEM	S canning T ransmission E lectron M icroscope
STM	S canning T unnelling M icroscope
TEM	T ransmission E lectron M icroscope
TMD	T ransition M etal D ichalcogenide
WS₂	T ungsten D isulfide
WSe₂	T ungsten D iselenide
ZLP	Z ero L oss P eak

Chapter 1

Introduction

1.1 Introduction and Motivation

The goal of this work is to controllably modify the structure and geometry of materials at the nanoscale. The materials which will be focused on are those with a layered structure. When isolated in single or few layer stacks these materials are considered two-dimensional, being no more than a few atoms thick. The first, and most widely studied, of these materials is graphene, a single layer of carbon atoms. Tuning of the structure of materials can be used to control their properties[9]. For example, tuning of the electronic charge carrier density, or the electronic band gap in graphene would facilitate its use in electronic devices[10].

Controlling the extent of the modification as well as confining the modification within a nanoscale area are currently the main challenges. In this work the feasibility of using focused beams of electrons and ions for this purpose will be investigated. The ability to probe materials with nanometre, and in some cases atomic, spatial resolution is already available in electron and ion beam microscopes. These beams can be used to modify materials using the strong beam-sample interactions occurring, as well as for imaging and analysis. They can be used to introduce a well-defined density of defects within a nanoscale region of the sample. They can

also be used to directly remove material from the sample, enabling the isolation of nanostructures.

The ability of these beams to modify the structure and geometry of two-dimensional materials with the high level of control that is required remains to be investigated. The modification of layered material systems with various types of charged particle beams has yet to be explored and optimised. The current understanding of the beam-sample interaction will be developed through modelling, simulation and experimentation. This knowledge will then be used to demonstrate state of the art modification of recently isolated layered materials.

1.2 Outline of Thesis

This thesis begins in chapter two with an introduction to the materials which feature throughout this work. Their unique properties, production methods and previously attempted modification techniques will be described. The reason these materials were selected will be made clear after reading this chapter.

The third chapter describes the modification techniques selected. The interaction of the various beams within a sample, as well as the theory of the modification mechanism will be presented. The use of focused beams of charged particles for the modification of the selected materials will be justified within this chapter.

Next is a chapter on the various characterisation techniques used to assess the extent of modification of the samples. The characterisation achievable by each technique, specifically in relation to our samples, will be described.

The fifth chapter is the first of the experimental chapters. It details our work on the nanostructuring of graphene with a low-energy electron beam. The effect of various parameters within the system, such as those of the beam or the gas environment, will be established. The physical process occurring will then be described.

The tailoring of graphene's properties and structure are next demonstrated using a focused beam of helium ions. The level of control achievable will be established. The imaging capabilities of various focused beam techniques will also be compared.

In the seventh chapter milling of molybdenum disulfide with a helium ion beam will be investigated. The effect of the milling on the edge structure of the molybdenum disulfide will be analysed. The ability to fill a milled hole in the sample with carbon, and then to crystallize the carbon will also be assessed.

In the final experimental chapter the extension of ion beam modification to three-dimensional material systems will be explored. Novel applications of ion beam milling will be demonstrated.

The last chapter presents the conclusions of the work undertaken in this thesis. The future work which remains to be done will also be discussed, outlining the challenges which future research must attempt to overcome.

Chapter 2

Layered Two-Dimensional Materials

In this chapter we will introduce graphene and molybdenum disulfide. Both of these are layered materials which can be isolated as single layers. An overview of relevant research based on the materials will be presented including their production, properties and applications. Our discussion will be focused on the most widely researched and the best understood of the two-dimensional (2D) materials, graphene, with a brief introduction to MoS₂.

2.1 Overview of Layered 2D Materials

2.1.1 Graphene

Graphene, the two-dimensional carbon allotrope, can be thought of as the basis of the other sp^2 carbon materials as shown in figure 2.1. In this allotrope three σ bonds per atom are formed resulting in a planar hexagonal structure. The remaining p orbital electron overlaps with adjacent p orbitals to form an out of plane π bond. The primitive lattice vectors, a_1 and a_2 are shown in figure 2.1(a).

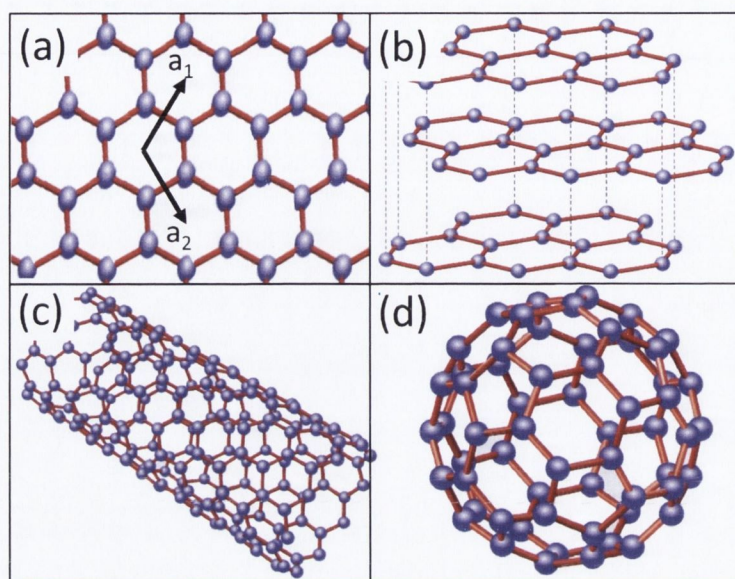


FIGURE 2.1: The allotropes of carbon. (a) is graphene, the lattice constant a (0.246 nm) is shown. (b) is graphite. (c) is a single-walled carbon nanotube and (d) is a buckyball. Figure adapted from [12].

The hexagonal lattice constant, a , where $a = |a_1| = |a_2|$, is equal to 0.246 nm. The C–C bond length is 0.142 nm.

These two dimensional hexagonal sheets of carbon are AB stacked and held together by weak van der Waals forces to form graphite, figure 2.1(b). Furthermore, fullerenes can be produced by rolling graphene up to form one dimensional nanotubes, figure 2.1(c). By introducing non-hexagonal member rings it can also be wrapped up into a sphere to produce zero dimensional buckyballs, figure 2.1(d) [11].

Zero and one-dimensional carbon allotropes were discovered in 1985 [13] and 1991 [14], respectively. At this time graphene was thought not to be a stable structure. It was not until 2004 when Novoselov, Geim *et al.* [1] conclusively demonstrated not only that isolating single layers of graphite was possible, but also that this novel 2D material had some remarkable properties which deviate from those of its bulk counterpart graphite. Throughout the years after their discovery the fullerenes were the subject of widespread research, with carbon nanotubes being heralded

as a potential component in a range of next generation devices[15]. With the discovery of graphene a new wonder material was born and an explosion in graphene research followed. In less than ten years there have been over 25,000 publications on the topic of graphene. Graphene is the second material in its family to earn its discoverer a Nobel prize.

2.1.2 Molybdenum Disulfide & Other 2D Materials

Transition metal dichalcogenides (TMDs) are a family of materials which consist of a transition metal atom sandwiched between two chalcogen atoms. These layers are then stacked and bound by van der Waals forces. The properties of the layered materials vary widely, they can be semiconducting, semimetallic or metallic.

Molybdenum disulfide (MoS_2) is one of the most interesting of these materials. MoS_2 has a trigonal prismatic structure with a monolayer height of 0.68 nm[16] (see figure 2.2). The hexagonal lattice constant, a , is equal to 0.316 nm and the out of plane lattice parameter, c , is equal to 1.258 nm. The unit cell is constructed from two layers due to the out of plane stacking order. Out of plane, MoS_2 stacks AbA, BaB where A and B are sulfur atoms and a and b are Molybdenum atoms.

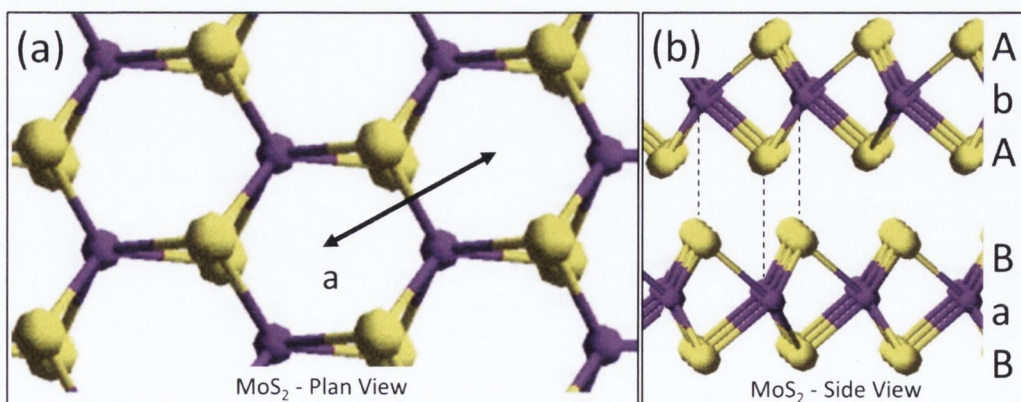


FIGURE 2.2: (a) A layer of molybdenum disulfide shown in plan view. The distance to which the lattice constant a (0.316 nm) refers is shown. (b) A cross-section view of two MoS_2 layers showing the stacking order. The yellow atoms are sulfur and the purple atoms are molybdenum[16].

Bulk MoS₂ is an indirect band gap semiconductor with a band gap of 1.2 eV. However, when isolated as a single layer MoS₂ becomes a direct gap semiconductor with a band gap of 1.8 eV[17]. Few layer MoS₂ can be probed by Raman spectroscopy, with the spectrum showing a strong dependence on the layer thickness[18]. 2D MoS₂ can be produced by the same methods as graphene such as mechanical exfoliation, Chemical Vapour Deposition (CVD) or liquid phase exfoliation.

Monolayer MoS₂ does not possess the mobility of graphene. However, it does have an electronic band gap. Due to this band gap electronic devices with large on/off ratios of 1×10^8 have been demonstrated[17]. Single layer MoS₂ transistors can produce devices with ultra-low power use in the off state. Monolayer MoS₂ is also promising for optoelectronic devices due to its direct band gap[19].

The other semiconducting TMDs which can be exfoliated to single layers include molybdenum diselenide (MoSe₂), molybdenum ditelluride (MoTe₂), tungsten disulfide (WS₂) and tungsten diselenide (WSe₂)[20–22]. An insulating 2D material exists in the form of BN and NbSe₃ is a metal[23].

The rest of this section focuses on the production, properties and applications of 2D materials with graphene used as an example.

2.2 Production of Graphene

2.2.1 Mechanical Exfoliation

When graphene was initially discovered by Novoselov *et al.*[1] in 2004 it was produced by the *mechanical exfoliation* of graphite onto silicon substrates with a 300 nm SiO₂ layer. The surface oxide provides both an electrically isolating layer, and also a means to identify single layer graphene under an optical microscope. An image of a large, single layer, single crystal, mechanically exfoliated graphene flake

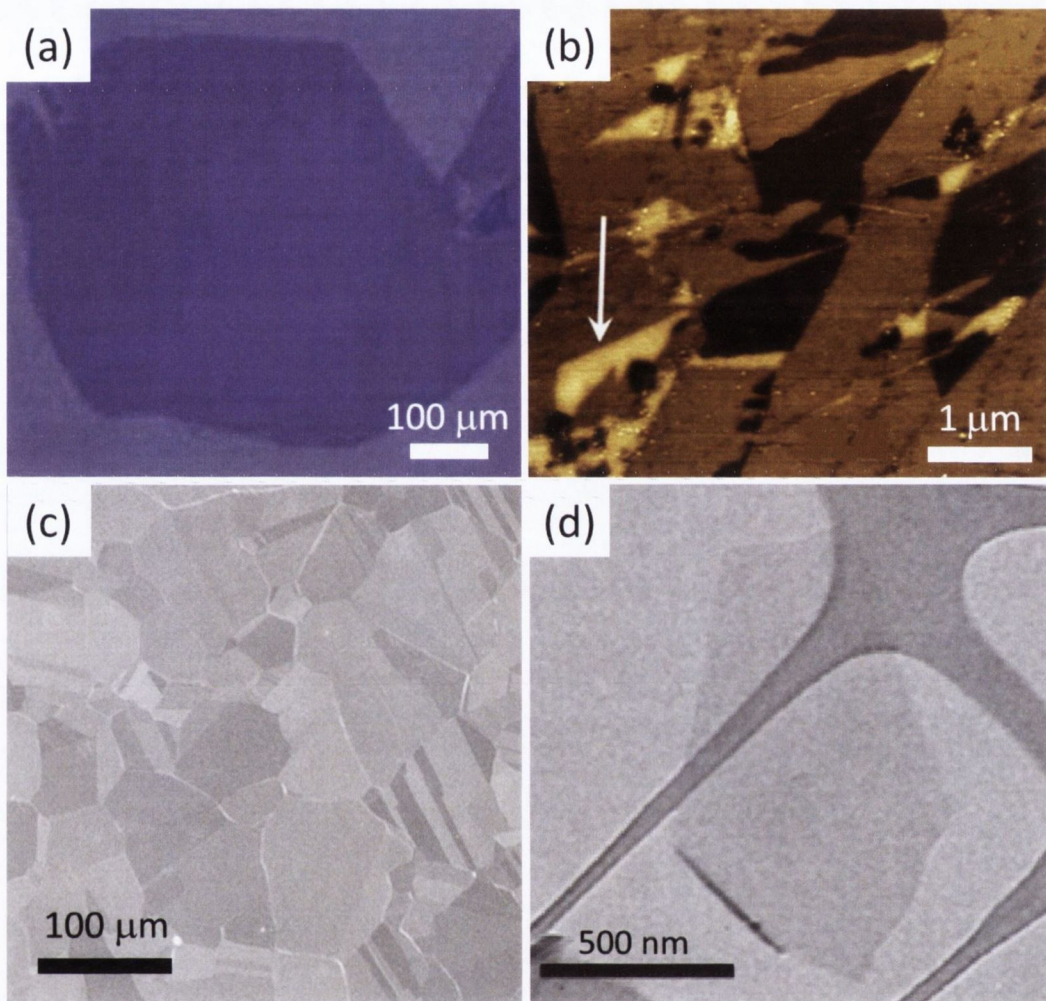


FIGURE 2.3: (a) An optical micrograph of mechanically exfoliated graphene flake[24]. (b) Electrostatic force microscopy phase image showing the different layer thicknesses and typical domain sizes achieved by epitaxial growth of graphene on SiC[25]. The arrow shows a bright area which indicates single layer graphene. (c) An SEM image of a CVD graphene flake with many different domains[26]. (d) A TEM image of a graphene flake suspended on a carbon support film. The flake was produced by liquid phase exfoliation[27].

is shown in figure 2.3(a). The colour of the sample is shifted from violet-blue to blue by the presence of a layer of graphene on the surface.

The process known as mechanical exfoliation is the peeling of graphite flakes from bulk graphite with scotch tape until single layers remain. This graphene preparation process is simple and affordable and it can be used to produce large (typically tens of μm) high quality flakes. The combination of these factors facilitated the

widespread adoption of graphene based research. However, the yield of single layer flakes is low. This process is time consuming and is not scalable for device integration.

2.2.2 Epitaxy and Chemical Vapour Deposition

Heating of silicon carbide at over 1,100 °C in low pressure ($\sim 100 \mu\text{Pa}$) can be used to grow graphene epitaxially. The properties of this type of graphene are almost as good as mechanically exfoliated graphene[28]. However it is challenging to achieve large graphene domains with uniform thickness[25]. Figure 2.3(b) shows the variation of layer thicknesses typically achieved. The growth environment and the substrate cost are also limiting factors to the widespread adoption of this production method.

A similar epitaxial graphene growth method is done on metal substrates by CVD. This process can produce large, high quality graphene sheets. By using copper foil and low pressure methane a self-limiting process is employed whereby very large, single layer graphene layers can be grown[29]. A CVD graphene flake is shown in figure 2.3(c). The size of a single crystal domain within the CVD graphene layer is typically tens of microns. The CVD method is making rapid progress, such as lower growth temperatures[30], which make it viable for electronic device applications.

These CVD graphene sheets can be transferred to an arbitrary substrate[31]. A polymer is first spin coated onto the graphene surface. The metal substrate is then chemically etched away. The graphene is placed onto a new substrate and finally the polymer is dissolved in solvent. This transfer process allows graphene grown on metal substrates during the CVD process to be transferred to electrically insulating substrates. The graphene can then be contacted to build electronic devices. The transfer process does have some limitations. The use of polymers and

solvents introduces contamination onto the graphene. Most of the contamination is removed by heating after the transfer process, but some will always remain.

2.2.3 Liquid Phase Exfoliation

The final graphene preparation method that will be discussed here is liquid phase exfoliation of bulk graphite. In this method graphite is ultrasonicated in solvents with solubility parameters within a defined range[32]. The solvent has a surface tension that favours an increase in the total area of graphite crystallites. This results in the graphite being exfoliated down to few-layer and single-layer graphene[27, 33]. Larger graphite pieces remain in the solution, but these can be separated out by centrifugation. The surface energy matching between the solvent and the solute stabilises the solution against re-aggregation[34].

Liquid phase exfoliation of graphite has been extended to high concentration dispersions and to high volume dispersions on an industrial scale of hundreds of litres[35]. The liquid phase exfoliation of graphene was also extended to a range of layered materials in 2011 by Coleman *et al.*[23]. This opened the field of graphene research up to many new 2D materials.

This method of graphene preparation certainly has numerous advantages over the other methods discussed, such as cost and scalability, however it is not without its drawbacks. The size of the flakes produced is small, no more than a few μm , with most of the single layer flakes being smaller than this. A typical flake is shown in figure 2.3(d). There is no way of isolating only single-layer dispersions, few-layer flakes will always be present and will outnumber the single-layer flakes.

For electron microscopy the solvent needs to be removed from the flakes before imaging. The use of low boiling point solvents such as isopropanol (IPA) make low temperature (80 °C) baking sufficient to clean the flakes. Without a baking step a

carbon contamination layer will build up on the flakes during imaging. The presence of contamination is also important for device applications. Contamination has been found to chemically dope graphene[36].

Table 2.1 gives an overview of the advantages and disadvantages of the various graphene preparation techniques outlined in this section.

Graphene preparation technique	Advantages	Disadvantages
Mechanical exfoliation[1]	Best quality	Time consuming
Epitaxial growth on SiC[37]	High quality	High temperature process, difficult to control domain size and thickness
CVD[38]	High quality, large single layer growth	High temperature process, contamination during transfer
Liquid phase exfoliation[27]	Cost effective, scalable	Small flake size, typically few layers, solvent removal

TABLE 2.1: Table of the advantages and disadvantages of the most common graphene production techniques.

2.3 Properties of Graphene

Graphene exhibits many fascinating properties due to its 2D structure. The σ bonds which covalently connect neighbouring carbon atoms in graphene are stronger than those found in diamond[39]. In 2008 Lee *et al.*[40] determined graphene to be the strongest material ever tested. For their measurement they used the tip of an atomic force microscope to indent graphene suspended over a hole in an SiO₂ substrate. They also found that graphene is highly flexible. Graphene's thermal conductivity was investigated in 2008 by Ghosh *et al.*[41].

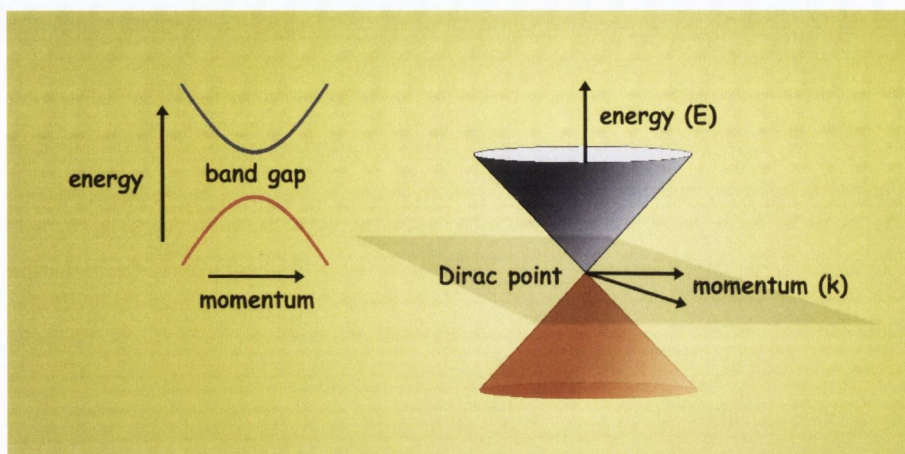


FIGURE 2.4: The dispersion relation of an insulator or semiconductor is shown on the left. The conical dispersion of graphene near the Dirac point is shown on the right.[44]

They used a non-contact optical technique and found it to be the highest recorded yet at nearly $5,000 \text{ W m}^{-1}\text{K}^{-1}$, over an order of magnitude greater than that of bulk silver ($\sim 410 \text{ W m}^{-1}\text{K}^{-1}$) or copper ($\sim 390 \text{ W m}^{-1}\text{K}^{-1}$), the most common thermal conductors.

Graphene also exhibits remarkable electrical properties due to the π -orbital perpendicular to the plane of the σ bonded hexagonal lattice. As these π -orbital electrons interact with the periodic potential of the hexagonal lattice, graphene's novel energy spectrum is formed[42]. The conical shape of the energy spectrum where the valence and conduction bands touch gives graphene a linear energy spectrum, as shown in figure 2.4. The motion of charge carriers in graphene near the Fermi energy is well described by the massless Dirac equation. It is due to this unusual linear energy spectrum that graphene exhibits interesting two-dimensional electronic properties such as Klein tunnelling, the half-integer quantum Hall effect and other quantum electrodynamic phenomena which can be studied using a desktop experiment[43].

Graphene has been found to have carrier concentrations of up to 10^{13} cm^{-2} with mobilities exceeding $10,000 \text{ cm}^2\text{V}^{-1}\text{s}^{-1}$ [1] on a substrate. An atomically smooth substrate can be used to enhance the carrier mobility of graphene by reducing

substrate induced scattering. Mayorov *et al.*[45] used atomically smooth boron nitride layers to encapsulate a layer of graphene. They measured a mobility of $> 100,000 \text{ cm}^2\text{V}^{-1}\text{s}^{-1}$. Bolotin *et al.*[46] went on to demonstrate an increased mobility of $200,000 \text{ cm}^2\text{V}^{-1}\text{s}^{-1}$ by suspending a graphene flake between electrical contacts, thus eliminating substrate induced scattering. This value is the same as the maximum theoretical value predicted by Morozov *et al.*[47]

2.4 Applications of Graphene

The combination of graphene's mechanical strength, thermal dissipation potential and outstanding electrical properties mean it is ideally suited for applications in a range of next generation devices. Graphene can be used in epoxy nanocomposites to produce stronger and stiffer materials than other nanocomposites[48]. Graphene can be used to replace the expensive indium tin oxide (ITO) anode currently used in organic Light Emitting Diodes (LED). This could lead to cost-effective flexible displays[49]. Graphene is very efficient at absorbing light, it could therefore be used to make efficient light sensors and solar cells[50].

Many other applications such as hydrogen storage[51], single molecule detection[52] and supercapacitors[53] all show a lot of promise and are currently being optimised. Graphene has been used to demonstrate a 300 GHz Field-Effect Transistor (FET)[54], and is theoretically capable of producing devices with frequencies up to tens of THz[55].

While graphene has highly mobile charge carriers, resulting in high switching speeds, it is a zero gap semiconductor. Semiconductor logic devices require a band gap in order to achieve an off state. Due to the touching of the valence and conduction bands, and the resulting lack of an electronic band gap, a graphene device would have a poor on/off ratio. Typical on/off ratios for graphene devices are less than 10. The International Technology Roadmap for Semiconductors (ITRS)[10]

states that the on/off ratio for a silicon transistor successor should be in the range of 1×10^4 to 1×10^7 .

For practical adoption of such devices a band gap would need to be engineered. This highlights the necessity for modification of graphene's properties.

2.5 Modification of Graphene

The broad range of applications to which graphene could be applied is clear. However, a precise and reliable method for tailoring the properties of graphene is required before many envisioned applications can be realised practically.

One property which must be tailored is graphene's band gap. An electronic band gap is required for switching operations. Graphene also requires a tunable carrier concentration, as well as control of the type of charge carriers. Current generation silicon technology uses ion implantation to modify these properties but new techniques need to be developed for 2D materials. A further level of control which must be achieved is that of the lateral dimensions of graphene. Nanoscale fabrication of structures such as nanopores and nanoribbons opens up a large range of graphene applications.

Many methods of modifying graphene have been attempted with varying degrees of success to date. Controlled defect introduction in graphene can be used to alter its electronic structure[56] as well as its mechanical[57], thermal[58], optical[59] and magnetic properties[60]. Graphene NanoRibbons (GNR) are desirable for electronic[61, 62] as well as potential spintronic[63] applications, while graphene nanopores have potential as DNA sequencers[5], gas separation membranes[64] and in hydrogen storage[65].

2.5.1 Tuning the Transport Properties

In order to tune the transport properties of graphene many techniques have been employed. Graphene has been found to have a tunable band gap by varying the electric field applied to a bilayer sample[66]. Bilayer graphene however, does not possess the same unique properties as monolayer graphene. This is because monolayer graphene has a linear dispersion, whereas bi-layer graphene has a more common parabolic dispersion.

Leenaerts *et al.*[67] found from a first principles study that molecules adsorbed on graphene, such as NO₂ and NH₃, resulted in *p*-type and *n*-type doping respectively. Control of graphene doping, i.e. *n*-type or *p*-type, can also be achieved by engineering its contacting substrate, for example, tetrafluoro-tetracyanoquinodimethane (F4-TCNQ) for *p*-type[68] and SiO₂ for *n*-type[69].

The introduction of defects into the structure of graphene has been found to provide a means to engineer its conductivity[56]. It was found that there was metallic behaviour within the region of a vacancy defect, allowing enhancement of the conductivity by an order of magnitude. Defects in acid-treated graphene have also been found to affect its electronic structure by bond cleavage[70]. This process involves breaking the C-C bonds by electrophilic attack and damages the structure of graphene. In each of these modification techniques electronic scattering was introduced into the graphene and the charge carrier mobility was subsequently reduced. A trade-off between conductivity enhancement and carrier mobility reduction could be observed.

Energetic beams of charged particles have also been used to modify the structure and properties of the surface of materials. The effect of low energy electron beam irradiation on graphene was investigated by Teweldebrhan and Balandin[71]. They used a Scanning Electron Microscope (SEM) to expose a graphene sample to electrons and measured the resulting effect with Raman spectroscopy. They found

that even relatively low energy irradiation of graphene (<20 keV) caused a significant shift in the material's optical response. This was attributed to bond breaking and sample heating which, over a period of several hours, resulted in disordering and partial amorphization of the graphene lattice. These findings indicate that such a beam can be used to introduce defects and affect a change in graphene's properties. However, the precise mechanism of this modification is the subject of debate[72, 73] as other factors, such as the build up of contamination, could have a significant effect on this time scale of several hours.

2.5.2 Tailoring the Geometry

Geometry engineering at the nanoscale can be used to produce unique structures and can provide a precise method to tune a material's properties[74]. Several etching techniques have been used to pattern the geometry of graphene. Oxidative etching of graphene was achieved by Liu *et al.*[75]; they heated the SiO₂ substrate to 600 °C and exposed the sample to an oxygen rich environment. Etch pits were observed to form due to the etching process as shown in figure 2.5(a). While this method can be used to produce a modified graphene surface it suffers from the limitation of requiring the sample to be in contact with a substrate. The substrate must be thermally conductive to allow the heat to be supplied to the sample. It is also not selective in the area that is etched; the whole sample is subjected to the process.

More precision can be added to this technique by defining the starting points for the oxidation to occur. Nemes-Incze *et al.*[76] used an Atomic Force Microscope (AFM) to create an array of holes in graphene supported on an SiO₂ substrate. They then used an oxygen-nitrogen atmosphere and a temperature of 500 °C to etch these holes into large etch pits. After an annealing step in argon at 700 °C hexagonal etch pits with crystallographically orientated edges, as shown in figure 2.5(b), were produced. This process involves multiple high temperature steps

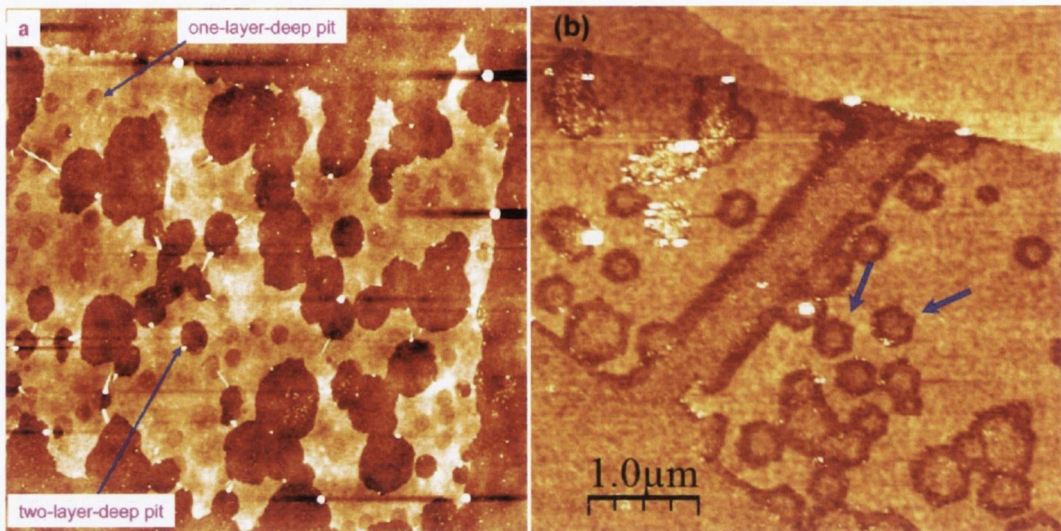


FIGURE 2.5: (a) Thermally assisted oxidative etching of graphene[75]. (b) Etch pits in graphene, after annealing crystallographically orientated edges were produced[76].

which are expensive and time consuming and ultimately not practical in device production.

Graphene can also be patterned by a focused probe of high energy electrons. The electrons must transfer sufficient energy to the atom to overcome the displacement energy¹ of the carbon atoms in the graphene lattice[77]. This value has been found, both theoretically and experimentally, to be ~ 20 eV[78]. The carbon atom can then be removed by the physical sputtering, or knock-on, process. The minimum electron beam energy required to do this is ~ 86 keV[79]. By this process nanopores as seen in figure 2.6(a) can be fabricated[5], these pores can be made as small as 3 nm in diameter[80]. The pore size can be further controlled by subsequent irradiation and heating as seen figure 2.6(b)[81].

The Transmission Electron Microscope (TEM) pore fabrication process was observed to produce structural deformation around the edge of the hole. This effect can be seen in figures 2.6(a) and (b). The TEM is not a practical approach for

¹The displacement energy, T_D , is the minimum kinetic energy that an atom requires to be permanently removed from its lattice position.

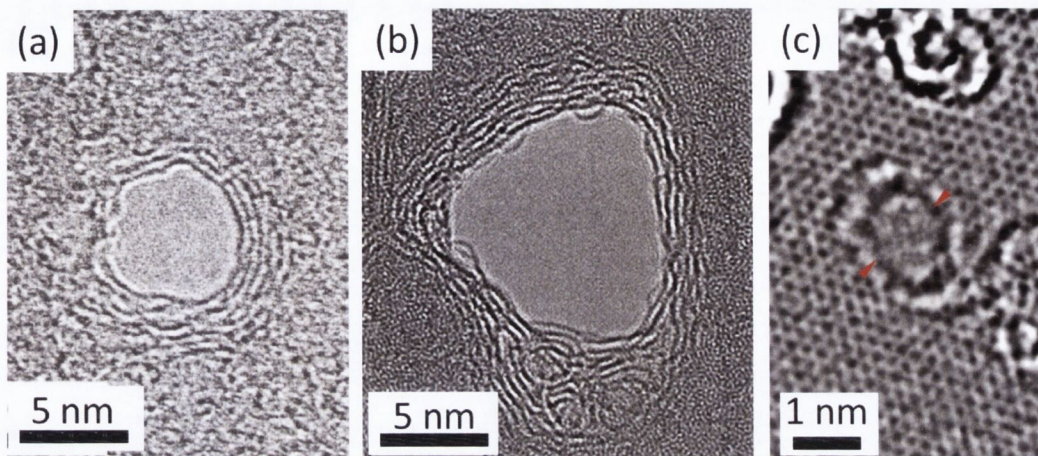


FIGURE 2.6: (a) A TEM fabricated graphene nanopore[5]. (b) A TEM fabricated nanopore after *in situ* annealing for 6 min at 400°C[81]. (c) A nanopore which was grown by TEM irradiation of a helium ion induced defect[82].

fabrication due to the expense of the tool and the rate of the sample patterning, each pore requires a patterning time of a few seconds.

The pore fabrication process can be initiated by the introduction of defects into the material. Russo and Golovchenko[82] used helium ion irradiation to create defect sites in graphene. They then used subsequent TEM irradiation to grow the defects into pores. This approach highlights the requirement for more efficient modification beyond that achievable by TEM.

2.5.3 Graphene Nanoribbons

Graphene NanoRibbons (GNRs) provide a means to open an electronic bandgap[62]. GNRs can be produced with two different edge orientations, shown in figure 2.7. In figure 2.7(a) the armchair edge orientation of the nanoribbon is highlighted in red. In figure 2.7(b) the zigzag edge orientation of the ribbon is highlighted. Zigzag edges are the more stable edge configuration as determined both theoretically and experimentally[83, 84].

GNRs with the zigzag edge orientation present spin polarised edges. However it is GNRs with the armchair edge orientation which have a tunable band gap. This

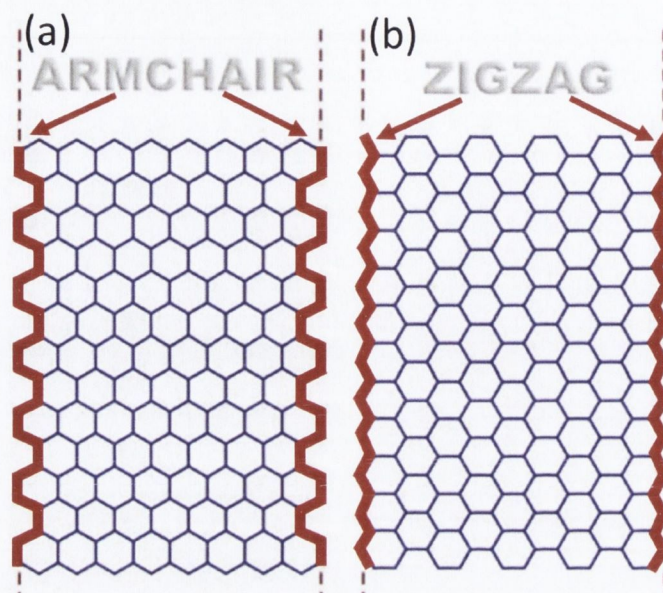


FIGURE 2.7: An illustration of graphene nanoribbons with armchair (a) and zigzag (b) edge orientations[85].

band gap scales inversely with the GNR width[86]. Armchair edge GNRs less than 20 nm wide can be used for room-temperature FET operation[87], however the band gap is very small at only 30 meV and so the on/off ratio would be very low.

In order to produce a band gap greater than 0.3 eV a ribbon width of less than 8 nm is required[88]. If larger band gaps which are comparable with those of Si, InP or GaAs are required the ribbon width must be 1-2 nm. The edge orientation must also be carefully controlled with a pure armchair edge providing the largest band gap. The challenge is to find a technique which can reliably and rapidly produce 1-2 nm wide GNRs with a preselected edge orientation and minimal edge damage.

2.5.3.1 Chemical Production of GNRs

GNRs have been produced by many different techniques to date. A combination of heating graphite in a forming gas and dispersing the resulting material in solvent

have been used to produce solutions of GNRs[61, 89]. These chemically derived nanoribbons have been produced with widths as narrow as 2 nm. These ribbons have been shown to have on/off ratios of $\sim 10^7$ at room temperature. This would be a suitable value for next generation devices. However, the production process yields a range of ribbon widths as well as multilayer ribbons.

Thermally activated nickel nanoparticles have been shown to etch graphene along high symmetry directions in the crystal, i.e. producing zigzag or armchair edges. This method can produce <10 nm wide ribbons[90, 91]. There is a limited amount of control using this technique. The etching occurs along preferred directions and, as such, arbitrary geometries cannot be patterned.

The production of graphene nanoribbons from carbon nanotubes has also been achieved. Interestingly it was almost a decade before the isolation of graphene that structures similar to graphene nanoribbons were first investigated. Nasreen *et al.*[92] reported their work on ‘flattened’ carbon nanotubes, discussing the potential effect of this structure on the material’s properties. It has only been over the past couple of years that the process of fabricating nanoribbons of graphene from carbon nanotubes has received significant attention.

One approach to creating nanoribbons from nanotubes was developed by Jiao *et al.*[93] They produced ribbons with smooth edges and widths between ten and twenty nanometres. A polymer layer was spin-coated onto a substrate which had been deposited with carbon nanotubes. They found that when the polymer layer was removed from the substrate the nanotubes were partially exposed on the underneath of the film. An argon plasma was used to etch the exposed region. When removed from the polymer film the nanotubes were found to have been converted to ribbons of graphene. While this process can produce good quality GNRs which remain structurally intact, it can also cause breaking of the nanoribbons. It is a multistep process with contaminating polymers and solvents necessarily coming into contact with the graphene.

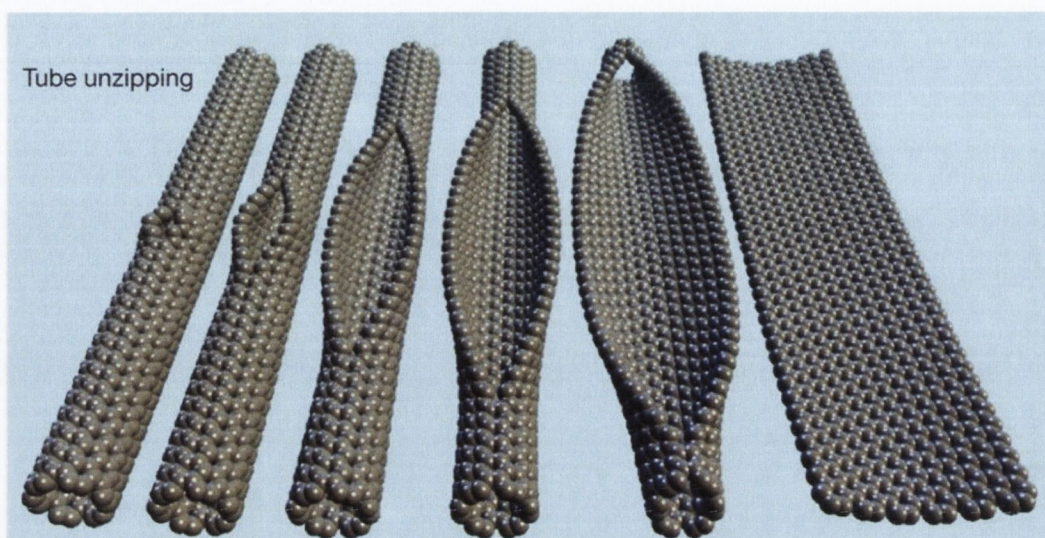


FIGURE 2.8: An illustration of the process of oxidatively ‘unzipping’ a carbon nanotube to produce a narrow graphene nanoribbon[94].

Another technique developed by Kosynkin *et al.*[94] uses a solution-based oxidative etching process to ‘unzip’ nanotubes. An illustration is shown in figure 2.8. While this process results in high yields of nanoribbons it introduces significant chemical modifications to the graphene. The graphene must be chemically reduced to restore some electrical conductivity; however even after this step the graphene contains oxygen functionalities on its surface and edges.

Electron Beam Lithography (EBL) is a common technique for patterning features with dimensions down to ~ 20 nm. EBL can be used to pattern graphene into nanoribbons. In EBL a resist is spin coated onto the substrate. A pattern is exposed within the resist by the focused electron beam of an SEM. In the case of a negative resist such as Hydrogen SilsesQuioxane (HSQ) the exposed area remains unaffected by a solvent bath while the unexposed resist is removed leaving the underlying graphene exposed. The exposed graphene is then removed by a reactive ion plasma. The limitations of this technique occur due to the sample contamination introduced by the use of chemicals in this resist-based process, HSQ is not easily removed.

In 2007 Chen *et al.*[87] demonstrated the production of GNRs by EBL. The limitations of the process resulted in the narrowest ribbons being no less than 20nm wide. They also found that the ribbons had rough edges which introduced scattering and increased the device's resistivity. The width of the ribbon meant that no appreciable band gap was opened and it was therefore not suitable for room-temperature transistor operation. More recently EBL GNRs down to 12 nm wide have been produced with bandgaps of up 0.1 eV[95].

EBL has the advantage of being a fast and scalable approach, however, a sufficient bandgap to make EBL a viable route for production of GNRs with high on/off ratios at room temperature has not been achieved. This is due to the fundamental limitations of this technique imposed by the proximity effect which limits the minimum size of features that can be produced by EBL. The proximity effect is caused by the interaction of the beam with the resist and the substrate. Unexposed areas of the resist receive a non-zero dose if they are in close enough proximity to an exposed area. The final features are therefore larger than the defined pattern. The resolution of the technique is typically limited to around 20 nm feature sizes[96].

The proximity effect which limits the feature sizes produced by EBL is significantly less of an issue in helium ion beam lithography (HIL)[97–100]. A focused beam of helium ions can also be used to expose a resist as it is the secondary electrons produced by the beam, and not the primary beam itself, which expose the resist. The other steps in the process are the same as those used in EBL. The helium ions used in HIL have the same energy as the electrons typically used in EBL. HIL is superior to EBL for several reasons.

- Helium ions remain more spatially confined within the resist than electrons.
- The yield of secondary electrons is higher for a helium ion resulting in more efficient resist exposure.
- The secondary electrons produced by the helium ion beam have a lower energy, these lower energy electrons are more efficient at exposing the resist.

- The yield of backscattered ions is much lower than the yield of backscattered electrons in an SEM. Backscattered particles return to the surface and expose the resist in a different area to where it entered the resist, this reduces the resolution of the exposure.

However, HIL is still in its infancy and it remains to be seen what the potential, as well as the practical limitations, of this technique may be.

2.5.3.2 Physical Production of GNRs

Scanning Tunnelling Microscopy (STM) has been used to produce GNRs with a width of 2.5 nm and a band gap of 0.5 eV[101, 102] which will provide a high on/off ratio. This value is comparable with the bandgap of germanium, 0.67 eV. This technique provided interesting insight into GNRs for fundamental investigations but does not offer a practical means of GNR production on a larger scale.

Focused beams of charged particles can be used to pattern materials. The dose required to mill is orders of magnitude greater than that required to image. Inspection is therefore possible on the same tool *in situ* without causing significant damage[103]. The sub-nanometre probe size which can be achieved with electron and He⁺ beams allows patterns with feature sizes an order of magnitude smaller than EBL or Focused Ion Beam (FIB) machining to be achieved. Patterning with these beams can be done directly without using resist-based techniques and without implanting metallic contaminants which cannot be avoided in other focused particle beam tools such as the gallium FIB.

Nanoribbons can be sculpted by a focused probe of high energy ($> \sim 86$ keV) electrons. A TEM with a 200 keV beam energy was used to produce the GNR shown in figure 2.9(a)[104]. GNR patterning with a TEM was also demonstrated by Robertson *et al.*[105]. They fabricated the GNR shown in figure 2.9(b) using an 80 keV beam energy. This energy is technically under the minimum e-beam

energy required to transfer sufficient energy to overcome the displacement energy threshold of carbon atoms in graphene. However, at a sufficient beam dose defects will be produced in the graphene which lower the carbon displacement energy. The TEM provides *in situ* characterisation of the ribbons fabricated. However, as mentioned in section 2.5.2 the TEM is not a practical tool for fabrication as it has very limited throughput.

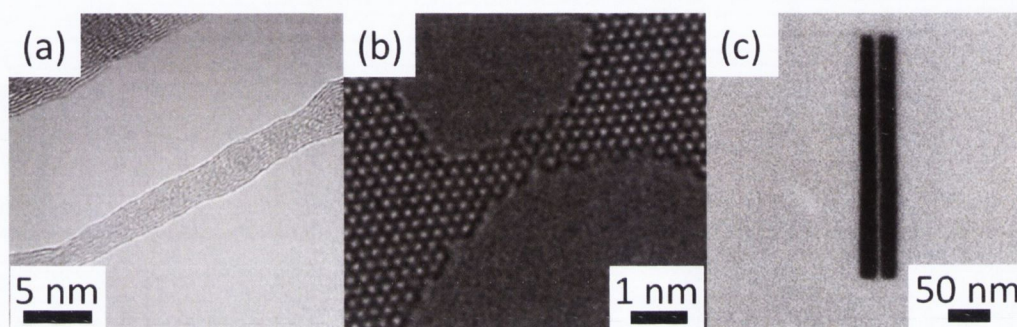


FIGURE 2.9: (a) A GNR produced in suspended graphene by a 200 keV focused electron beam[104]. (b) A GNR produced in suspended graphene by an 80 keV focused electron beam[105]. (c) A 5 nm wide graphene nanoribbon fabricated in suspended graphene by a focused helium ion beam[106].

A focused helium ion beam has also been used to pattern graphene into ribbons. Early work on the patterning of graphene with a focused helium ion beam in 2009 produced minimum feature sizes of ~ 10 nm[106–108]. The team further improved on this result in 2010 by fabricating GNRs with line widths as narrow as 3 nm[109]. A high aspect ratio ribbon which is just 5 nm wide is shown in figure 2.9(c). The lattice damage due to the milling was found to recover at a distance of about 1 nm from the patterned edge.

This direct patterning is not possible with low energy (typically up to 30 keV) electron beam irradiation in the SEM as no sputtering of material occurs[110] below ~ 86 keV. Helium ion beam milling is also more efficient than high energy e-beam milling employed in the TEM[111] due to the higher rate of energy transfer from the He^+ to the sample. Zhou *et al.*[112] concluded in their review of graphene

patterning techniques that the “Nanostructuring of graphene is most convincingly demonstrated by helium ion microscopy”.

In order for HIM to be realised as a viable technique for GNR fabrication some issues will need to be overcome. An understanding of the beam-sample interactions occurring will be required. As the edge structure is key in determining the properties of the GNR the extent of the edge damage introduced by the HIM patterning process needs to be further investigated. The patterning parameters must also be optimised in order to attain the best modification results achievable.

Graphene has been shown to have unique properties which are of great interest for many applications. Other layered materials, such as MoS₂, are now being extensively researched as they too can display unique properties when isolated as single layers. A greater range of uses for these materials can be enabled by control of the structure and geometry of the material.

A modification technique which has nanoscale spatial resolution is required. The technique must provide sufficient control to tune the properties or the geometry of a 2D sample. The properties must be tuned to control the electronic response of the material so that it can be used for device applications. Geometrical tailoring is another route to altering the electronic band structure of the material. A well defined edge structure with minimal damage extension is required for best results. Tailoring the structure can not only modify the electronic properties but can also produce nanopores which are required for a range of applications as discussed in section 2.5.

Chemical etching and physical sputtering are among the modification techniques most widely used. Chemical processing generally introduces contaminants and defects, whereas physical modification is a more direct and controllable approach. Focused beams of charged particles provide the highest resolution direct modification of layered materials.

The question of the ability of a <30 keV beam of electrons to modify graphene, and to what extent this can be exploited, remains to be fully answered. The direct structural modification and material removal by a highly focused beam of helium ions is also a technique which has yet to be explored and optimised. The mechanisms by which this can be achieved will be discussed in the next chapter.

Chapter 3

Modification Methodologies

In the previous chapter a review of 2D materials was presented. The modification requirements for these materials are now understood. The main requirements are the introduction of a well-defined amount of damage and nanoscale lateral control. The most promising techniques which can be used to modify these materials were also discussed. EBL, chemical etching and plasma etching showed potential but it was the charged particle beams which were deemed most suitable. The challenges and limitations of these techniques were clarified.

In this chapter we will describe in detail the methodologies which we have adopted in this work. We have developed new techniques based on our understanding of the limitations which exist with current technologies. These techniques employ the use of charged-particle beams. Finally, characterisation techniques such as charged-beam microscopy, as well as optical and spectroscopic techniques, will be described.

3.1 Focused Electron Beam

The capability of a beam of electrons to modify a material was first assessed. The energy coupling between the beam and the sample must be investigated to determine if this method is feasible.

3.1.1 Beam-Sample Interaction

When a beam of electrons enters a sample it will begin to transfer energy to the sample through various collisions. The maximum energy transferred through elastic scattering¹ depends on the beam energy and the mass ratio of the two particles. The maximum transferable energy, T_m , from a projectile (beam particle) of energy E to an atom is given by[113]:

$$T_m = \frac{4M_1M_2}{(M_1 + M_2)^2} E \quad (3.1)$$

where M_1 and M_2 are the mass of the projectile and target atom respectively. In the case of two particles with identical masses an efficient energy transfer occurs. As the masses diverge the energy transfer becomes inefficient and a higher beam energy is required to transfer significant kinetic energy.

An electron and a carbon atom have significantly different masses (1:21,800), however, a sufficiently high energy electron beam can transfer enough energy to overcome the carbon displacement energy. Displacement energies for most materials are typically a few eV. In the case of sp² bonded carbon in graphene the electron beam energy must be $> \sim 86$ keV for knock-on damage to occur.

Elastic scattering can also cause the beam electron to deviate from its original trajectory in the sample. The exact scattering events which a particular particle will undergo after entering a sample cannot be precisely predicted as this is a

¹Elastic scattering refers to the interaction between the beam and a sample nucleus.

stochastic process. Instead we must describe the probability, $P(E)$, of an event occurring. The probability, or cross section (σ_e), for elastic scattering above a minimum angle ϕ_0 is described by the equation[114]:

$$\sigma_e = 1.62 \times 10^{-20} \left(\frac{Z^2}{E^2} \right) \cot^2 \left(\frac{\phi_0}{2} \right) \quad (3.2)$$

where Z is the atomic number of the sample and E is the energy of the projectile. From this equation we can see that σ_e is approximately $\propto 1/E^2$. The scattering angle is also strongly forward scattering.

The trajectories of 200 electrons in a bulk carbon target were simulated using the ‘monte CARlo SIMulation of electroN trajectory in sOlids’ (CASINO) software package[115]. The result is shown in figure 3.1. Multiple beam energies were used. The 5 keV beam on the left experiences strong deflection and deposits its energy in the sample within a short distance. The 20 keV beam on the right remains fairly well collimated within the sample for the first few hundred nanometres. It then begins to lose energy and become more severely deflected, eventually coming to rest. In these simulations the electron path is no longer plotted when its energy becomes less than 50 eV. The red paths are created by electrons which have backscattered within the sample and are moving towards the surface.

The simulation can be used to find the average size of the area on the surface through which backscattered electrons (BE) escape from. This value is related to the interaction volume of the beam in the sample. It gives an idea of the effect of beam energy on modification resolution. For a 5 keV beam energy the surface radius of BE was 25 nm. This value increased to 66 nm for a 10 keV beam energy. For 15 keV it was 195 nm, and finally for 20 keV the surface radius of BE was 454 nm. This trend approximately follows the same relationship as the penetration depth vs. beam energy, i.e. the surface radius of BE is approximately $\propto E^2$.

The cross section for elastic scattering is also approximately $\propto Z^2$, where Z is the atomic number of the atoms from which the sample is composed. This relationship

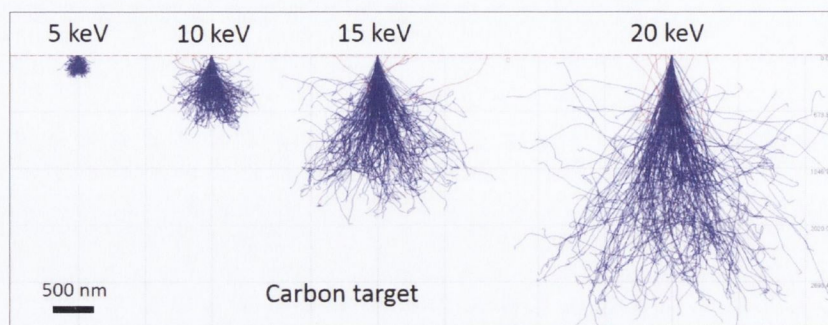


FIGURE 3.1: Simulated trajectories of 200 electrons in a carbon target. The interaction volumes of four beams with different energies are shown.

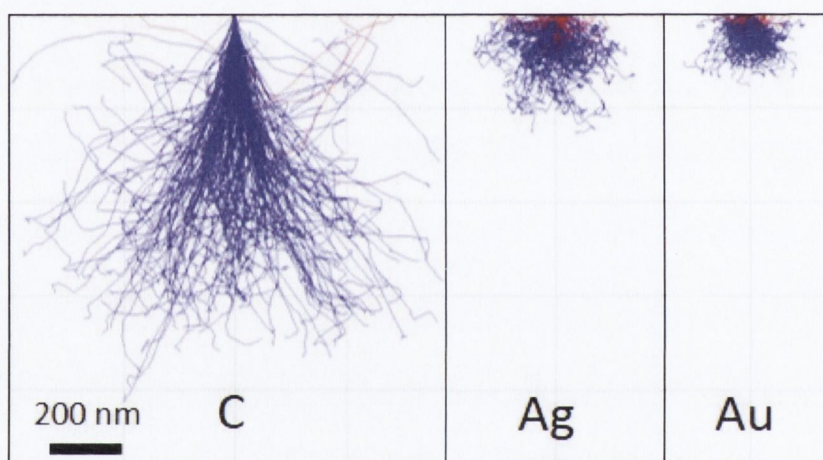


FIGURE 3.2: Simulated trajectories of 200 electrons in carbon, silver and gold targets.

was modelled in the simulation in figure 3.2. The simulation uses an electron beam energy of 10 keV and samples of carbon, silver and gold with atomic numbers of 6, 47 and 79 respectively. The stronger interaction in the gold causes the beam to deposit its energy near the surface of the sample and not penetrate as deep as in the carbon sample on the left.

A summary of the main points of the elastic scattering process is given below:

- For knock-on damage to occur the displacement energy of an atom in the sample must be overcome. A beam with sufficient energy can remove sample material by this mechanism.

- The most probable elastic collision will result in a minor deviation of a beam electron from its path. Scattering to higher angles is less common.
- Lower energy beams undergo many collisions within a short distance in the sample. They do not penetrate as deep and they produce secondary signals from a more localised region of the sample.
- Samples with higher mass elements cause a beam to scatter more strongly. The beam penetration is shallow.

The beam electrons can also scatter inelastically whereby energy is transferred to the sample electrons. Inelastic scattering can break the chemical bonds in a sample by a process known as radiolysis. This bond breaking can alter the structure and properties of materials. If sufficient radiolysis occurs a crystal structure can be degraded to a more amorphous form.

Another significant process which occurs during the irradiation of a sample with an electron beam is contamination. Hydrocarbon molecules are present on the sample surface and in the imperfect vacuum ($100 \mu\text{Pa}$) of the chamber. Hydrocarbons are highly mobile on most surfaces. Inelastic scattering produces secondary electrons which dissociate the hydrocarbons resulting in the deposition of a polymerised carbon layer on the surface of the sample. An example of carbon contamination spots deposited by a focused electron beam can be seen in figure 5.1(b).

3.1.2 Low Energy E-beam Activated Gas Etching

It was shown in section 2.5 that nanopores can be created in graphene by heating it in a gaseous environment. By this process a reaction between the oxygen gas and the carbon atoms was activated and pores were created in the graphene. However this process is not localised. On the other hand, modification of graphene's geometry cannot be achieved by an electron beam with an energy $< \sim 86 \text{ keV}$.

What we wish to consider is the possibility of etching graphene by supplying energy to the system with a low-energy (<30 keV) focused electron beam. The electron beam can provide the energy required to overcome the activation energy to facilitate a reaction between carbon and a gas, in this case nitrogen. The energy from the electron beam is coupled to the system both by ionisation of nitrogen gas and by heating of the graphene sample. This approach can provide nanoscale graphene modification which is localised to a confined region of the sample.

In order to understand the etching process the probability of the nitrogen ionisation by the electron beam will first be calculated. This process is dependent on the energy of the electron beam. A lower energy electron beam (down to 100 eV) will couple energy more efficiently to the nitrogen molecule and result in an increased ionisation cross section.

The lower energy electron beam also couples energy more efficiently to the graphene sample. The transfer of energy to the graphene leads to a reduction of the activation energy, the energy required for the nitrogen and carbon atoms to react. After the reaction a gaseous species is created and diffuses from the region of the sample surface. The activation energy for the reaction is also reduced at defective sites, such as flake edges or vacancies. At these locations the reaction rate is higher and more etching will occur.

The ionisation cross section, $\sigma_i(E)$, was calculated by using the Binary-Encounter-Bethe (BEB) equation[116].

$$\sigma_i(E) = \frac{S}{t + (u + 1)/n} \left[\frac{Q \ln t}{2} \left(1 - \frac{1}{t^2} \right) + (2 - Q) \left(1 - \frac{1}{t} - \frac{\ln t}{t + 1} \right) \right] \quad (3.3)$$

where $t = E/B$, $u = U/B$, $S = 4\pi a_0^2 N (R_H/B)^2$, $a_0 = 0.52918 \text{ \AA}$, $R_H = 13.6057 \text{ eV}$ and Q is approximated to 1. E is the energy of the electron beam. The binding energy B , the orbital kinetic energy U , the electron occupation number N , and a dipole constant Q are constants for each orbital within a given atom or molecule. The total ionisation cross section for a given atom or molecule is found

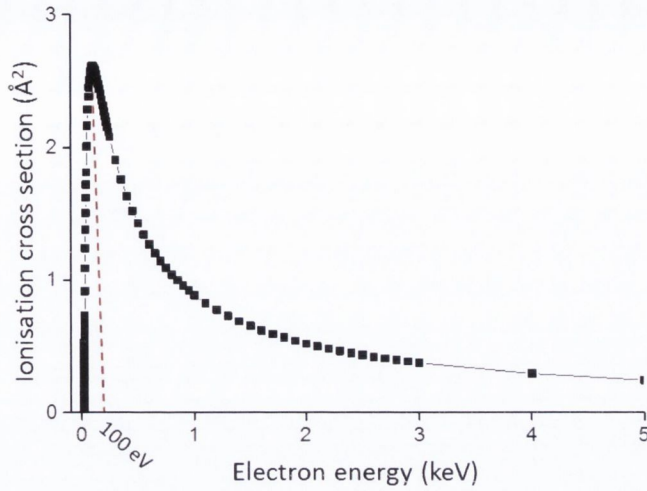


FIGURE 3.3: Ionisation cross section of the nitrogen molecule as a function of the energy of an incident electron.

by summing the contributions from each orbital. The calculation must then be repeated if the ionisation cross sections for multiple electron beam energies are required.

From figure 3.3 we can see that the ionisation cross section increases as the electron energy decreases until a maximum is reached at approximately 100 eV, at which point the cross section decays again. This was plotted using equation 3.3 with electron energies from 15 eV to 5 keV and the values for the nitrogen molecule[117].

We then consider the energy transfer from the electron beam to the graphene sample. The Bethe model[114] can be used to describe the rate of energy loss, dE , with distance travelled in the sample, dS . This equation is given as:

$$\frac{dE}{dS} = 2\pi e^4 N_0 \frac{Z\rho}{AE_i} \ln \left(\frac{1.166E_i}{J} \right) \quad (3.4)$$

where e is the electron charge, N_0 is Avogadro's number, Z is the atomic number, ρ is the density of the sample, A is the atomic mass, E_i is the electron energy at any point in the sample and J is the average energy loss per event. If we consider only the energy loss through phonon excitation then we can estimate the thermal

energy deposited in the sample using equation 3.4. Equation 3.4 states that the energy transferred to the sample increases as the beam energy is decreased.

Interactions with the sample through mechanisms such as plasmon excitations will also couple energy to the graphene and contribute to the heating effect. The overall trend of a stronger coupling of energy from the beam to the sample at lower beam energies is still valid and is estimated using the above simplification. Other factors, such as vacuum and surface contaminants, are likely to contribute to the etching process to some extent. However, these factors will be minimised through sample cleaning and careful sample handling. As a result of theoretical consideration we do not expect them to contribute significantly to the etching process, this will be confirmed experimentally.

The two equations (3.3 and 3.4) can then simply be combined as they represent independent processes. The combination of these two equations, shown in equation 3.5, describes the rate of energy transfer from the beam to the gas etching reaction. The rate of energy transferred to the system is equivalent to the etching rate.

$$R = k2\pi e^4 N_0 \frac{Z\rho}{AE_i} \ln\left(\frac{1.166E_i}{J}\right) \left(\frac{S}{t + (u + 1)/n}\right) \left[\frac{Q \ln t}{2} \left(1 - \frac{1}{t^2}\right) + (2 - Q) \left(1 - \frac{1}{t} - \frac{\ln t}{t + 1}\right)\right] \quad (3.5)$$

where R is the etching rate and k is a scaling parameter with a unit of $\text{nm s}^{-1} \text{keV}^{-1}$. The area of material removed, A , is dependent on the electron energy and is equal to the etching rate, R , multiplied by the etching time,

$$A(E, t) = Rt \quad (3.6)$$

This approach provides a means to remove material from a graphene sample. The etching is spatially controlled by positioning the electron beam on the sample. A

pattern of a required geometry can then be produced by moving the electron beam across the sample surface.

3.1.2.1 Control of the E-beam Modification

There are a range of parameters which may be adjusted to control the modification of two-dimensional materials in the gas assisted e-beam etching process. These parameters include, the probe size, the beam dwell time, the beam current, the beam energy and the gas pressure. Control of these parameters can be achieved in a scanning electron microscope (SEM).

The electron beam must be confined to a small region on the sample surface. This is required to localise the etching process to a well-defined area. The electron beam is focused onto the sample surface as described in section 4.1.

A measurement of the size of the electron probe can be made during experiments. When a high magnification image of a sample with a sufficiently sharp edge is acquired, the intensity profile across that edge is attributed to the size of the imaging probe. A flake of graphene suspended on a holey carbon support film was imaged before our experiments in order to measure the probe size. The intensity profile across the flake edge was plotted using the ImageJ software package[118]. The intensity of the flake was taken as 100% while the surrounding area was 0% intensity. The distance over which the intensity drops from 75% to 25% was taken as the probe size. The electron probe size achieved in an SEM is typically less than 10 nm and is ~ 1 nm in modern instruments.

The position of the electron beam on the sample can be adjusted using electromagnetic scanning coils. The coils are located within the electron column and deflect the beam laterally in a matrix pattern during imaging. They can also be used to drive the beam arbitrarily, although the use of an external scanning control system is often required to achieve complex patterns.

The beam current can be adjusted by changing the strength of the condenser lens. A stronger condenser setting will bring the crossover plane within the column further above the aperture, allowing less current to reach the sample. The current can also be adjusted by changing the size of the beam limiting aperture. Inserting a smaller aperture will reduce the current which reaches the sample. Using these methods the current can be adjusted from 9 pA to 5 nA in the instrument used.

The dwell time, or time to which the sample is exposed to the electron beam, can be controlled by deflecting the beam off the sample by a beam blanker. An electron beam blanker typically allows a minimum exposure time of between 100 ns and 10 μ s. The time of exposure, combined with the beam current, will determine how many electrons are available in the experiment.

Another parameter which must be considered is the energy of the electron beam. A potential difference within the electron column is used to vary this parameter. In an SEM the beam energy is typically controllable within the range of a few hundred eV to 30 keV.

As well as controlling the number of electrons available in the experiment, the number of gas molecules can also be controlled. By adjusting the flux of gas into the SEM chamber we can ensure that the desired number of gas particles contribute to the etching. The pressure range available is from 70–400 mPa.

The process of low energy e-beam etching is more controllable and practical than the other techniques reviewed in the previous chapter. This method is truly confined to the nanoscale, with a fabrication resolution of just tens of nanometres. The resolution is primarily limited by the diffusion of nitrogen ions from the region of the electron probe.

3.2 Focused Gallium Ion Beam

A direct patterning technique can be achieved through the use of a focused beam of gallium ions. Gallium ions directly displace atoms from the sample without the need for an etching gas due to their large momentum.

3.2.1 Beam-Sample Interaction

Gallium ions interact strongly with material. They have a mass of over 127,000 times that of an electron. When supplied with sufficient kinetic energy the ions can cause significant damage and material removal from the surface of a sample. The energy transfer from a gallium ion to a carbon atom is so efficient that a gallium ion with a kinetic energy of only a few tens of eV can displace a carbon atom from a graphene lattice.

Gallium ions are typically accelerated to 30 keV for milling applications. This energy is large enough for a single ion to displace several atoms within a sample. In fact what occurs is that the gallium ion transfers a significant amount of energy to atoms in the sample. These atoms then recoil and travel onwards in the sample causing a cascade of damage. This process was modelled in figure 3.4. In this figure the path of gallium ions was plotted as a black line. The recoiling carbon atoms were plotted with an orange path. Green points show where the recoiling carbon atoms came to rest. The average number of displacements which result, directly or indirectly, from a 30 keV gallium ion incident on the surface of this sample was 333 displacements per ion.

3.2.2 Control of the Gallium Ion Beam Milling

A focused beam of gallium ions is generated within a Focused Ion Beam (FIB) microscope. The components of the FIB column are much the same as those of any

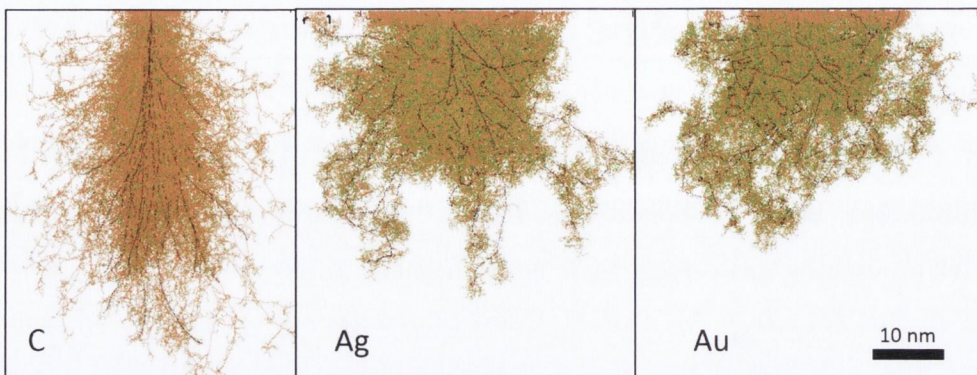


FIGURE 3.4: A simulation of the interaction of 30 keV gallium ions within carbon, silver and gold samples. Most of the damage is caused by recoiling sample atoms (orange) rather than the primary gallium ions (black).

other scanning beam microscope. Lenses are used to focus the beam, an aperture is used to select the beam current and octopoles shape and scan the beam.

Where the FIB differs from other microscopes is its source. The FIB uses a Liquid Metal Ion Source (LMIS) to produce a beam of gallium ions. This source can produce a range of beam currents from 1 pA up to tens of nanoamps while remaining focused. Resolution is traded for a large beam current; the highest resolution is achieved at lower beam currents.

The limitation of this ion source is the energy spread of ~ 5 eV[119]. This energy spread leads to chromatic aberration of the beam within the lenses. Ions with different kinetic energies get focused to different points on the sample.

The FIB is ideally suited to removing micro and even nanoscale regions of material from a sample. However the momentum of the gallium ions, coupled with the limited resolution of the tool (~ 5 nm[120]) make it impossible to fabricate features with dimensions of just a few nanometres. Feature sizes are limited to >10 nm at best[121].

3.3 Focused Helium Ion Beam

Focused helium ion beam milling directly uses the beam-sample interaction to remove material from the sample. No etching gas is required. It can also provide sub-nanometre lateral patterning acuity. Feature sizes an order of magnitude smaller than those created by FIB can be patterned. This approach can therefore provide a greater level of modification control than low energy e-beam etching.

3.3.1 Beam-Sample Interaction

The trajectory of helium ions in a sample depends on the beam energy and the sample composition. The helium ions will penetrate further into the sample as the beam energy is increased. This is shown in the ion simulation in figure 3.5. In this figure the ‘Stopping and Range of Ions in Matter’ (SRIM) software package was used to simulate the trajectories of 200 helium ions in a 3D carbon sample. The effect of the target composition was also simulated in figure 3.6 using carbon, silver and gold targets. The ion beam was observed to scatter more strongly and penetrate less deeply into materials with a higher Z number.

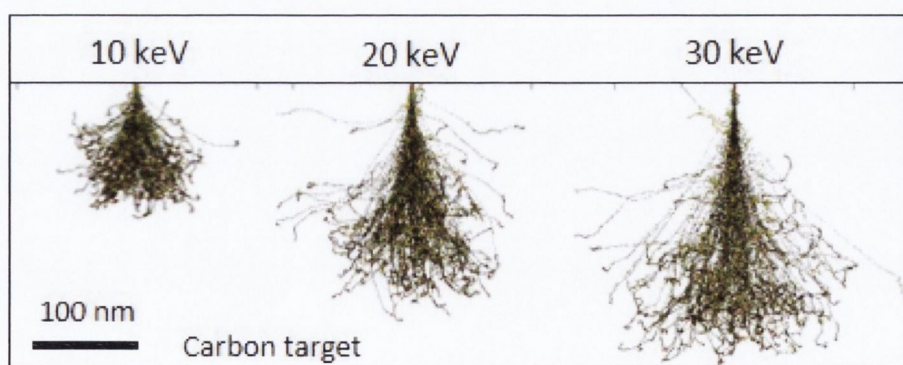


FIGURE 3.5: A simulation of the trajectories of 10, 20 and 30 keV helium ions in a carbon sample.

The trajectory of the helium ions in a sample is different to that of electrons. In figure 3.7(a) we can see the distribution of 30 keV electrons after interaction within

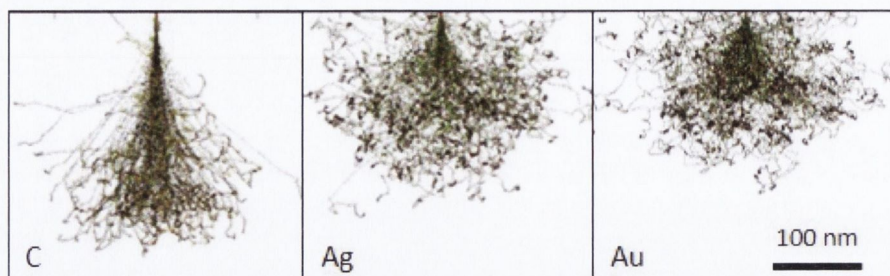


FIGURE 3.6: A simulation of the trajectories of 30 keV helium ions in samples with different atomic numbers. Carbon, silver and gold samples were used.

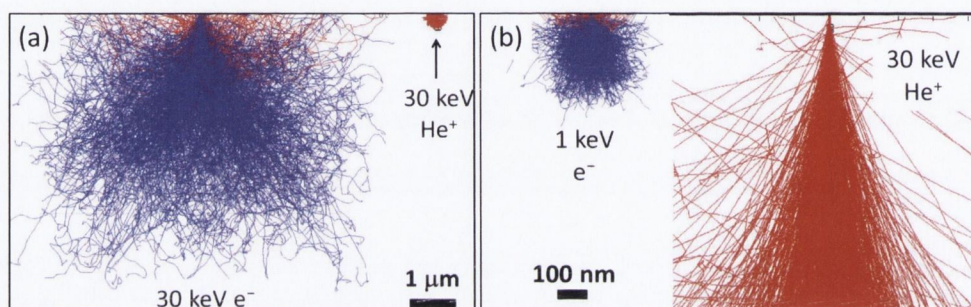


FIGURE 3.7: (a) 30 keV electron beam interaction volume compared with 30 keV helium ion beam interaction volume in silicon. (b) 1 keV electron beam interaction volume compared with part of the 30 keV helium ion beam interaction volume in silicon.

a silicon sample. This was simulated using the CASINO software package[115]. As well as penetrating deep into the sample, the beam electrons experience large angle deflections and backscattering in the sample. In comparison, the interaction of a 30 keV helium ion beam in a silicon sample is shown on the right hand side in figure 3.7(a). The helium ion interaction volume is far more localised within the sample. The ion interactions were modelled using the SRIM software package[122].

The interaction volume in the SEM can be reduced by decreasing the beam energy. In figure 3.7(b) we see the simulated distribution of 1 keV electrons in silicon. The electrons are confined to a much smaller volume at this reduced energy and do not penetrate as deep as the 30 keV helium ion beam. However, the electron beam undergoes large deflections while the helium beam (shown on the left of figure 3.7(b)) remains well collimated in the near surface region (~ 100 nm).

The interaction volume describes the propagation of the ions or electrons within a

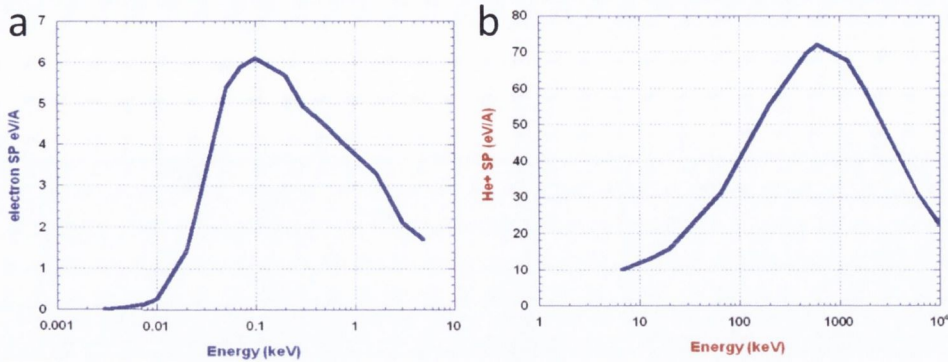


FIGURE 3.8: The stopping power as a function of the beam energy for electrons (a) and helium ions (b) in a chromium sample[123].

sample and the position at which they come to rest. However, along their journey through the sample the beam ions/electrons lose energy and the probability of a collision occurring changes. In figure 3.8 the stopping power as a function of the beam energy is shown. The stopping power simply refers to the rate of transfer of energy from the beam to the sample. In figure 3.8(a) the stopping power for an electron beam in a chromium sample is shown. Within an electron energy range of 10 keV down to 100 eV the stopping power is increasing. The electron beam interacts more and more strongly with the sample as it loses energy. The opposite is true for helium ions within the energy range below 500 keV as seen in figure 3.8(b). Helium ions deposit energy to the sample at the greatest rate when they first enter the sample.[123]

The reason for these opposing trends is the velocity of the particles. Helium ions have a mass of approximately 7,300 times that of an electron. A helium ion with the same kinetic energy as an electron will have a velocity which is 86 times less than that of the electron. When the stopping power graphs are replotted with velocity instead of energy on the x-axis then the curves follow the same trend (see figure 3.9). This indicates that it is the particle velocity which determines the stopping power trend, and not its energy[123].

The stopping power describes the energy transferred from the beam to the sample by both elastic and inelastic interactions. The electronic and nuclear stopping

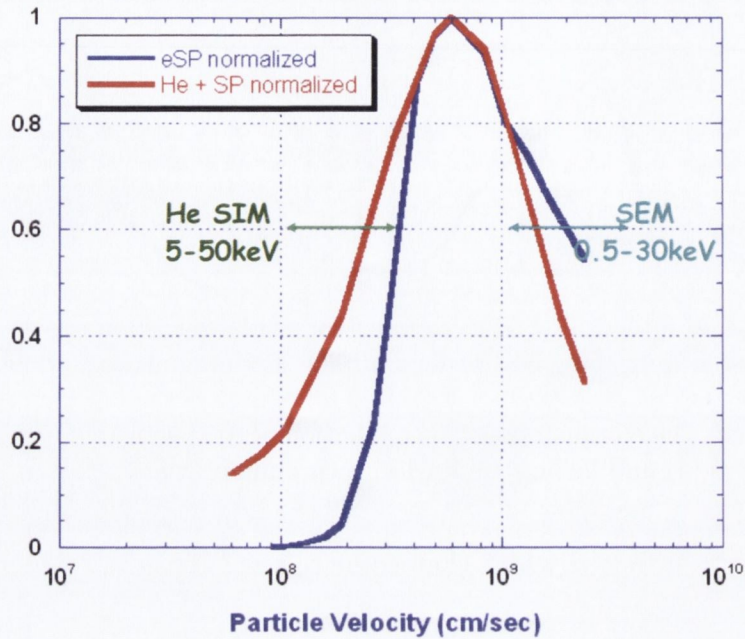


FIGURE 3.9: The stopping power curves of electrons and helium ions as a function of particle velocity[123].

power for helium ions in carbon are plotted separately as a function of helium ion energy in figure 3.10[124]. The electronic stopping power is a result of inelastic collisions whereby the beam transfers energy to the sample electrons. The electronic stopping power is highest as the beam enters the sample. As the beam continues to propagate through the material the electronic stopping power decreases while the nuclear stopping power increases. Eventually, at around 4 keV for aluminium[124], the nuclear stopping power becomes greater than the electronic stopping power. At this point the beam transfers most of its energy to the nuclei in the sample. The damage due to displacement of the atoms in the sample is greatest at this point. While aluminium is not used in this thesis the overall trend is well represented by this data.

Graphs of the ion penetration depth and the depth of damage events produced by a helium ion beam with an initial energy of 30 keV in an aluminium sample are shown in figure 3.11. The damage is observed to occur most prominently near the end of range of the beam path. This is in agreement with the stopping power

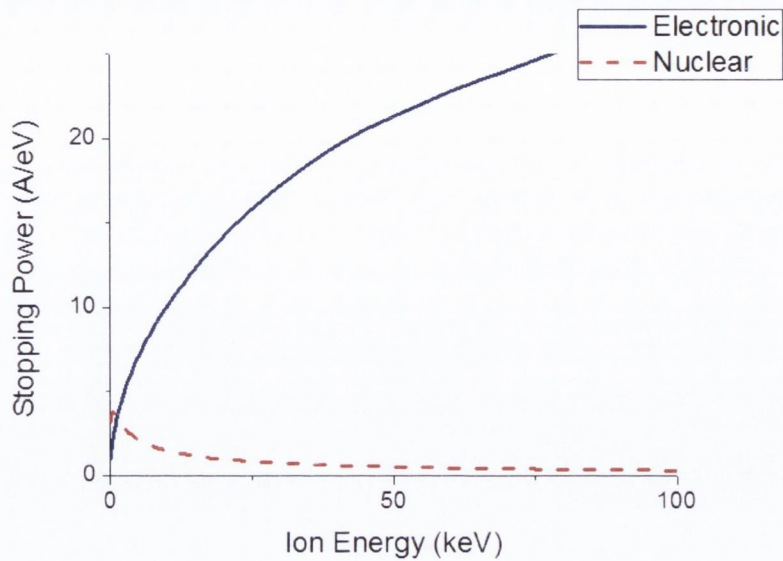


FIGURE 3.10: The electronic and nuclear stopping power for helium ions in carbon are plotted separately as a function of helium ion energy[124].

graph which shows an increase in the elastic collisions near the end of range of the ion trajectory.

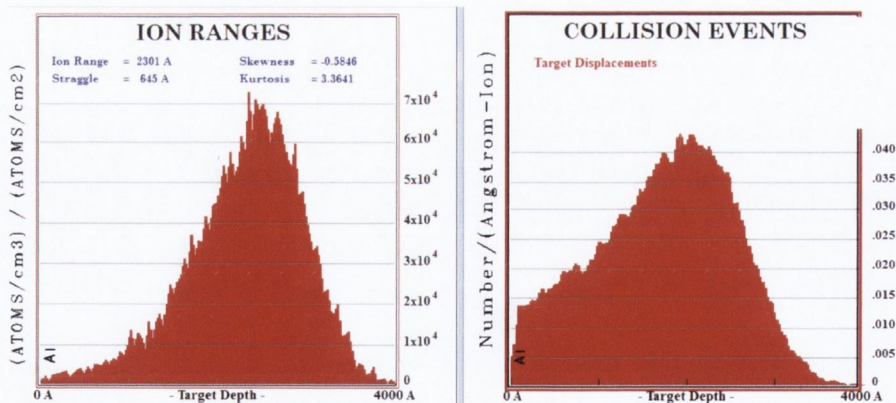


FIGURE 3.11: SRIM graphs of the ion penetration depth (a) and the depth of damage events (b) produced by a 30 keV helium ion beam in aluminium.

3.3.2 Helium Ion Beam Milling

A focused beam of helium ions can cause atomic displacements within a sample. The dose is defined as the number of ions per unit area. At high doses these displacements lead to amorphisation and removal of surface material by sputtering.

The extent of the damage caused by the helium ion beam and to what extent this can be exploited needs to be estimated.

In order to modify and pattern nanomaterials using a focused beam of helium ions, the dose of ions required to completely remove a layer of material must be calculated. The probability of removing one atom from the sample for an incident ion of a given energy was first found.

The dose of ions required to mill a volume of material from the sample is then a function of the beam energy, the particle mass, the sample composition, the sample density and the displacement energy of the sample atoms. The calculation of the dose required to remove every atom from the sample volume is a simplified scenario as it does not account for the changes occurring in the sample as damage is produced. For example the displacement energy will be reduced as damage progresses, leading to an acceleration of the rate of damage. The dose required to remove material would therefore be overestimated by our calculation. However, for 2D materials this simplification will not lead to an unreasonable error. The order of magnitude of the dose required can be found.

In the case of a sufficiently high energy ion beam the collision with the target nuclei can be described as a binary collision. For this type of Rutherford scattering the Coulomb potential can be used to accurately describe the collision[125].

The maximum transferable energy from a projectile of energy E to an atom is given by equation 3.1. The probability, $P(E)$, of a scattering event occurring between the projectile and the sample is[125]:

$$P(E) = Nx\sigma(E) \quad (3.7)$$

where Nx is the areal density of atoms and $\sigma(E)$ is the interaction cross-section. Now we consider the case of displacement collisions, where only a collision which transfers sufficient energy to the target nucleus is considered. This type of

collision is what will remove atoms from the target. T will be used to represent transferred energy. The probability that an ion will collide with a target atom and result in an energy transfer of between T_D and T_m is given by the displacement cross section:

$$\sigma_d = \int_{T_D}^{T_m} \frac{d\sigma}{dT} dT \quad (3.8)$$

where the differential cross section is given by:

$$d\sigma(E, T) = \pi \frac{M_1}{M_2} Z_1^2 Z_2^2 e^4 \frac{dT}{ET^2} \quad (3.9)$$

The integral of $d\sigma(E, T)$ from T_D to T_m is:

$$\sigma_d(E, T) = \pi \frac{M_1}{M_2} Z_1^2 Z_2^2 e^4 \frac{1}{E} \left(\frac{1}{T_D} - \frac{1}{T_m} \right) \quad (3.10)$$

The displacement cross section is then multiplied by the areal density of atoms, Nx . This gives us the probability, $P(E)$, of a displacement collision occurring. The probability is multiplied by the helium ion dose to find the displacement density of the target nuclei. If the displacement density is greater than the atomic density then that area of the sample would be entirely milled away by the beam.

The direct removal of atoms from a sample with a sub-nanometre ion beam affords a high level of sample modification control. This can be used to introduce specific defect densities, or to remove areas of material with truly nanoscale precision.

3.3.2.1 Control of the Ion Beam Milling

There are many parameters which can be adjusted to control the modification process. The HIM uses a cryogenically cooled, atomically sharp source to ionise helium gas. The helium ions are then accelerated down the column of the microscope (see figure 3.12). A series of lenses, quadrupoles and octupoles, are used to

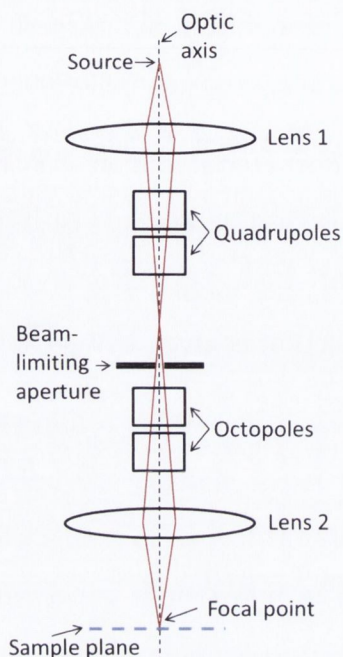


FIGURE 3.12: An illustration of the column of the helium ion microscope.

shape the beam into a <0.35 nm probe. The probe size can be measured in the same way as described for an SEM in section 3.1.2.1.

As the beam is scanned during experiments the spacing between points can be varied. If the probe size is measured to be 0.35 nm then a point to point spacing (or pixel spacing) of this value will result in each probe being adjacent with just the beam tails overlapping. This close proximity of points may be desirable where a large dose is required, such as for milling. However, if such extensive damage is to be avoided then the pixel spacing can be increased to reduce the overall dose on the exposed area. An illustration of a helium ion beam incident on a graphene lattice is shown in figure 3.13. The illustration is to scale, showing how localised the helium ion modification technique can theoretically be.

The beam current can be adjusted by either changing the strength of the condenser lens, or by changing the size of the beam-limiting aperture, as in an SEM. Both of these approaches will have an effect on the size of the probe. Typically a trade-off occurs whereby a smaller probe also has less beam current. A third option exists in

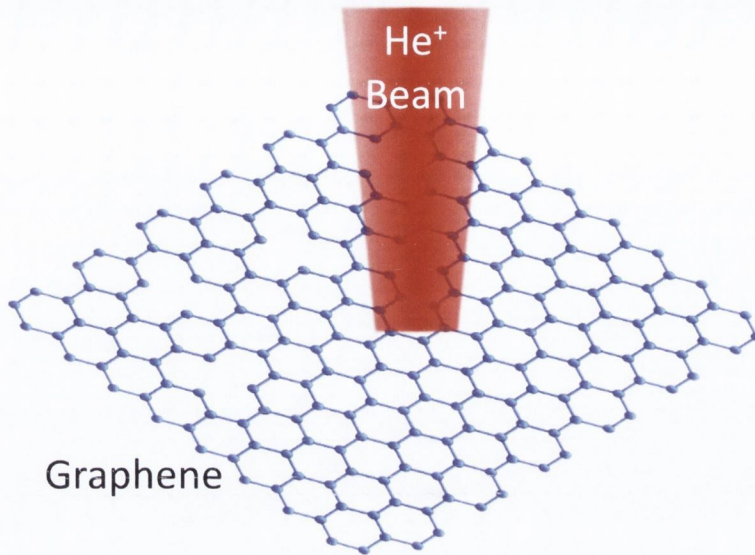


FIGURE 3.13: An illustration of the helium ion beam irradiation of graphene. The beam size is in scale relative to the graphene lattice. This shows how localised the milling process can be.

the HIM which carries no such penalty. The beam current can also be adjusted, by a couple of orders of magnitude, by changing the pressure of the helium gas in the region of the source. The time the beam spends at a point can also be controlled. This dwell time, combined with the beam current can be used to vary the dose per point. The beam energy is controllable within the range of approximately 5 to 35 keV.

Another factor to consider is the scanning strategy, or the path taken when rastering the beam over the sample. For example, Pickard[106] found that when milling nanoribbons in graphene, the two rectangles on either side of the ribbon could not be fabricated in series. The two sides had to be milled in parallel, with the beam milling a small section from one side, then the other and repeating. This strategy is illustrated in figure 3.14.

The principles of both electron beam and ion beam induced modification of materials have been discussed here. These techniques have been demonstrated to be applicable to the modification of layered materials. E-beam modification can be

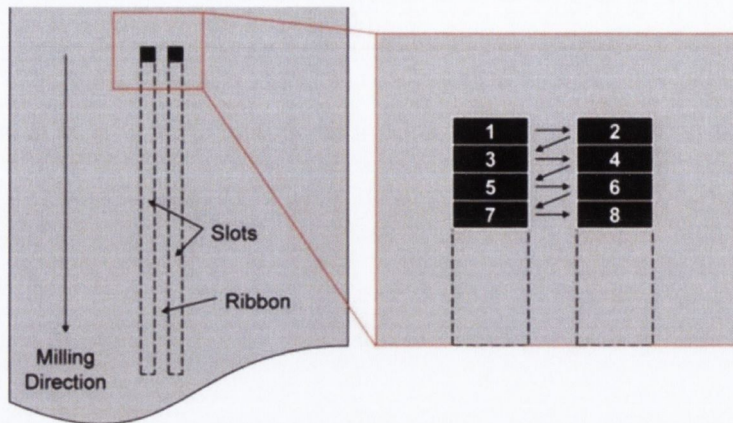


FIGURE 3.14: Illustration of the scanning strategy used by Pickard and Scipioni. The areas on either side of the ribbon had to be milled in parallel.[106]

realised with a gas assisted etching technique whereby the beam ionises the gas and also supplies energy to the sample. Ion beam modification is a more direct modification technique whereby atoms in the sample are directly ejected from their lattice position by the momentum of the beam ion.

Physical models for the processes which dominate the modification methods have been developed and described. The relevant parameters which need to be investigated in order to establish control and optimisation of these processes were outlined. In subsequent chapters these models will be compared to experimental data in order to confirm the validity of the theory presented.

In the next chapter the characterisation techniques which were used to analyse our samples will be introduced. These techniques will also be used to investigate the extent of the sample modification produced by the methods outlined in this chapter.

Chapter 4

Characterisation Techniques

In this chapter we will introduce the characterisation techniques used in this work. Our milling and modification techniques outlined in the previous chapter produce nanoscale alterations of our materials. We require techniques which can image these structural modifications at the nanoscale. We also require spectroscopic techniques which can identify the structure and composition of materials. These techniques provide the information required to understand the processes occurring in the experiments conducted.

Structural information can be provided by TEM analysis and Raman spectroscopy. Thickness information can be obtained qualitatively from transmission SEM and quantitatively from Raman spectroscopy and TEM techniques such as Scanning Transmission Electron Microscopy (STEM) and Electron Energy Loss Spectroscopy (EELS). High resolution topographical imaging was achieved using HIM and SEM. Finally, chemical analysis was obtained from Energy-Dispersive X-ray Spectroscopy (EDX) and EELS.

4.1 Scanning Electron Microscopy

The initial development of the field of electron microscopy was driven by the resolution limit of optical microscopy. The diffraction limit imposed by the wavelength of visible light is ~ 200 nm. By the late 1920's this resolution limit had already been reached. In 1931 Knoll and Ruska built the first electron lenses and used them to acquire an image with electrons[126]. Within the just a year of the first electron microscope image being produced the resolution was improved beyond that of the optical microscope.

In the scanning electron microscope (SEM) electrons are generated by a source and focused by an electromagnetic condenser lens[127]. An aperture is used to reject off-axis electrons which would otherwise lead to an increase in the final probe size. The electrons are focused on to the surface of a sample by an objective lens. The probe is not always round, an effect known as astigmatism. Octopoles in the column are used to apply a correcting field to reshape the beam. The electron probe is then rastered across the sample surface by scanning coils in the electron column. The electrons penetrate into the sample and typically undergo several collisions with both sample electrons and nuclei. Signals generated by these interactions within the sample can escape from the sample and be collected to image and characterise bulk specimens.

Modern SEMs use a field emission source which can produce a small, intense probe of electrons. The current per unit area per unit solid angle is called the brightness and is used to compare various types of electron and ion sources. The SEM electron probe can be as small as 1 nm in diameter with a brightness of 10^8 Am⁻²sr⁻¹[127]. The technique is very versatile as it can be used to image a broad range of samples.

The signals most commonly used to image in the SEM are secondary electrons (SE). These are produced by inelastic scattering. Secondary electrons can be further divided into the categories of SE₁, SE₂ and SE₃ electrons. SE₁ electrons

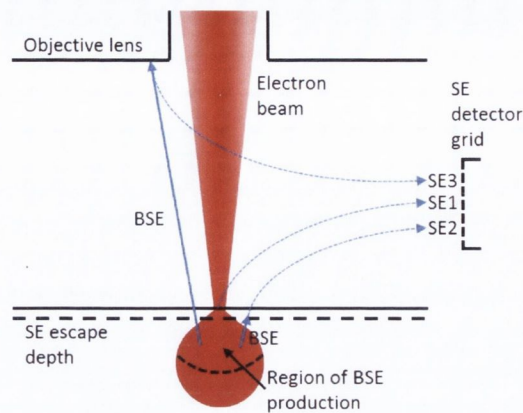


FIGURE 4.1: The interaction volume excited in a sample during SEM irradiation. The different types of electrons which can leave the sample are shown.

are generated directly by the primary beam and as such are produced from a region near the incidence point of the electron probe. SE_2 electrons are produced when the primary beam backscatters from within the sample and excites sample electrons on its way back to the surface. SE_3 electrons are generated from other surfaces within the SEM chamber by electrons which have backscattered from within the sample.

The SE_1 type electrons are generated from close to the beam interaction point on the sample. The inlens detector (also known as a through-lens detector, TLD, or a through-the-lens detector, TTL) is optimised to collect primarily this type of electron. A higher proportion of SE_2 electrons are attracted by an electric potential towards a chamber mounted SE detector. This detector was named after its inventors and is known as an Everhart-Thornley or ET detector.

Secondary electrons generated in the SEM typically have a peak in the energy distribution at about 2 - 5 eV, with a cut-off in the definition of a secondary electron at 50 eV. The low kinetic energies of secondary electrons means that they can only escape from near the surface of the sample[128]. The maximum depth from which SEs can escape is called the escape depth. In an SEM this value typically ranges from approximately 5 nm in a metal up to 50 nm for insulators[129]. SE_1

electrons are both generated within the region of incidence of the beam and are generated from near the surface.

SE₁ type electrons provide the highest resolution topographical imaging in the SEM. Contrast is generated by the variation of the secondary electron yield as a function of angle of incidence of the primary electron beam. When the electron beam is incident on the surface at a higher angle (relative to the surface normal) the amount of secondary electrons generated is increased.

SE₂ electrons are generated by BSE and so they carry less localised information. BSE are produced by the interaction of the beam with sample nuclei. They therefore carry qualitative information about the composition of the sample. SE₂ electrons also inherit this compositional information.

4.1.1 Transmission SEM

Transmission imaging mode involves the use of a transmission detector. This detector can be used to collect beam electrons which have passed through a thin sample. This mode can only be used for samples which are thin enough for most of the beam electrons to penetrate. The sample should ideally be no more than a few 10s of nanometres thick. Either electrons which transmitted straight through the sample in bright field mode, or those which have been scattered to a range of angles defined by the detector geometry in dark field mode can be used to image.

The bright-field transmission imaging mode provides contrast due to changes in composition or thickness. The collection semi-angle of the transmission detector in bright-field mode is ~ 15 mrad. Strong thickness contrast, even for flakes with atomic thickness differences can be obtained.

The resolution is also superior to any other modes of imaging available in our system (see Appendix A). The spatial resolution is 0.8 nm for a 30 keV beam energy. The main limitation of this technique is the requirement for the samples

to be very thin. Transmission SEM is ideally suited to imaging thin flakes and for observing any porous structures which they may contain due to its high spatial resolution and strong thickness contrast.

4.2 Transmission Electron Microscopy

The TEM operates by accelerating electrons to gain enough energy for the majority of electrons to pass through a thin (<100 nm) section of material. The electrons travel in a parallel beam. The formation of the beam is shown in the left schematic in figure 4.2. These electrons are typically accelerated to between 80 and 300 kV (for our TEM specifications see Appendix A). Higher voltages were historically preferred as the imaging resolution is increased and the sample need not be quite so thin. However, lower voltages are returning to favour with the use of aberration correction. Aberration correction is a relatively new field of microscopy which has enabled many new applications such as atomic resolution imaging of beam sensitive samples.

Contrast in TEM images is not always easy to interpret and can be formed by a variety of interactions. Mass-thickness contrast is the simplest to interpret and is dominant for amorphous samples. The image shows contrast because the sample either has non-uniform thickness or because some areas consist of heavier atoms than others, or both. Diffraction contrast occurs when the electron beam is incident on an atomic plane at a special (Bragg) angle. When the spacing of the atomic planes and the beam angle satisfy the Bragg equation the electrons constructively interfere. If an objective aperture is used (see figure 4.3) these scattered beams create contrast in the image which is related to the arrangement of the crystal at this location.

The diffracted beams constructively interfere to create diffraction patterns. These diffraction patterns can also be recorded in the TEM (see figure 4.3) and are a

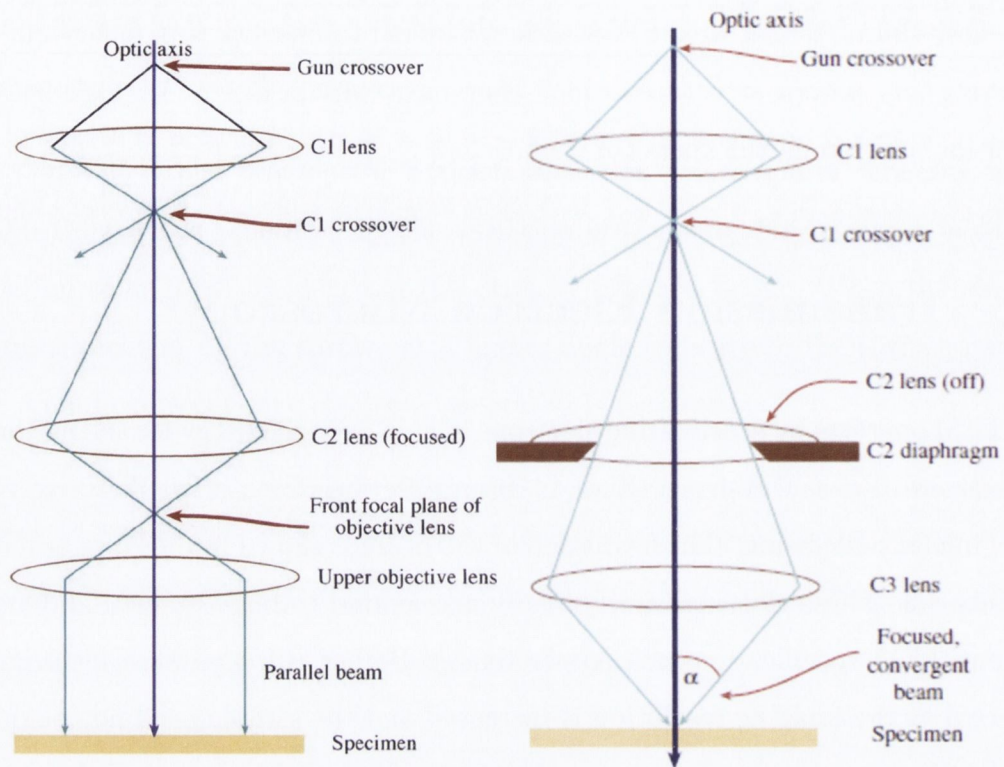


FIGURE 4.2: The illumination system of a TEM. Parallel illumination of the sample (TEM mode) is shown on the left while a focused probe on the sample surface (STEM mode) is shown on the right[130].

powerful technique to determine the spacings and orientations of the planes within a crystal. The Bragg equation which defines this relationship is $n\lambda = 2d \sin \theta$, where n is an integer, λ is the de Broglie wavelength of the electron, d is the spacing between atomic planes in the crystal and θ is the scattering angle of the beam. When $\theta = \theta_B$, the Bragg angle, constructive interference occurs and a diffraction spot is observed in the back focal plane¹, for a crystalline sample. The electrons are scattered to a larger angle by more closely spaced atomic planes. They will therefore appear further from the position of the direct (unscattered) beam in the diffraction pattern. The angular position of the diffraction spot in the diffraction pattern is used to determine the orientation of the atomic planes.

Phase contrast occurs due to the differences in the phase of the electron waves after propagating through the sample. Phase contrast can be used to image the

¹The plane where the objective aperture is found in figure 4.3.

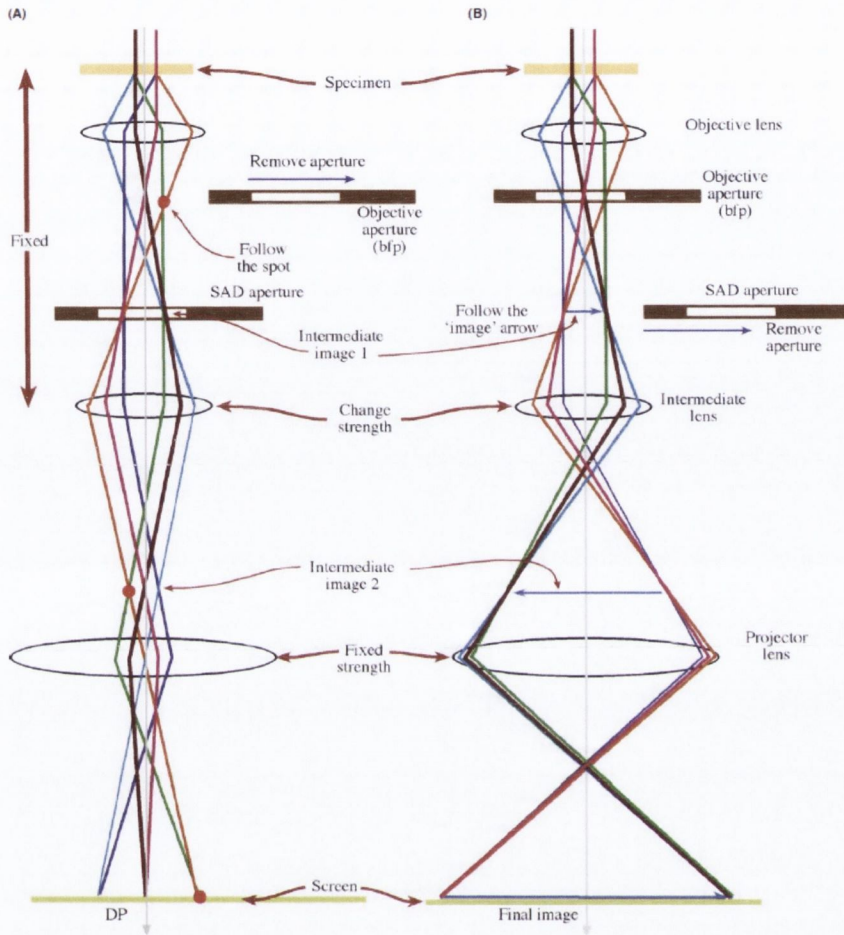


FIGURE 4.3: The projection system of a TEM. The formation of a diffraction pattern on the viewing is shown in (a) while an image is formed on the screen in (b)[130].

atomic structure of a sample, if the resolution of the instrument is sufficient and the sample is thin enough (tens of nanometres). If the resolution is not sufficient then artefacts such as edge delocalisation, where extra lattice fringes are seen beyond the real edge of a crystal, may be observed. Phase contrast imaging is very sensitive not only to the sample but also to the operating conditions of the microscope.

The electron beam in conventional TEM mode is parallel and in phase before reaching the sample. After passing through the sample the exit wave contains information about the sample. The objective lens then adds spurious information

to this wave due to the lens imperfections. This makes these images difficult to interpret and computer simulations are required to understand the contrast. Exit wave reconstruction attempts to remove the artefacts from the final image and reproduce the true exit wave. One technique used to achieve this is focal series reconstruction. A series of images are captured (twenty is usually sufficient) at incremental values of defocus[131]. These images along with the operating parameters of the microscope and constant values such as the spherical aberration constant (C_s) of the objective lens are then combined to reproduce the electron exit wave. For our TEM the focal series reconstruction method can result in an improved resolution of the reconstructed image[132]. With this technique resolution down to 0.5 Å can be achieved.

4.2.1 Scanning Transmission Electron Microscopy

In Scanning TEM (STEM) mode the electron beam is focused into a probe at the sample plane (see the right schematic in figure 4.2) and rastered across the surface, much like in an SEM. Material (Z) contrast imaging can be used to image the atomic structure of a specimen. In Z contrast imaging the electrons which are scattered to high angles (50–150 mrad) by a nuclear (elastic) interaction are detected. STEM mode can be used with a high-angle annular dark field (HAADF) detector to exploit Z contrast for imaging[133].

HAADF imaging can resolve the atomic structure of a sample in an easily interpretable image. Software packages which must be used to interpret phase contrast images are not required in HAADF imaging. The contrast in the image shows atoms as bright areas (areas of higher intensity) and the inter-atomic spacings as darker areas. Heavier atoms (higher Z number) display a higher intensity with the intensity scaling as Z to the power of ~ 1.7 [134]. A column of atoms produces an intensity which is directly proportional to the number of atoms in the column.

The probe of electrons formed at the sample plane must be sufficiently small to provide the necessary resolution for atomic scale imaging. This probe must also have sufficient brightness to provide a reasonable signal to noise level. A high brightness (i.e. field emission) source is a prerequisite for high resolution STEM, and aberration correction of the probe forming optics is greatly advantageous. With such developments STEM can now be used to analyse single atoms[135]. Sample requirements for STEM, specifically atomic resolution STEM, are even more demanding than for typical TEM samples. The thickness must be no more than a few nanometres, otherwise the beam broadening within the sample will limit the resolution.

We use STEM to image with easily interpretable thickness contrast. We can also avoid edge delocalisation which occurs in TEM mode due to lens aberrations. This allows us to more clearly observe the edge structure of our samples. The more simple contrast mechanisms in STEM also limit the information which can be achieved by this technique. Diffraction contrast and defect observation, for example, are more commonly done in TEM mode.

4.2.2 Electron Energy Loss Spectroscopy

In EELS a beam of electrons with a very narrow range of kinetic energies enter the sample. These electrons are then filtered and analysed after interacting with the sample. In a thin sample most electrons lose no energy, however some will interact with the sample in an inelastic collision. The energy lost in this interaction is dependent on a range of factors such as the chemical species of the elements and their electronic structure. The energy spectrum of the electrons is resolved by a magnetic prism. The EELS spectrum has three main features.

The Zero Loss Peak (ZLP) contains electrons which have lost no detectable energy in the sample, this peak is shown in figure 4.4[136]. The plasmon peak contains electrons which interact with outer shell electrons in the sample and are found at

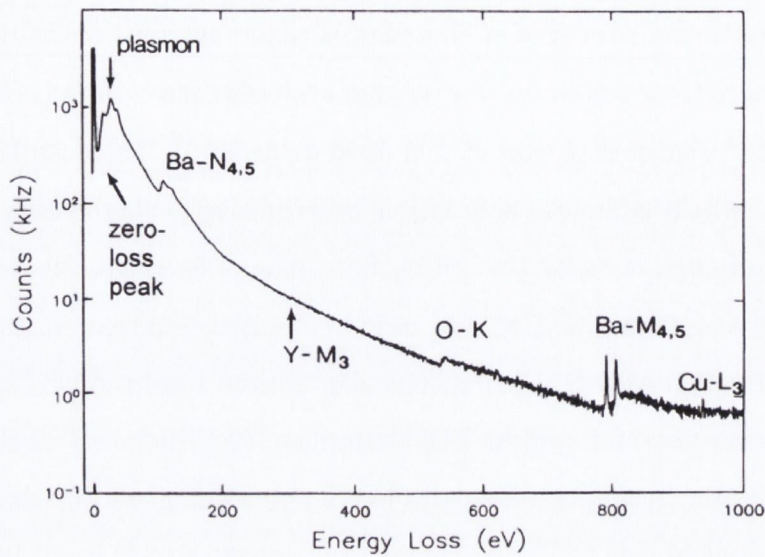


FIGURE 4.4: Electron energy-loss spectrum of a high-temperature superconductor (YBa₂Cu₃O₇) with the electron intensity on a logarithmic scale, showing zero-loss and plasmon peaks and ionization edges arising from each element [136].

5 - 50 eV energy loss. A plasmon is a collective, resonant oscillation of valence electrons, the plasmon peak gives information about the density of the valence electrons.

Characteristic edges contain electrons which interact with core shell electrons, resulting in sharper edges corresponding approximately to the binding energy of the sample electrons. This binding energy is characteristic of the sample atom, allowing us to identify the composition of the material under investigation. The concentration of this element in the sample can also be found by integrating the area under the characteristic edge.

Within ~ 50 eV of the characteristic edge a fine, near-edge structure is observed. This region is known as the Energy-Loss Near-Edge Structure (ELNES). The near edge structure gives information on the local structure and bonding, for example EELS can differentiate between graphitic carbon and diamond-like carbon. The extended region beyond the ELNES is known as the Extended Energy-Loss Fine Structure (EXELFS). In the EXELFS region a weak periodic oscillation may be

observed, this can be used to determine the bonding distance and radial distribution of near neighbours. EELS is a very powerful technique which can provide a substantial amount of information from a sample. With the introduction of monochromated TEMs the meV range of energy loss can now be probed by EELS, wherein lattice vibrations (phonons) can be probed.

Energy-filtered images can also be acquired. In this mode the electrons which have lost energy within a certain range are selected to form an image. Energy-filtered TEM (EFTEM) can produce maps of the distribution of different elements. Plasmon energy-filtered images provide thickness contrast imaging. For graphene a 15 eV energy window centred on the 25 eV plasmon energy loss peak can be used. As the plasmon excitation cross section is high we get images with greater thickness resolution than standard bright field imaging. This is due to the removal of the noise from the ZLP[137].

4.2.3 Energy-Dispersive X-ray Spectroscopy

EDX exploits the fact that element characteristic X-rays are produced during electron beam irradiation of a sample. When an electron with sufficient energy interacts with a core-shell electron it can transfer sufficient energy to the sample electron to excite it to an unfilled higher energy level. The atom becomes ionised and is left in an excited state. This excited state is unstable and the excited atom will decay back to its ground state through the transition of an outer shell electron to the inner shell vacancy. The energy can be released as an X-ray photon. The energy produced in this relaxation process is characteristic of the atomic species involved in the process.

This characteristic X-ray can be detected by an EDX detector within the microscope chamber allowing material characterisation to be performed. X-ray production also occurs over a broad energy range due to the slowing down of the electron

in the sample. These X-rays produce a background signal on which the characteristic X-rays are superimposed. These X-rays are known as bremsstrahlung, or braking-radiation. They contribute no characteristic information to the spectrum.

An array of EDX analysis points on a sample can be used to form an image of the distribution of the various elements within a sample. The concentrations of the elements within the sample can also be determined. Detection of elements down to ~ 0.1 atomic % with an accuracy of approximately 5 % [138] is typically achievable.

4.3 Helium Ion Microscopy

The most recent major development in the field of ion microscopes was the helium ion microscope (HIM) which was commercialised by Carl Zeiss in 2007. The HIM is a new charged beam microscope with unique applications. The HIM finds itself somewhere between an SEM and a FIB, but with advantages over both. The resolution of the tool surpasses what is typically achievable in bulk sample imaging with an SEM. Material removal is also possible, but with much higher precision than a FIB.

Probe size and resolution are two strongly related terms, however the difference is important when comparing SEM and HIM. The resolution is not only dependent on the size of the probe which the optics can form, but also the volume of the sample from which the signal is generated. Petrov and Vyvenko [139] demonstrated that the secondary electrons generated by 30 keV helium ions have a narrower energy distribution peaking at lower energy compared to those generated by 30 keV electrons. The energy distribution of these secondary electrons is shown in the graph in figure 4.5. The majority of secondary electrons produced by the 30 keV helium ion beam have an energy of less than 2 eV. This results in the mean escape depth of the secondary electrons produced by helium ions being limited to

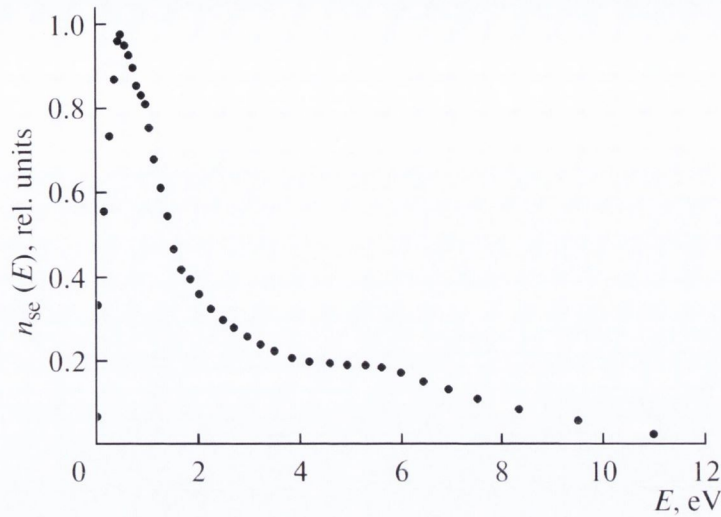


FIGURE 4.5: A graph of the secondary electron energy distribution in a HIM operating at 30 kV[139].

typically 2 nm or less[140, 141] resulting in greater surface sensitivity than SEM imaging.

In the HIM the backscatter yield of ions from the sample is very low, typically 1% or less, especially for low Z materials. This also results in a low SE_2 yield. SE_1 electrons are the dominant signal produced in the HIM and, as we have already discussed in section 3.1 of this chapter, SE_1 electrons provide the highest resolution SE imaging. The HIM was primarily used for sample milling and modification in this work. However, it is clearly capable of providing high resolution imaging as well.

4.4 Raman Spectroscopy

A technique which can provide a value for the density of defects over a micron sized area of graphene was required. This was necessary to assess the extent of the damage introduced by various doses of helium ions. The thickness of the graphene sample also needed to be confirmed. Raman spectroscopy was selected as it is a fast, non-destructive technique which can provide this information[142].

Raman spectroscopy is an optical characterisation technique which can be used to probe the vibrational modes of crystal structures. A monochromatic beam of photons (a laser) is focused onto the sample. Photons are absorbed by the sample and are then emitted after a short period. The emitted photons can have a shift in energy relative to the incident photon which is characteristic of a particular phonon mode within the sample. The emitted photons are collected with a lens and sent through a monochromator to separate them based on their energies. A spectrum of the energy shift, or Raman shift, is produced.

For a perfect crystal structure with Raman active phonon modes several sharp well defined peaks will be observed. These peaks may shift due to sample doping or change in intensity due to symmetry breaking in the crystal structure. Other modes may also become Raman active within the crystal as the structure is modified. For example, defective graphene displays a D peak which is not present in the pristine form of the crystal. Raman spectroscopy can therefore be used to identify the extent of the defects within a graphene sample. The Raman spectrum is also sensitive to the stacking of layers. A measure of the thickness of thin, layered materials, such as graphene[143] and MoS₂[18], can be made with single layer resolution. If the sample stage is electronically controllable then a Raman map of the surface can be created. This can be used to show the distribution of defects or the thickness variation across the sample.

The most prominent features of the Raman spectrum of graphene are the characteristic G peak at $\sim 1580 \text{ cm}^{-1}$ and the 2D peak at $\sim 2700 \text{ cm}^{-1}$. A third peak, the D peak at $\sim 1350 \text{ cm}^{-1}$, becomes Raman active in defective graphene. In the low defect density regime the ratio of the D peak intensity to the G peak intensity (I_D/I_G) is proportional to the defect density[144].

The Raman spectra of graphene samples of different thicknesses are shown in figure 4.6[145]. Single layer, bi-layer and few-layer spectra are shown. Single layer graphene has the smallest G peak to 2D peak intensity ratio. This ratio grows as

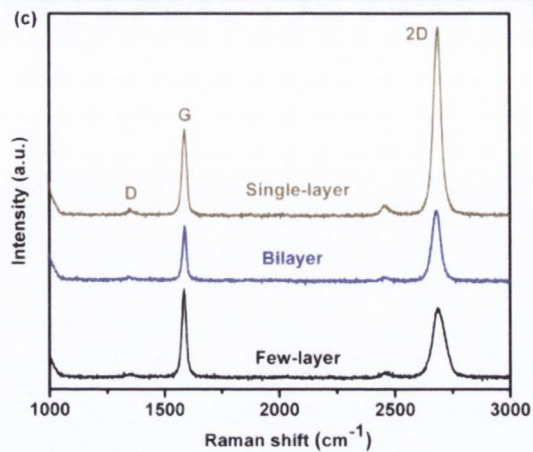


FIGURE 4.6: Raman spectra of graphene samples with different thicknesses.

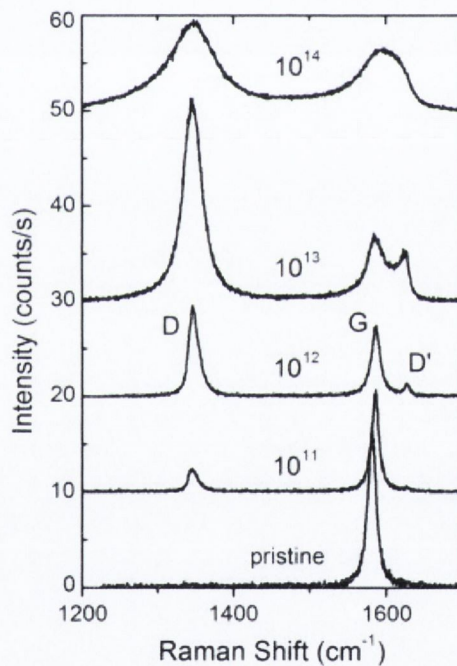


FIGURE 4.7: Raman spectra of graphene samples with different densities of defects.

the sample thickness increases. The 2D peak is also observed to broaden as the number of graphene layers increases.

Pristine and defective graphene spectra are shown in figure 4.7[59]. The 2D peak is not shown in this energy range. The bottom spectrum is from pristine graphene. The spectra further up in the image get progressively more defective. As the material becomes more defective a new peak, the D peak, is observed to grow on

the left hand side. A second defect related peak, the D' peak also appears to the immediate right of the G peak. The ratio of the D peak to the G peak intensity can be used to estimate the density of defects in the sample[144]. At very high defect densities the peaks in the spectra broaden and the defect density can no longer be estimated by this ratio. The material has become highly defective at this point.

For graphene analysis by Raman spectroscopy a 633 nm HeNe laser, a 100× objective lens and a diffraction grating with 1200 lines mm^{-1} were used. The time used to acquire a spectrum with a good signal to noise ratio from a point on the sample was 10 s. For greater signal several spectra can be averaged.

The simplicity and speed with which Raman spectroscopy can probe the structure of graphene make it a highly useful and widely adopted technique. The main limitations of this technique are the time it takes to produce a Raman map of the sample and the resolution of the technique which is limited by the laser spot size, typically $\sim 1 \mu\text{m}$.

The characterisation methods discussed here have been demonstrated to have broad applicability to the investigation of modified layered materials. These techniques facilitate the analysis of sample composition, topography, structure, geometry, and thickness. In the next chapter the results of the experiments on focused electron beam etching of graphene in a gas environment will be described in detail.

Chapter 5

Gas Assisted E-beam Etching of Graphene

In this chapter the use of a low energy (<10 keV) focused electron beam to etch graphene will be described. The electron beam was used to supply the energy required to facilitate a graphene-nitrogen reaction. This reaction causes carbon atoms to be removed from the sample within the region of the beam. Nanopores were created by this process. This approach has the benefit of confining the nanopore generation to a nanoscale region.

The effect of the various parameters on the etching process will be assessed. These parameters include, the electron probe size, the beam dwell time, the beam current, the beam energy and the gas pressure. The resulting microstructure modification will be analysed by TEM. The model for the etching process will also be verified.

5.1 Etching Experiment

Chemically exfoliated few-layer graphene was prepared in solution as described in section 2.2. The solution was dropped onto a lacey carbon support film on a TEM

grid and left to dry in air overnight. In each etching experiment the electron beam was focused onto a spot of ~ 5 nm on the surface of the graphene flake. A nitrogen flux was delivered directly to the adjacent region of the beam-sample interaction spot through a nozzle. The flux was adjusted by monitoring the gas pressure in the SEM chamber. Etching of the graphene was studied as a function of beam dwell time, nitrogen gas pressure, beam current and beam energy.

The damage to the graphene by the etching was studied by measuring the area of material removed from each exposed region after the experiment. This etched area was calculated by taking an image of the flake in transmission mode in the SEM and converting it to binary, i.e. black and white, using ImageJ. One such binary image is shown inset in figure 5.1(d). A histogram of the area was then used to find the number of black pixels. As the scale of each pixel is known the size of the holes etched in the material can be calculated.

The TEM was operated at an acceleration voltage of 80 kV to analyse the effect of the etching process on our sample while minimising the damage introduced[77]. As well as standard TEM imaging, focal series reconstruction and energy-filtered TEM (EFTEM) were used to analyse the sample after etching. EFTEM plasmon imaging, as described in section 4.2.2, was used to resolve the sample thickness with monolayer precision[137]. For this technique we apply a 15 eV energy window centred on the 25 eV plasmon energy loss peak of graphene.

5.2 Results and Analysis of the Etching Process

Figure 5.1(a) is an SEM image of a typical graphene flake before etching experiments. It shows uniform contrast, indicating the same thickness, across an area of up to $1 \mu\text{m} \times 1 \mu\text{m}$. Deposition of carbon contamination was initially observed to occur before introducing nitrogen gas into the chamber. The contamination appeared as bright circular features, as shown in figure 5.1(b). The nitrogen gas

flow was then turned on. Partial etching of three areas on a flake is shown in figure 5.1(c). However, the rate of etching was not fast enough to etch through all of the layers of the sample before the area drifted out of the region of the beam probe. The drifting was obvious due to the elongated shape of the etched areas. This is typical of thicker flakes, thin flakes (typically <3 layers) were therefore selected for our experiments. This drifting is typically due to inherent instabilities in the stage and was unavoidable.

Some contamination was also observed around the edges of the etched area. Successful etching through a flake is shown in figure 5.1(d). Holes of several tens of nanometres in diameter can clearly be seen to have been introduced in the graphene flake. There are nine such holes in the flake corresponding to nine electron beam conditions. The inset is an image of the holes after converting the image to binary. The binary image was used to calculate the area of material removed by the etching process.

The effect of the nitrogen gas on the etching was investigated by varying the pressure of the nitrogen gas in the system. The dwell time was set to 30 s. Five adjacent regions on the same flake were irradiated at different gas pressures. The images of the effect of the exposure at 55 pA beam current are shown in figure 5.2(a) with the lowest gas pressure at the bottom. In figure 5.2(b), with a fixed beam current of 55 pA (black squares), etching occurred when the nitrogen pressure was higher than ~ 250 mPa. Above this value the etching rate was positive. Hydrocarbon contamination was observed at a lower pressure. The deposition was graphed as negative etching rate. The increasing nitrogen pressure was observed to suppress hydrocarbon contamination and enhance etching.

The experiment was then repeated with larger beam currents. At a beam current of 70 pA (red circles in figure 5.2) deposition of contamination at low nitrogen pressure was not observed. At 700 pA (blue triangles) etching was again observed to occur, but at a faster rate. In all cases the etching rate was observed to increase with increasing nitrogen pressure. It was found that the etching rate was linearly

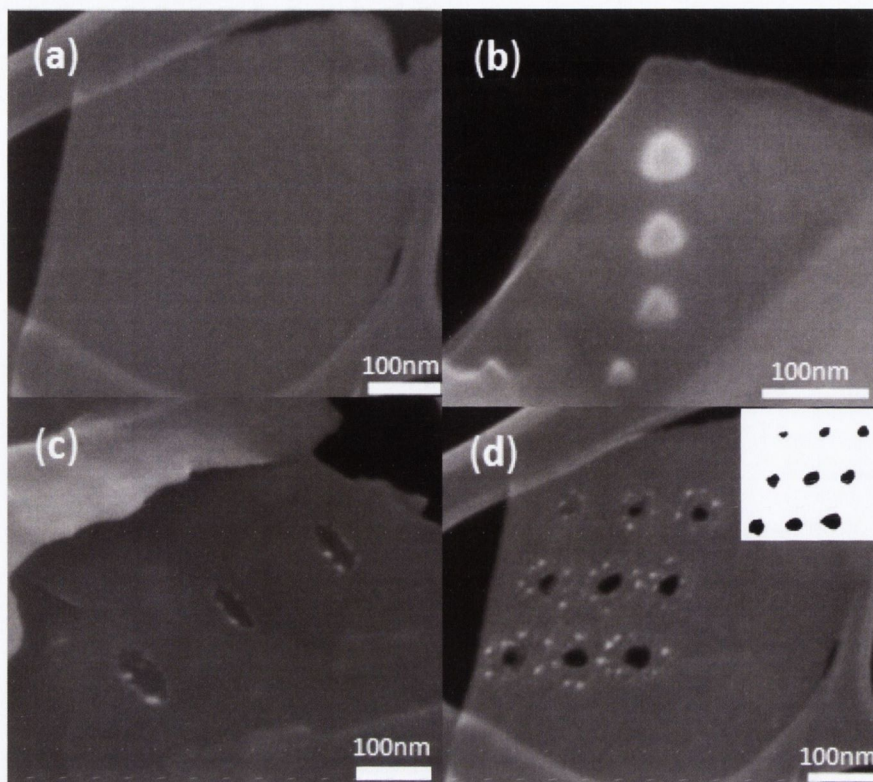


FIGURE 5.1: (a) SEM image of a graphene flake before etching. (b) Four spots of beam deposited carbon before the nitrogen gas was introduced. (c) Three partially etched regions. (d) Nine holes etched into a flake, each under different conditions. Inset is the binary image used to calculate the size of the etched areas.

dependent on the nitrogen pressure within our experiments. For the following experiments the nitrogen pressure was fixed to approximately 300 mPa.

The beam dwell time effect was studied by observing the amount of material etched for a range of dwell times. The dwell time refers to how long the electron beam probe was left focused on a single spot on the sample. A fixed nitrogen pressure (~ 300 mPa) and beam current (~ 180 pA) were used. The experiment was conducted on two flakes. As shown in figure 5.3, the etched areas of the two flakes both increased approximately linearly as we increased the dwell time. The etching rates of the two flakes measured, i.e. the slopes of the two curves, are however different, 5.2 ± 0.6 nm²/sec (blue squares) and 2.7 ± 0.3 nm²/sec (open circles) for samples 1 and 2 respectively. This can be attributed to the different

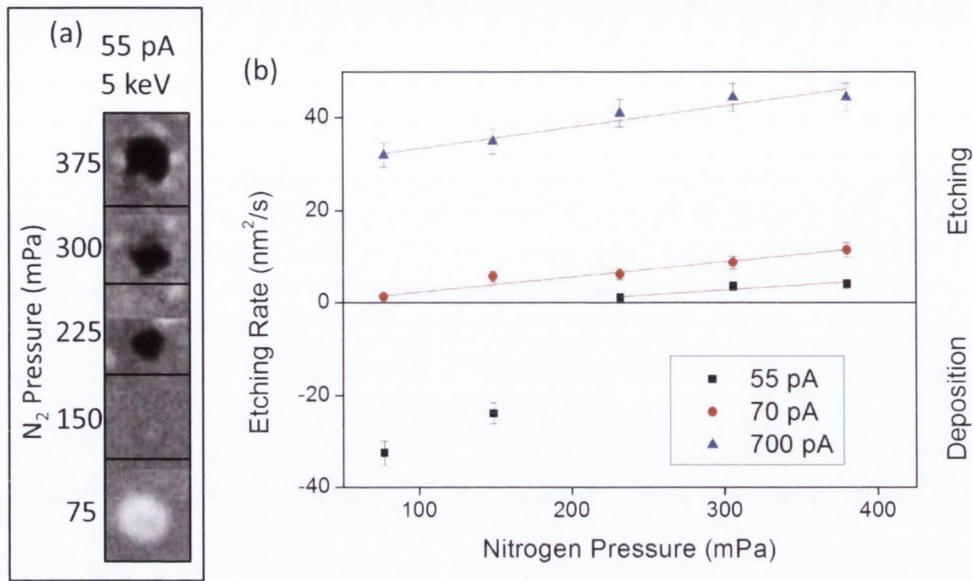


FIGURE 5.2: An example of the deposition and etching observed at different nitrogen gas pressures is shown in (a), a 55 pA beam current and 5 keV beam energy were used. (b) At the lowest beam current (55pA, black squares) hydrocarbon contamination was initially observed. Upon increasing the nitrogen gas pressure the deposition was observed to be suppressed, etching then began to dominate. The rate of etching grows with higher gas pressure. The effect of nitrogen gas pressure on the etching rate was also observed at beam currents of 70 and 700 pA.

thicknesses of the flakes used and it indicates that the number of layers in the flake had an effect on the etching rate. Nevertheless, the etching rate was constant for a given flake within the duration of the experiment (< 180 sec).

The effect of the beam current on the etching rate was investigated. Initially at a very low beam current range, 10 pA - 40 pA, (figure 5.4(a)) the deposition of contamination was observed, graphed as negative etched area. When the beam current continued to be increased etching was seen to dominate. The etching rate then increased as the beam current continued to be raised. In figure 5.4(b) a further increase was observed in the etching rate with larger beam currents (~ 300 pA)¹

¹It has been found that the etching rate depends on the size of the electron beam probe, especially at a low current range. To exclude this effect, the probe size was monitored and controlled at each beam current. A value of 6.5 ± 3.1 nm was recorded, this probe size variation is negligible and was discounted as a contributing factor to the etching rate.

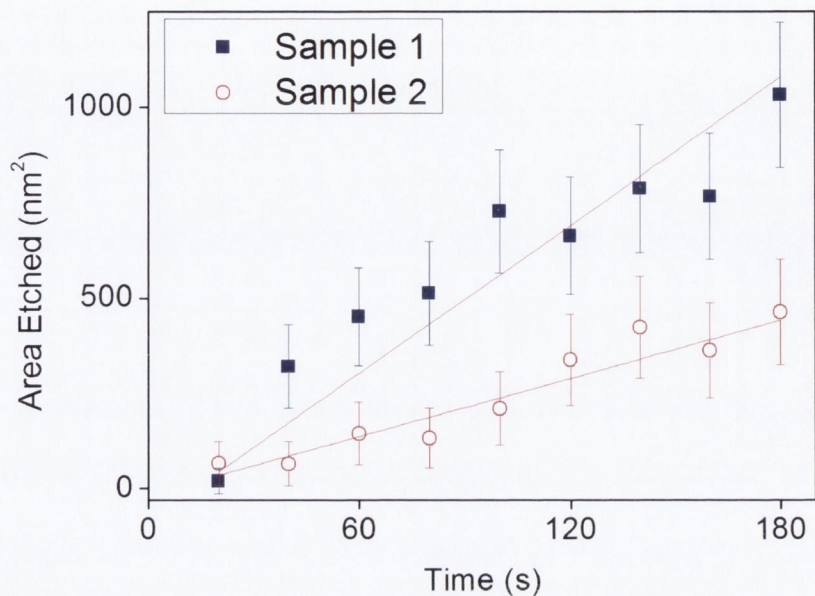


FIGURE 5.3: A linear increase in the amount of material etched at longer dwell times was observed. The different etching rates for the two samples was attributed to their different thicknesses.

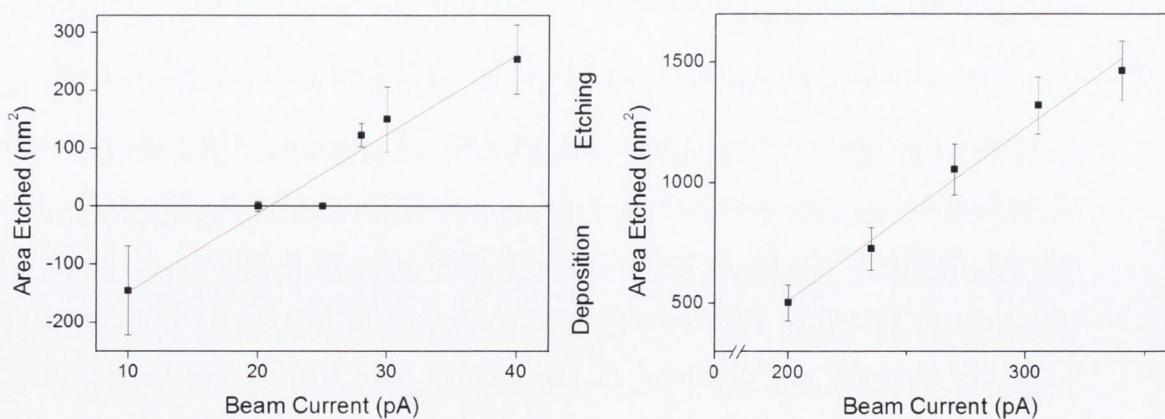


FIGURE 5.4: The transition from deposition to etching at higher beam current is observed in (a). A higher rate of etching occurs with increasing beam current, as is evident from (b).

The energy of the electron beam was also observed to have an effect on the etching rate. The energy was increased from 2 keV to 10 keV with a step of $\Delta E = 2$ keV. During this experiment the beam current (240 pA), the nitrogen pressure (300 mPa) and the probe size (~ 11 nm) were maintained at constant values within the error of the experiment. The image from which the data was taken is shown in figure 5.5(a). This image shows a flake of graphene with five holes etched using five different electron beam energies. The area of each of the holes versus the electron beam energy was graphed in figure 5.5(b). It was apparent from the experimental data that the etching rate was strongly dependant on the beam energy. A large increase in etching rate was observed for lower energy electrons.

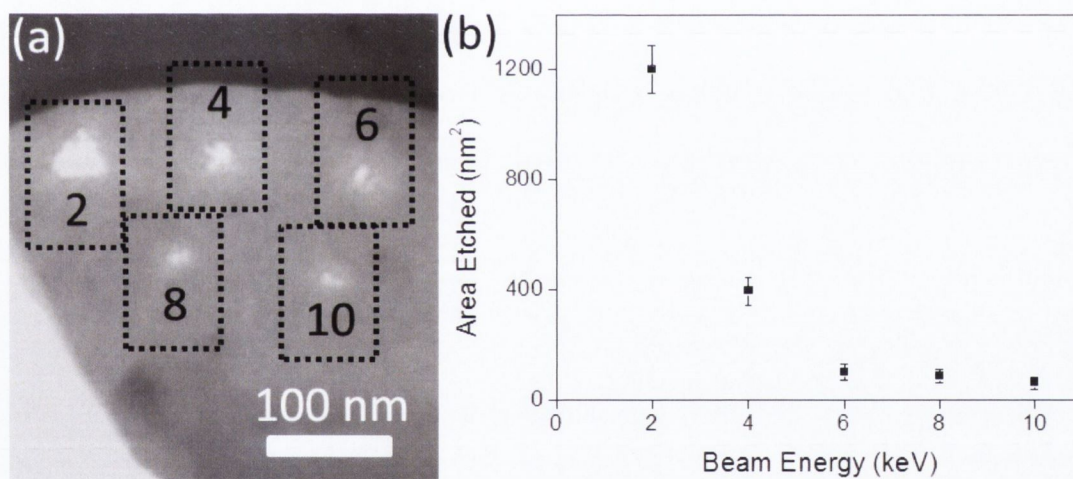


FIGURE 5.5: (a) Transmission SEM image of a graphene flake etched in five different areas by five different electron beam energies. The energy used to etch the adjacent hole is indicated in units of keV. (b) Graph of the etching rate of graphene as a function of the incident electron beam energy. A sharp increase in the etching rate at lower beam energies was observed.

Below is a summary of the effects of the different parameters within the system on the etching.

Nitrogen gas No etching without the gas. Linear increase in etching rate as gas pressure was increased.

Beam dwell time Linear increase in etched area with increasing dwell time.

Etching shown to be slower with thicker flakes.

Beam current Linear increase in etching rate as beam current was increased.

Beam energy Large increase in etching rate for lower beam energies.

It was described in section 2.5.2 that an electron with sufficiently high energy (>86 keV) can cause removal of material by a physical sputtering process. The process occurring here follows the opposite trend to this mechanism, lower energy electrons cause more material removal. It is therefore not knock-on damage which causes the etching observed here.

The effect of the beam heating on the sample was first considered as a mechanism for the material removal process. If the electron probe could heat the exposed region significantly then ablation of the carbon could be occurring. The sample temperature was estimated by using the model outlined by Reimer and Kohl[146]. Using the surface plasmon interaction we found the probe of the SEM to introduce a temperature of ~ 387 K, far below the sublimation temperature of $\sim 4,000$ K for graphite.

The kinetic energy of the nitrogen molecules was also considered using $\frac{3}{2}k_B T$, which should be appropriate at this pressure. At only ~ 0.03 eV their kinetic energy is insufficient to cause damage to the graphene lattice, as described in section 2.5.2. Even if the nitrogen is in thermal equilibrium with the beam electrons (1,800 K) their kinetic energy would still only be 0.155 eV. This is far below the ~ 20 eV required to displace carbon from its lattice position.

The results can be explained by the low-energy e-beam activated gas etching model proposed in section 3.1.2. This model attributes the etching process to a combination of two factors. Thermal energy is supplied to the graphene sample by the electron beam, thereby lowering the activation barrier for the carbon-nitrogen reaction to occur. The electron beam also ionises the nitrogen gas, creating a substantially more reactive species of nitrogen.

Equation 3.6 ($A(E) = Rt$) predicts this behaviour as the area etched was calculated to be proportional to the time of exposure. This equation describes the etching probability per interaction. It is therefore reasonable that the amount of nitrogen, as well as electrons, had a linear relationship with the etching rate.

The effect of the energy of the electron beam on the rate of etching is less clear. The etching model proposed must be able to explain this effect. Equation 3.5 predicts a higher rate of energy transfer to the etching process as the electron beam energy is reduced. This increased energy transfer occurs due to both the higher nitrogen ionisation cross section and the stronger beam-sample interaction at lower beam energies. Due to these combined effects the etching rate will rise sharply with decreasing beam energy.

First, equation 3.3 was used to find the ionisation cross section of nitrogen gas as a function of the electron beam energy. For the nitrogen molecule there are four molecular orbitals. The orbital values for B and U defined by Hwang *et al.*[117] were used. The ionisation cross section from each of the orbitals was added to get the total ionisation cross section for a given electron beam energy. The ionisation cross section of a nitrogen molecule for a 2 keV electron is shown in table 5.1. The total ionisation cross section is, $\sigma_i = 0.521 \text{ \AA}^2$.

Orbital	B (eV)	U (eV)	N	$\sigma (\text{\AA}^2)$
$2\sigma_g$	41.72	71.13	2	0.04189
$2\sigma_u$	21.00	63.18	2	0.09585
$1\pi_u$	17.07	44.30	4	0.2468
$3\sigma_g$	15.58	54.91	2	0.1366

TABLE 5.1: Table of the constants of each of the orbitals of the nitrogen molecule[117]. The ionisation cross-sections, σ , of each orbital for a 2 keV incident electron are listed.

The ionisation cross section values for each of the energies used in our experiments were then calculated. The values are plotted in figure 5.6 as blue circles. This data can be fitted by the exponential relationship: $\sigma_i(2 - 10 \text{ keV}) =$

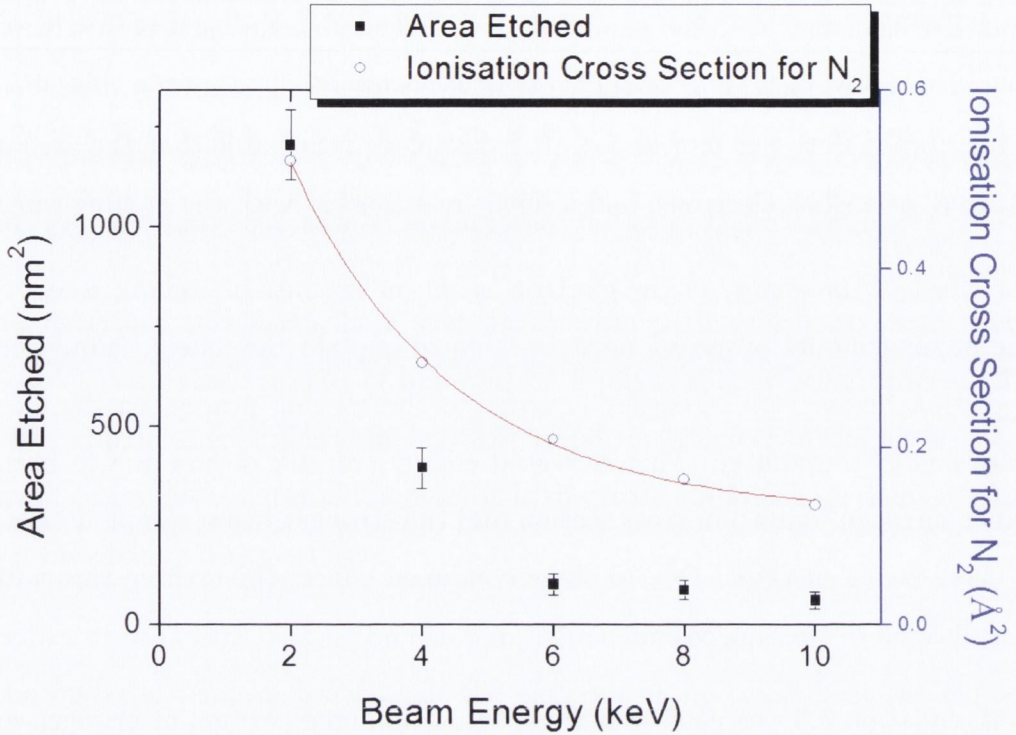


FIGURE 5.6: A logarithmic increase in the calculated ionisation cross section of nitrogen gas (blue circles) occurs as the energy of the electron beam is reduced. The experimental data from figure 5.5 is shown as black squares.

$\exp(-0.066)E_i^{-0.84} \text{Å}^2$. This fitting describes the ionisation cross section as a function of the electron beam energy, over this data range only.

The experimental etching data from figure 5.5 is re-plotted in figure 5.6 as black squares. It can be seen that in terms of the electron beam energy dependence, the experimentally observed etching behaviour (black squares) deviates qualitatively from the nitrogen ionisation model in figure 5.6 (blue circles). This indicates that the etching mechanism is also regulated by other physical processes.

The amount of energy transferred from the electron beam to the graphene as a function of beam energy is given by equation 3.4. The values for carbon were substituted into the equation ($Z = 6$, $\rho = 2.1 \text{ g/cm}^3$ and $A = 12.01 \text{ g/mol}$). The parameter E_i is equivalent to the beam energy E as we are using an atomically

thin target. The equation then becomes:

$$\frac{dE}{ds} (keV nm^{-1}) = -\frac{8.24}{E} \ln \left[11.66E \left(1 + \frac{0.0784}{E} \right) \right] \quad (5.1)$$

The ionisation of the nitrogen molecule and the thermal energy transfer to the graphene sample are two independent processes. Their effect on the overall etching rate is therefore simply described by the product of the probabilities of these two events.

$$R (nm s^{-1}) = k \exp(-0.06563) E^{(-0.8385)} \frac{8.24}{E} \ln \left[11.66E \left(1 + \frac{0.0784}{E} \right) \right] \quad (5.2)$$

This equation can then describe the experimental data recorded quantitatively. The only fitting parameter is the proportionality constant k , which represents a one dimensional etching rate per thousand eV of energy of the electron beam. This model is used with $k = 1.32 \text{ nm s}^{-1} \text{ keV}^{-1}$ to plot the dashed curve in figure 5.7. The curve is in good agreement with our experimental data points shown in figure 5.7. This result indicates that the etching rate is dominated by the probabilities of nitrogen ionisation and beam-graphene interaction in this system and the combined effect of these two processes determines the etching rate observed experimentally.

The linear enhancement in etching rate due to a higher gas pressure, a higher beam current and a longer beam dwell time can all be explained by this model. For example, if there are more nitrogen ions, more reactions with the graphene surface can occur. An increase in either the nitrogen gas pressure or the electron beam current will lead to an increase in the rate of nitrogen ion production. An increased irradiation time will also produce more nitrogen ions.

The experimental and theoretical analysis corroborates the chemical etching model which we proposed in chapter 3. Nitrogen ions react with the activated graphene surface to form a gaseous product (such as cyanogen, $(CN)_2$ [147]) and carbon atoms are removed initially. The vacancies which these leave behind cause the

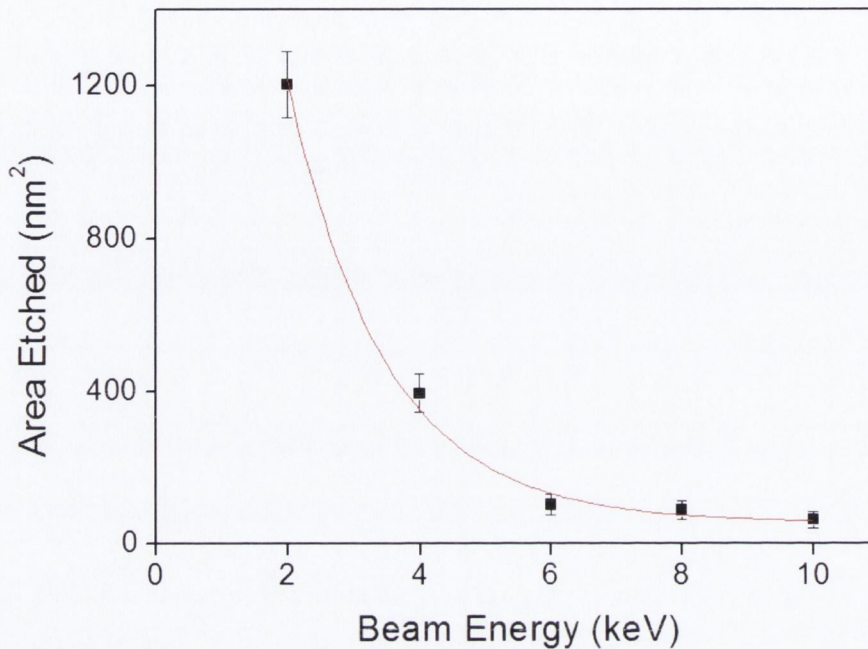


FIGURE 5.7: The line is a fitting of the model introduced in section 3.1. The black squares are the experimental data points from figure 5.5.

neighbouring atoms to rearrange due to surface tension. This disordered region has a reduced activation energy leading to an enhanced etching rate. These areas grow into pores. The density of pores is greatest at the point of incidence of the electron beam, leading to a hole forming at this location in the material.

HR-TEM images enhanced by focal series reconstruction are shown in figure 5.8(a) and (b). Figure 5.8(a) is an image of a region of pristine graphene. Figure 5.8(b) shows the structure of the lattice of graphene adjacent to an etched region. The graphene lattice undergoes structural disorder and amorphisation by these processes, leading to the worst affected areas growing into the pores which were observed in figure 5.8(c) and (d).

A hole was formed where the electron beam was centred due to a large density of these pores. Nitrogen ions diffuse from the region of the electron beam and damage an area much larger than the beam spot size. The size of the electron probe is indicated by a red spot at the centre of the etched area in figure 5.8(d).

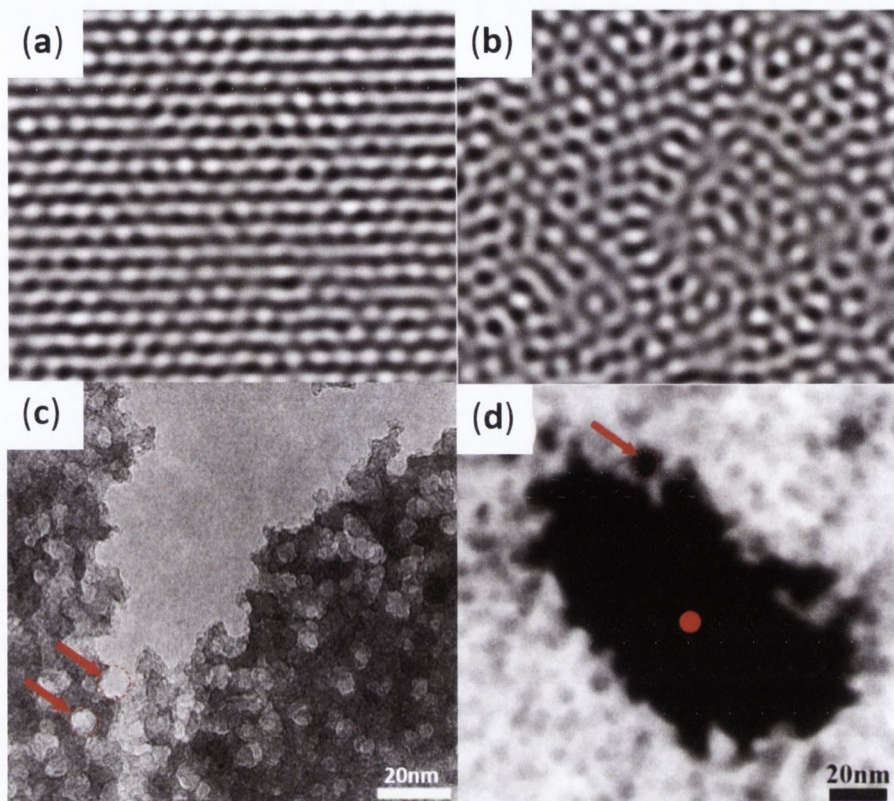


FIGURE 5.8: (a) A focal series reconstruction of pristine multi-layer graphene. (b) A reconstruction of graphene adjacent to an area etched in the SEM. A high pass filter which highlights the high frequency information and removes the ‘foggy’ background has been applied to both of the reconstructed images. (c) Bright-field TEM image of the edge of one of the etched holes, red arrows indicate some pores evident in the material. (d) A plasmon energy loss image with thickness contrast, the red dot at the hole centre shows the nominal diameter of the SEM electron beam used to etch the hole (5.9 ± 0.4 nm).

The nitrogen ions have a limited diffusion length which leads to this increasing thickness further from the hole centre. An area where the material was not etched is soon reached, typically within forty nanometres. An illustration of the etching process is shown in figure 5.9.

It is worth noting that the experimental etching rate is slightly higher than the model predicted at lower beam energies. The lower energy electrons interact far more strongly with the carbon and nitrogen atoms in the system[71]. The high density of nanopores and their connection result in removal of large areas of graphene at an enhanced rate.

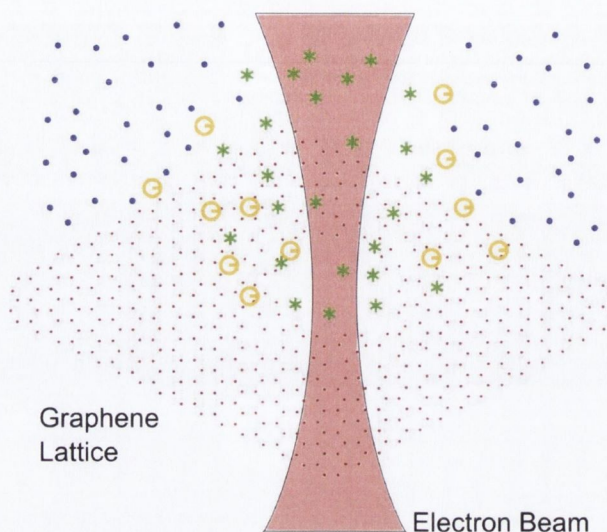


FIGURE 5.9: An illustration of the etching process. The nitrogen gas (blue circles) is ionized (green asterisks) by the electron beam (pink cone at the centre). The nitrogen ions bond with carbon atoms to form a gaseous product (hollow circles) which is then pumped from the system.

5.2.1 Temperature Effect

The energy supplied by the beam to the graphene causes a heating effect which lowers the activation barrier for the etching reaction to occur. It follows that if thermal energy could be supplied by another means the rate of the reaction could be further increased. Similarly if the sample were to be cooled the rate of the reaction would be slowed.

A stage with a controllable temperature range from -25°C to $+50^{\circ}\text{C}$ was used to investigate the effect of temperature on the etching. The beam energy was set to 5 keV, the beam current was 150 pA, the nitrogen gas pressure was 380 mPa and the dwell time was 620 ns.

The stage is water cooled, this leads to more instability than a normal stage. The stage drifted quite significantly, at up to 100 nm/s. This drift rate prevented the use of a single point irradiation as in the previous experiments. Instead an entire flake was irradiated for a total time of 10 min. One flake was irradiated at -25°C , another at $+50^{\circ}\text{C}$. The total area irradiated in each experiment was $1.5 \times 1.5 \mu\text{m}$.

The sample was then analysed using plasmon-filtered TEM. What we expected to observe were nanopores distributed across the surface, like those seen around the edges of figure 5.8(d).

The flake irradiated at -25°C is shown before and after etching in figures 5.10(a) and (b) respectively. The flake irradiated at $+50^{\circ}\text{C}$ is shown before and after etching in figures 5.10(c) and (d) respectively. The before etching images in figures 5.10(a) and (c) are SEM images. The after etching images in figures 5.10(b) and (d) are plasmon energy filtered TEM images. The contrast is not exactly the same in the before and after images due to the different imaging techniques used. What was expected from the etching was damage at the flake edges or pores etched into the surface. These effects were not observed in either case. It is clear from these images that the irradiation caused no observable etching effect.

The lack of etching observed can be attributed to the difference in the dose of electrons delivered to the sample. In a typical etching experiment a point on the sample with an area of $\sim 80\text{ nm}^2$ was irradiated. In this experiment the beam could not be confined to a point on the sample due to the drifting, resulting in an area of $2.25 \times 10^6\text{ nm}^2$ being irradiated by scanning the beam across the sample. Even with the $20\times$ increase in etching time used in this experiment the electron dose was still 1,430 times less than when a single point was irradiated. To deliver a dose which was observed to result in etching in the previous experiments to an area this size (using this beam current, beam energy and gas pressure) an irradiation time of ~ 10 days would be required.

A stage with a greater range of temperature control and more stability (to reduce drifting) would be required to further investigate the effect of temperature on the rate of etching.

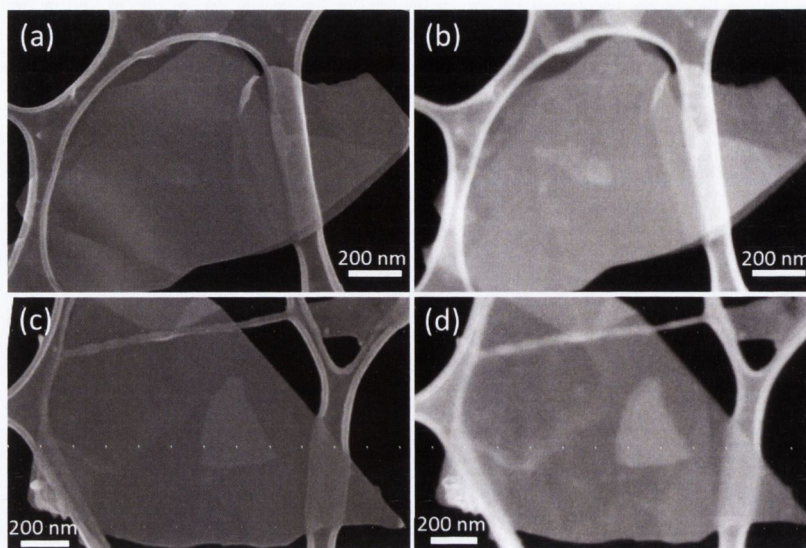


FIGURE 5.10: (a) SEM image of a graphene flake. (b) The same flake imaged in plasmon energy filtered TEM after etching at -25°C . (c) SEM image of a graphene flake. (d) EF-TEM image of the same flake after etching at $+50^{\circ}\text{C}$.

5.2.2 Gas Assisted E-beam Etching of MoS_2

The nitrogen gas assisted electron beam etching technique was developed using graphene. This technique would have a much broader appeal if it could be applied to a range of materials. Etching of a few-layer flake of MoS_2 was attempted.

Figure 5.11 shows a flake of MoS_2 after an attempt at etching. The electron beam was focused on a point within the red box. No observable etching occurred. This result was attributed to two factors. Firstly, MoS_2 layers are three atoms thick, unlike the single atom thick graphene layers. As was observed earlier, the thickness of a sample affects the rate of etching. Secondly, the MoS_2 sample consists of heavy metallic elements which do not react with nitrogen to become a gaseous species which evaporates from the sample. This result indicates that only an etching gas and a sample which react to form a gaseous product are suitable for this etching technique. It must be determined if such a product exists when determining the applicability of this technique to new materials.

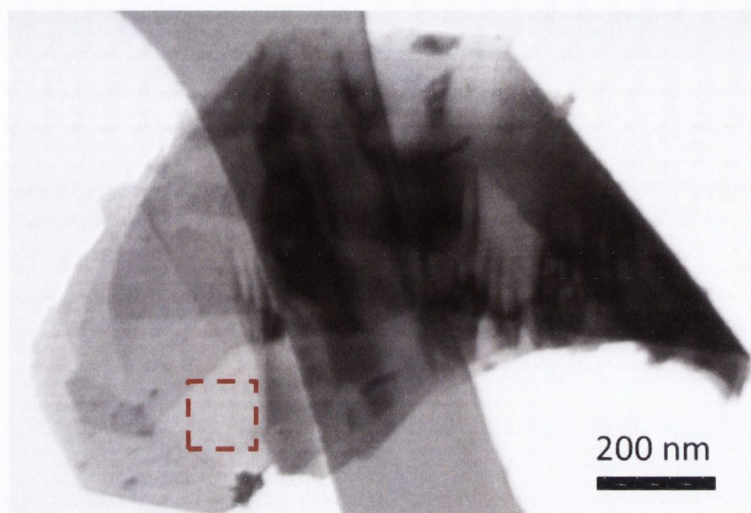


FIGURE 5.11: An MoS₂ flake after etching attempt. No observable etching occurred.

In this chapter a novel technique to controllably fabricate nanopores in graphene with a low energy electron beam has been demonstrated. This method overcomes the limitations suffered by other techniques, providing spatial control of the etching[75]. A model was also developed to describe this etching method. The removal of areas of graphene as observed in the SEM was found to occur due the reaction between the nitrogen ions in the system and the excited graphene lattice, both of which are a direct consequence of the presence of the electron beam. Nanopores with a diameter of < 10 nm were fabricated. A high density of these pores can be fabricated in order to remove larger areas of material.

The experiments conducted here and the model proposed rely on the generation of nitrogen ions, but other gases could also be used. The calculations used to model this process may be applied to a range of materials and gases, as long as they react to form a gaseous product. Further work can be done to afford more control of the etching process, such as adjusting the sample temperature. The modifications made here have been well characterised and can hopefully find applications in gas filtration[3], DNA sequencing[5] or tuning of the carrier density of graphene[56].

The e-beam induced chemical etching process developed here still has some limitations. The etching was localised to the region near the electron beam, however,

the diffusion of ions did reduce the resolution of the process. A precisely defined shape of arbitrary dimensions cannot be etched from the sample. This technique cannot reliably produce a required density of defects within the structure of the material. Also, an appropriate gas must be used such that a reaction with the material to be etched will produce a gaseous product.

In the next chapter the direct sample modification abilities of a beam of helium ions will be investigated. The issue of diffusion of ions from the location of the probe is overcome in this approach. This process can also facilitate the modification of samples without relying on a chemical reaction to occur.

Chapter 6

Graphene Imaging & Modification with a Helium Ion Beam

In the previous chapter the modification of a graphene surface was achieved by the localised reaction of nitrogen ions with the carbon atoms in graphene, enabled by the electron beam. The technique was limited in its resolution and the range of samples to which it can be applied. A very promising technique to overcome such limitations is that of direct sample manipulation by irradiation with a focused beam of high energy (tens of keV) ions.

In this chapter the beam damage, image quality and edge contrast of a graphene sample in the helium ion microscope (HIM) will be investigated. Raman spectroscopy will be used to quantify the disorder that can be introduced into the graphene as a function of helium ion dose. The effects of the dose on both free-standing and supported graphene will be compared. This rate varies due to the interactions which the beam undergoes in the substrate and will be clearly shown and explained. The ability of the HIM to produce GNRs will also be shown.

The irradiation doses investigated by Raman spectroscopy will be correlated directly to image quality by imaging graphene flakes at high magnification. The edge contrast of a freestanding graphene flake imaged in the HIM will then be compared with the contrast of the same flake observed in SEM and STEM.

6.1 Defect Density vs. He^+ Dose

6.1.1 Defects vs. Dose Experiment

For this experiment both freestanding and supported graphene samples were prepared by the Chemical Vapour Deposition (CVD) method. A 1×1 cm copper foil was placed in a furnace and heated to $1,000^\circ\text{C}$ in vacuum. Methane and hydrogen were flowed through the furnace causing carbon to deposit on the copper surface. The furnace was then cooled, leaving a single, continuous layer of graphene on the copper film.

To make the freestanding sample the graphene was transferred to a silicon substrate with arrays of $2\ \mu\text{m}$ holes by the following steps. A 200 nm polymer (PMMA) layer was spin coated onto the sample. The copper foil was chemically etched away. The graphene and polymer layers were transferred to a silicon substrate. The PMMA layer was removed with acetone. Finally, the sample was removed from the acetone and left to dry in air.

Some residual polymer contaminants remain after this process[148]. The extent of the residual contamination on our sample can be seen in the SEM image in figure 6.1. In this image the white areas correspond to the contaminants. The effect of this contamination has been observed to introduce some doping in the graphene[149, 150].

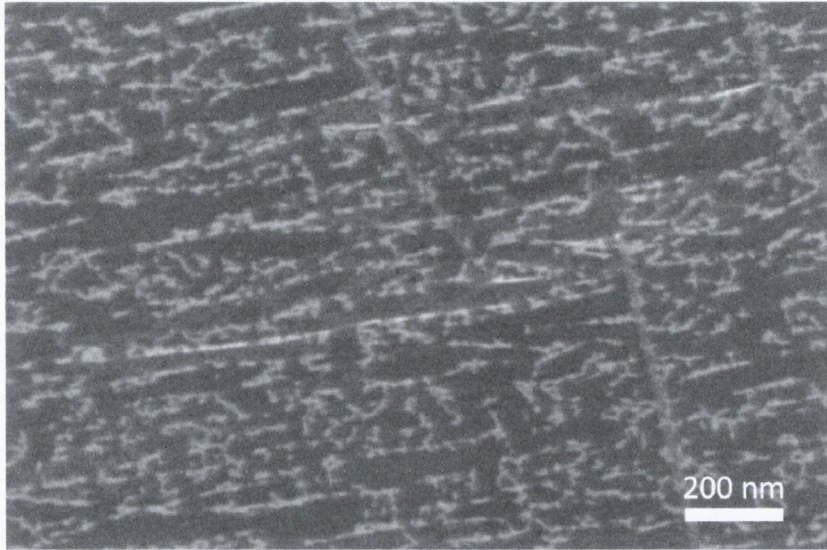


FIGURE 6.1: SEM image of the residual contamination on CVD graphene after transfer to an SiO₂ surface. The contamination appears as the white regions on the sample.

The supported graphene sample was prepared by the same process as above except that the graphene was transferred onto a 300 nm SiO₂ layer grown on a silicon substrate. Single layers were identified by optical contrast.

A HIM operating at an acceleration voltage of 30 kV was used to irradiate both graphene samples. Seven areas on each sample were irradiated with doses of 10^{13} , 5×10^{13} , 10^{14} , 5×10^{14} , 10^{15} , 5×10^{15} and 10^{16} He⁺/cm². This exposure was achieved by using the internal patterning software to raster the focused helium beam over a $2 \times 2 \mu\text{m}$ area with a 5 nm pixel spacing. A beam current of 1 pA was used and the dwell time per pixel was adjusted to achieve the required dose.

Raman spectra were acquired from the irradiated areas using a 10 s acquisition time and four spectrum averages at each point.

6.1.2 Defects vs. Dose Results

Seven Raman spectra from the seven irradiated areas on the freestanding and supported graphene samples were acquired. A spectrum from a nearby un-irradiated

area was also acquired. These spectra are shown for freestanding and supported graphene in figure 6.2(a) and (b) respectively. In order to find the defect density the I_D/I_G ratios for each spectrum were found and are plotted as a function of the log of the irradiation dose in figure 6.3. It is clear from the first four data points in each graph that the supported graphene sample consistently has a greater defect density (higher I_D/I_G ratio) than the freestanding graphene sample, at the same irradiation dose. At a dose above 5×10^{14} He^+/cm^2 the I_D/I_G ratio can no longer be used as an indicator of the defect density in the sample[151]. Above this dose the peaks are observed to become progressively broader. Also the 2D peak is not present in the highest dose samples. At this point the material has become heavily defective.

The supported graphene sample experiences more damage than the freestanding graphene sample for several reasons. We used a SRIM[152] simulation to find the backscatter yield of helium from the sample. Backscattered ions can interact a second time with the graphene layer on the surface. The sample was set up as a 0.34 nm carbon layer on a 300 nm SiO_2 layer on a Si substrate (C density = 2.25 g/cm^3 , SiO_2 density = 2.65 g/cm^3). The trajectories of 10,000 30 keV helium ions in the sample were simulated. The damage calculation mode was set to monolayer collision steps. Figure 6.4 shows the trajectories of the first 500 helium ions in the sample. Very few of the ions were observed to backscatter to the surface of the sample. The yield of backscattered ions from the 10,000 in the simulation was just 0.94 %. This result indicates that a slightly higher dose was received by the supported sample due to backscattering of the primary beam within the substrate. However the backscatter yield is so low that it alone cannot account for the significant difference in damage rate between the two samples that we have observed.

Another factor to consider is the removal of the substrate atoms from the sample by the primary beam; this process is known as sputtering. The sputtered ions can interact with the graphene on their way to the surface. The sputtering yield

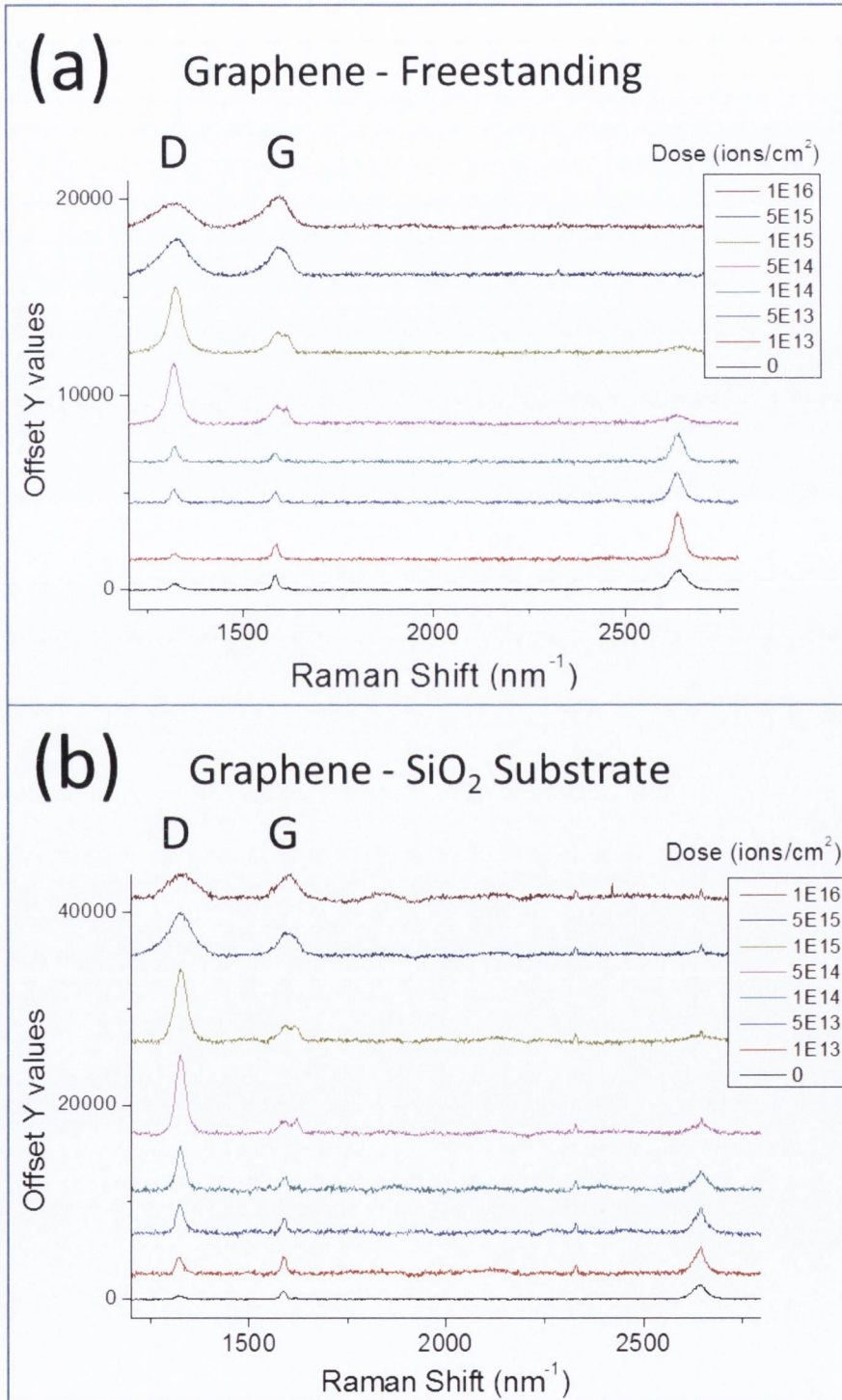


FIGURE 6.2: Raman spectra from graphene areas irradiated with various doses of helium ions. The sample in (a) was freestanding graphene. The sample in (b) was graphene supported on SiO₂.

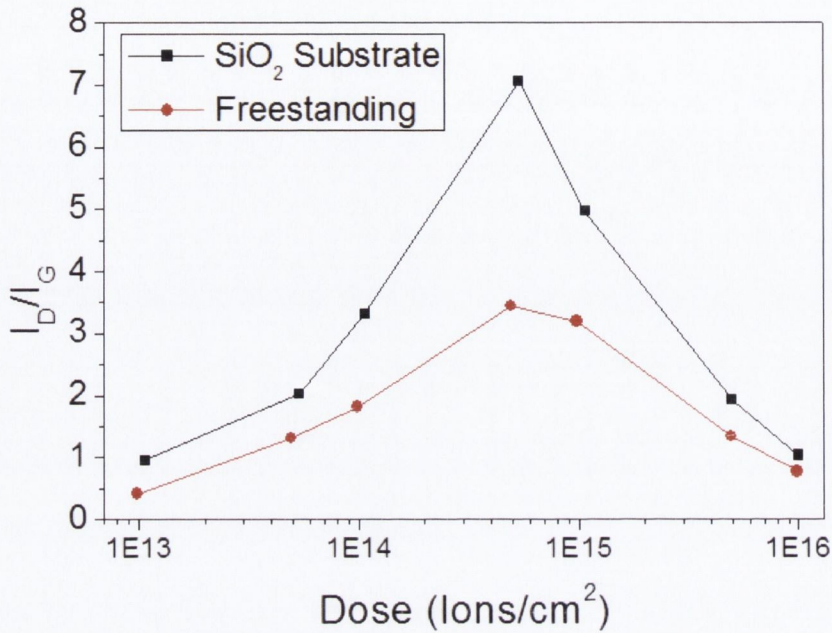


FIGURE 6.3: The ratio of the D peak to G peak intensity of the Raman spectra shown in figure 6.2 plotted against the log of the ion dose. The supported sample was observed to have a higher rate of defect production.

is defined as the number of sputtered atoms divided by the number of incident ions. From the SRIM simulation we know that the sputtering yield for graphene is 0.035. The sputtering yield is 0.003 for Si and 0.005 for O. These sputtered atoms have a very low energy when compared to that of the primary beam. They therefore have a shorter elastic mean free path (MFP) than the primary beam. The sputtered atoms will transfer more energy to the atomic nuclei than to the sample electrons[123]. These various collisions contribute to the enhanced rate of damage in the supported graphene sample over the freestanding sample. The sputtering yield for freestanding graphene is just 0.005.

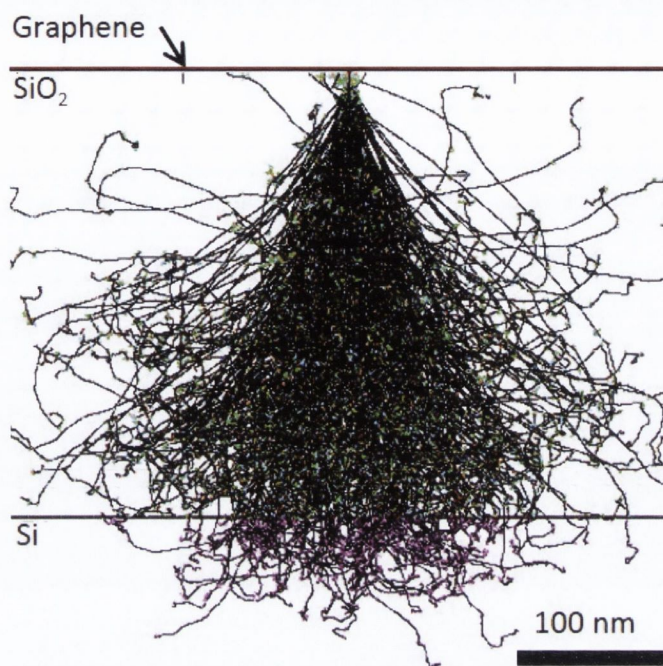


FIGURE 6.4: SRIM simulation of the trajectory of 30 keV helium ions. The sample is single layer graphene on a 300 nm SiO₂ layer on Si. 500 ion trajectories are shown. 10,000 ion trajectories were simulated to obtain a value for the yield of backscattered helium ions. 0.94% of the ions were backscattered. Sputtering yields of 0.035 for C, 0.003 for Si and 0.005 for O were also calculated from the simulation.

6.2 Image Quality vs. He⁺ Dose

6.2.1 Image Quality vs. Dose Experiment

Graphene flakes were prepared by liquid phase exfoliation. A couple of drops of the solution were dropped directly onto a holey carbon support film on a TEM grid and left in air to dry.

In order to correlate the ion doses analysed by Raman spectroscopy with image quality in the HIM a graphene flake was located selected in the HIM. Flakes were used for this part of the project in order to obtain good edge contrast. The graphene flake was suspended above a deep hole (several mm) which acts as a Faraday cup. The bottom of the Faraday cup was coated in carbon. This set-up

produces minimal background noise in the images from secondary electrons and backscattered ions produced beneath the graphene sample.

The flake was imaged with a field of view of 500 nm. This is approximately the minimum magnification at which the sub-nanometre resolution of the tool can still be demonstrated. Higher magnifications would make it impossible to image with the extremely low dose we require. Even at this magnification an image with a dose of 10^{13} He⁺/cm² could not be acquired as our beam blanker could not blank at a fast enough rate to acquire this image with the parameters used. The maximum blanking rate is 100 ns.

Images of the flake were acquired with doses of 5.2×10^{13} , 1.3×10^{14} , 5.2×10^{14} He⁺/cm². These images were acquired with a beam current of 0.4 pA, a field of view of 500 nm and a resolution of 512×512 pixels. The dwell times used were 0.2 μs, 0.5 μs and 2 μs respectively. A final image was acquired with a much higher dose of 1.3×10^{17} He⁺/cm². This is the typical dose used when acquiring a high resolution image from which the sub nanometre probe size of the HIM can be measured. For this image the dwell time was 1 μs the resolution was increased to 2,048 × 2,048 and 32 line averages were used.

6.2.2 Image Quality vs. Dose Results

Four images of a few layer graphene flake acquired with various doses in the HIM are shown in figure 6.5 (a) - (d). Three of these images were acquired with doses very similar to those investigated by Raman spectroscopy (5×10^{13} , 10^{14} , 5×10^{14} He⁺/cm²) and one with a much higher dose of 1.3×10^{17} He⁺/cm². An intensity profile from each image was plotted across the top edge of the flake as indicated in figure 6.5 (a) - (d). These profiles are shown to the right of the image from which they were plotted. In the first half of each profile there is no signal, this indicates that the experimental set up has successfully minimised any signal generation from beneath the sample. As the beam then scans across the sample a signal is

observed. In the lowest dose image (figure 6.5(a)) the signal to noise ratio is very poor and the sample edge is not well defined. The signal to noise is increased as the imaging dose increases, however it is not until a significant dose, on the order of 10^{17} He^+/cm^2 (figure 6.5(d)), that a good signal to noise ratio is achieved. This dose is over 200 times the maximum dose which we have investigated by Raman spectroscopy.

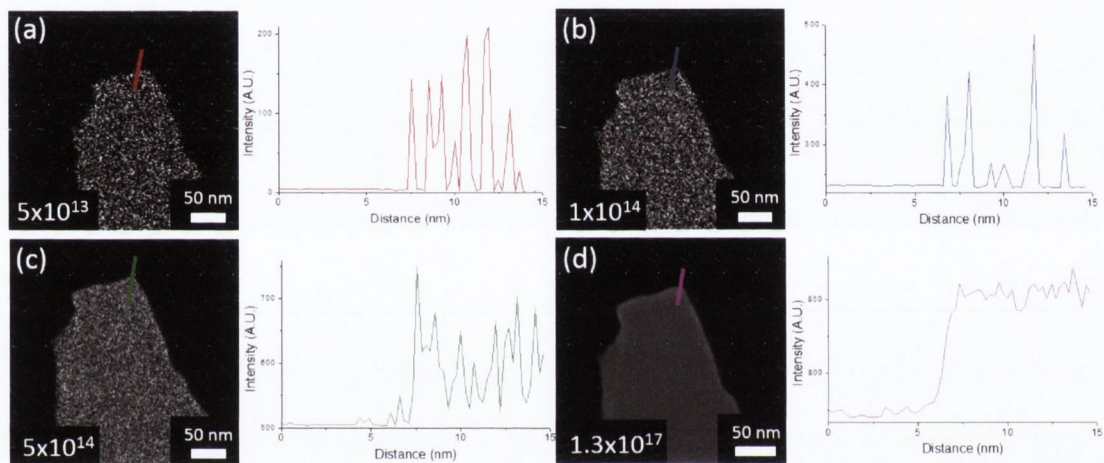


FIGURE 6.5: (a) - (d) Helium ion microscope images of a graphene flake acquired at various imaging doses. The flake is freestanding over a hole in a holey carbon support film. The imaging dose used is indicated on the image in units of He^+/cm^2 . An intensity profile across the edge of the graphene flake was plotted from each image and is shown adjacent. A poor signal to noise ratio was observed until the highest dose of 1.3×10^{17} He^+/cm^2 was used. From the edge profile of the highest dose image the probe size was estimated to be $0.5 \text{ nm} \pm 0.1 \text{ nm}$.

From the intensity profile of the image acquired at the highest dose an accurate edge profile measurement could be made. Taking the distance from 25 % intensity to 75 % intensity across the flake edge gives us a FWHM of our probe of 0.5 ± 0.1 nm. This measurement was done using the ImageJ[118] software package. The signal to noise ratio of the edge profile measurement from the low dose images could be improved by averaging over the width of several pixels. This approach could only be used in the limited case of a perfectly straight edge. Also, the image would still not reveal any other useful information such as surface details.

These results show us that in order to acquire an image of graphene with sub-nanometre resolution in the HIM, a dose which is hundreds of times beyond that which causes serious damage to the graphene lattice is required. Either a high quality sample or a high quality image can be attained, but not both.

6.3 HIM Imaging vs. SEM and STEM

6.3.1 Image Contrast Experiment

A graphene flake was identified on the TEM grid. An image of this flake was acquired in an SEM using the in-lens detector. The microscope was operating at a 20 kV acceleration voltage. A 2.6 mm working distance was used. The same flake was then imaged in a TEM operating at 300 kV. STEM mode was used with a HAADF detector to acquire the image. Finally the flake was imaged in the HIM, which was operating at 30 kV. A very low beam current of 0.4 pA was used in the HIM to minimise sample damage.

6.3.2 Image Contrast Results

When accurate topographical and dimensional analysis is required the HIM provides very useful information when compared to electron microscopes. The three images of a single graphene flake acquired in three different microscopes are shown in figure 6.6. Figure 6.6(a) is the SEM in-lens image, (b) is the STEM – HAADF image, and (c) is the HIM image. The corresponding intensity profiles are plotted adjacent. Each of the imaging techniques displays the graphene flake as a bright region on a dark background.

From the intensity profiles it can be seen that the edges are not always well defined. In the SEM and STEM profiles the edges are somewhat rounded, making it difficult

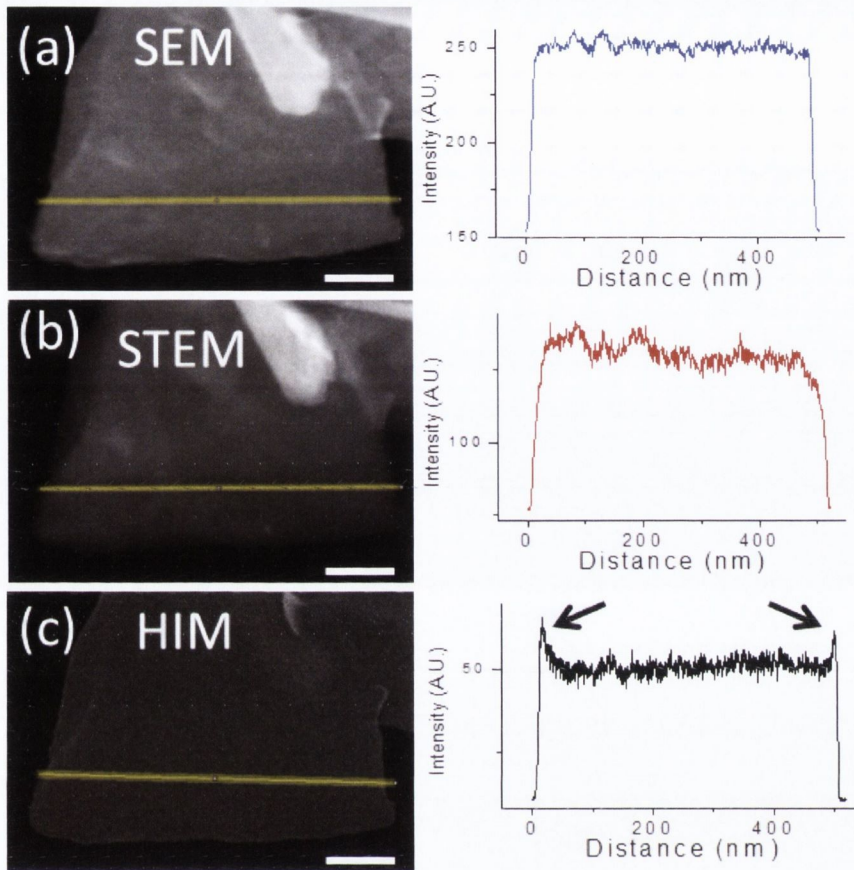


FIGURE 6.6: Three images of the same graphene flake acquired in three different tools. (a) SEM in-lens image of a graphene flake. An intensity profile across the flake is shown adjacent. (b) STEM-HAADF image of the flake. The intensity profile from the same region of the flake is shown adjacent. (c) HIM image of the flake, with the intensity profile from the same region also plotted. The well-defined flake edges in the HIM intensity profile are indicated by two arrows. Scale bars are 100 nm.

to identify the exact edge of the flake. The STEM technique does have the highest resolution and at a larger magnification the edge could be shown with lattice resolution. However, in the HIM profile the edges are bright. This results in a small intensity increase at the edge. This peak makes analysing the dimensions of the flake trivial in the HIM by measuring the peak to peak distance. The well-defined edge contrast in HIM images extends to smaller features than in low kV SEM images[153, 154]. The peak to peak method used here is a simple dimensional metrology technique for measuring nanoscale features, and is only available down to sub-nanometre features in the HIM. This is due to the enhanced sensitivity of

secondary electron yield on incidence angle in the HIM.

6.4 Graphene Nanoribbon Fabrication

6.4.1 GNR Experiment

A thin freestanding flake was located on the TEM grid and four sets of adjacent 15 nm wide rectangles were milled. Each pair of rectangles was milled at a different angle in order to produce GNRs with various edge orientations. A pixel spacing of 0.5 nm and a high dose of He^+ ($>10^{18} \text{ He}^+/\text{cm}^2$) were used.

6.4.2 GNR Results

The GNRs milled by the HIM are shown in figure 6.7. This figure shows that with a sufficient dose the graphene can not only be altered structurally, but can also be completely removed where required. The geometry fabricated here is just one example of how such a material can be altered. Nanopores, or more complex geometries are also possible, with the appropriate beam scan control.

Fabrication of GNRs is not always achieved without issue. The most common problems are shown in the HIM images in figure 6.8. In figure 6.8(a) an array of six adjacent rectangles were patterned. The resulting structure is that of a series of parallel carbon deposits. This is the result of a patterning attempt when the sample or chamber is not sufficiently clean. In this case the rate of deposition is greater than the rate of milling and no ribbons can be produced.

Figure 6.8(b) is an image of a milled cross. Figure 6.8(c) shows the same feature after acquiring a single image. It is clear that the sample is greatly altered by this single image acquisition. This means that acquisition of a high quality image of a milled feature should be avoided in the HIM.

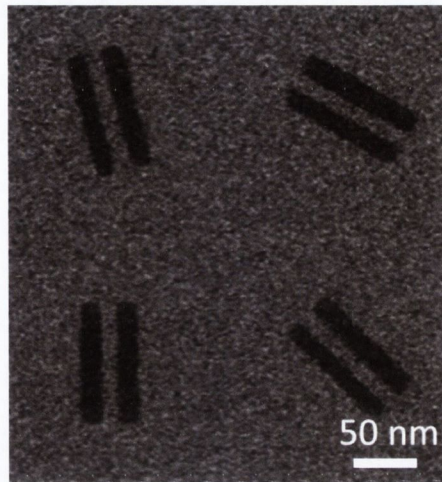


FIGURE 6.7: HIM image of graphene nanoribbons fabricated in the HIM. The eight milled rectangles were used to produce four GNRs with different edge orientations.

Figure 6.8(d) shows an area where six adjacent rectangles were milled across the width of the graphene. The ribbons were milled in series. When milling nearby features one after another the previous area is affected by the fabrication of a new feature. The ribbons bend towards the area being patterned by the beam. This can be avoided by adopting a suitable scanning strategy, as described in section 3.3.2.1.

Figure 6.8(e) is a 15 nm wide GNR. This ribbon remained intact during the fabrication process. However, it was exposed to a substantial dose of helium ions as images were acquired to position the patterns. Its structure has most likely been severely degraded. This could have been avoided by placing the patterns without having looked at the sample, or at least by imaging with a substantially lower dose.

In this chapter CVD grown graphene and Raman spectroscopy were used to determine that a dose of 30 kV helium ions in the range of 10^{13} He^+/cm^2 and below produces minimal damage to graphene. Doses above 5×10^{14} He^+/cm^2 cause significant damage to the graphene lattice. The presence of a substrate beneath the

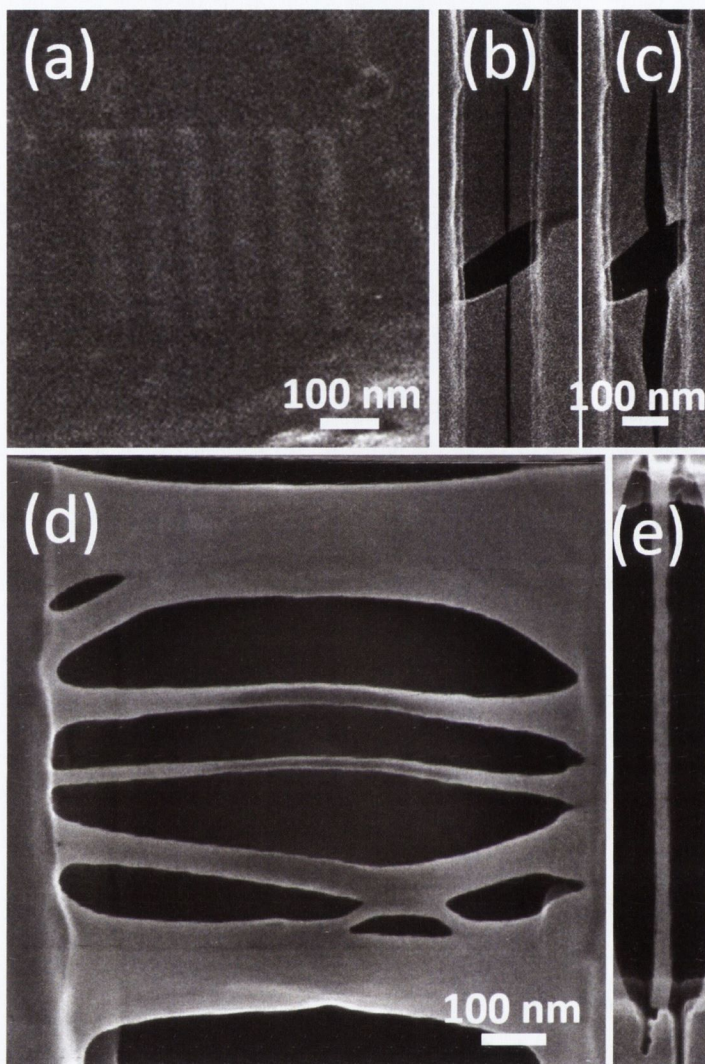


FIGURE 6.8: (a) Attempted HIM milling of six rectangles in graphene. Deposition of carbon contamination was dominant. (b) and (c) The vertical cut milled by HIM (b) was observed to significantly widen (c) by acquiring a single image. (d) HIM milled rectangles which have broadened after imaging. (e) A single 12 nm wide graphene nanoribbon isolated over a trench.

graphene was observed to enhance the rate of damage.

Chemically exfoliated graphene flakes were then used to find the dose required to achieve sub-nanometre (~ 0.5 nm) resolution in the HIM. A dose on the order of 10^{17} He⁺/cm² was required, 200 times greater than the dose which caused significant lattice damage in the Raman spectroscopy. A non-destructive image can be acquired in the HIM, but it must either have a lower signal to noise ratio

or a lower magnification than our high dose image.

HIM images of a single chemically exfoliated graphene flake were then compared with SEM and STEM images of the same flake. The edge of the flake was most clearly defined in the HIM image. Samples with nanometre or even sub-nanometre dimensions, down to single atom thickness, can be simply and accurately measured by helium ion microscopy. The HIM provides highly precise material modification, both in terms of lateral dimensions, desired dose, and even penetration depth into the sample by adjusting the acceleration voltage. This modification has been used here to introduce defects into a graphene sample. The doses identified here serve as a guideline for safely imaging, or controllably modifying graphene in the HIM.

Freestanding graphene was used to produce GNRs 15 nm in width. The ribbons were patterned with various orientations and represent the flexibility of the patterning capabilities of the HIM. There are many issues which need to be overcome for the fabrication to be successful, some of which have been described. The control of the edge structure enables the production of nanoribbons with different properties, such as semi-metallic or semiconducting in the case of graphene.

The damage produced in graphene by HIM irradiation has been characterised and direct patterning was demonstrated. What remains to be investigated is the extent of the lattice damage which is introduced into the structure of the material within the region of a patterned feature. This is of paramount importance as we have established in chapter 2 that a well defined edge structure is required, for example, to produce nanoribbons of graphene with semiconducting behaviour.

In order to characterise the edge structure TEM analysis is required. However, even at the lowest achievable energy of 80 keV in our TEM the knock-on threshold for edge carbon atoms in graphene is still exceeded[155]. A beam energy of ~ 50 keV would be required to minimise the damage. This means that our characterisation technique is not capable of investigating the damage extension from the

edge of a HIM patterned feature in graphene. In the following chapter molybdenum disulfide flakes will be used as they are more stable under the high energy electron beam. Patterns will be milled into these flakes by the helium beam and the resulting lattice structure surrounding the patterned area will be investigated.

Chapter 7

Milling & Refilling of MoS₂ Nanoflakes

In the previous chapter it was shown how defects can be produced in 2D materials by helium ion irradiation. This damage was exploited in order to achieve nanoscale modification. The complete removal of material by helium ion milling was used to fabricate GNRs. Such structures can be used to exploit the effects of quantum confinement.

In this chapter we take the knowledge of the helium ion-sample interaction and use it to mill flakes of MoS₂. It will be shown that patterns of arbitrary dimensions and orientations can be fabricated in MoS₂. The damage extension produced by this technique will also be investigated.

Furthermore, the process of introducing carbon into a milled region by beam induced deposition will be demonstrated. Unique heterostructures and heterojunctions can be created by this technique. The carbon can subsequently be annealed *in situ* by the electron beam in the TEM.

7.1 Helium Ion Milling

7.1.1 Milling Dose Calculation

The dose of helium ions required to mill a region from a single layer of MoS₂ must be calculated in order to fabricate nanostructures. A lower dose would only lead to structural damage, not complete removal of material. First equation 3.10 can be used to find the displacement cross sections of both the molybdenum and sulphur atoms in the MoS₂ sample. Their relative contributions were added with a weighting which depends on the atomic ratio of the two atomic species, i.e.

$$\sigma_{d, MoS_2} = \left(\frac{2}{3} \times \sigma_{d, S} \right) + \left(\frac{2}{3} \times \sigma_{d, Mo} \right) \quad (7.1)$$

The displacement energy, T_D , of a sulphur atom in MoS₂ is 6.9 eV[20]. This value was found using DFT simulations and may vary somewhat from the actual value. The maximum transferable energy, T_m , from a helium ion with a kinetic energy of 30 keV to a sulphur atom can be found using equation 3.1, reproduced below:

$$T_m = \frac{4M_1M_2}{(M_1 + M_2)^2} E$$

For sulphur $M = 32.06$ and $Z = 16$. T_m for sulphur was found to be 11.83 keV. The equation for the displacement cross-section, σ_d , was first given in equation 3.10, it is:

$$\sigma_d(E) = \pi \frac{M_1}{M_2} Z_1^2 Z_2^2 e^4 \frac{1}{E} \left(\frac{1}{T_D} - \frac{1}{T_m} \right)$$

For sulphur this becomes $\sigma_{d, S} = 4.977 \times 10^{-37} \text{cm}^2$.

For molybdenum $M = 95.94$, $Z = 42$, $T_m = 4,613$ eV and $T_D = 20$ eV[20]. The displacement cross-section for molybdenum is $\sigma_{d, Mo} = 3.939 \times 10^{-37} \text{cm}^2$.

The total displacement cross section using equation 7.1 is $4.626 \times 10^{-37} \text{cm}^2$. Next the areal density of atoms, Nx , in a layer of MoS₂ must be calculated. The

equation used was

$$Nx = \frac{M}{\rho} N_A x \quad (7.2)$$

where M is the molar mass, ρ is the density and N_A is Avogadro's number. Using values of 160.07 g/mol for M , 5.060 g/cm³ for ρ , 6.022×10^{23} mol⁻¹ for N_A and 6.2×10^{-8} cm for x (the thickness of a single layer of MoS₂[156]), this becomes $Nx = 1.181 \times 10^{18}$ cm⁻². The probability of a displacement collision occurring is,

$$P = \sigma_d Nx,$$

$$P = 5.463 \times 10^{-19}$$

This is the probability of one helium ion removing one cm² of single layer MoS₂. When a dose of $(5.463 \times 10^{-19})^{-1}$ He⁺/cm² is used there is a 100% probability of removing one cm² of single layer MoS₂. In order to remove one cm² of MoS₂ a dose of 1.830×10^{18} He⁺/cm² is required.

The main simplification made in this calculation is that the cross-section, and thus the probability, does not vary during the irradiation process. In reality the partial removal of the MoS₂ structure will lead to a reduction in the displacement energy of the Mo and S atoms. This will lead to a somewhat reduced dose being required to remove a single layer. The value we have calculated is the upper limit of the milling dose for single layer MoS₂.

Another simplification which was made was that there is no difference between scanning the beam slowly over an area in a single pass, or scanning the beam rapidly over the sample in several passes. As long as the total dose received by the sample is the same the result is the same. It is known from many years of FIB experiments that this is not the case[157]. Our approach is to scan the beam over the sample in one pass. If several passes were used the beam would experience a modified sample with each pass; this is a more complex situation which we avoided.

7.1.2 Ion Milling Experiment

MoS₂ flakes were prepared by chemical exfoliation. The MoS₂ solution was dropped directly onto a TEM grid. The grid was left to dry in air overnight. The sample was then baked at ~ 80 °C for 3 hrs. The TEM grid was loaded into an SEM stub designed to hold TEM grids. The surface beneath the TEM grid (several mm below) was a non-conductive carbon layer. The carbon layer has a very low SE yield due to the charging effect; the positively charged surface inhibits the escape of negative SEs. The yield of backscattered ions is also very low for carbon (< 0.2 %). This ensures that the SE contrast between the flake and the surrounding hole is maximised. It also ensures that the milling is done by the primary ion beam, and not the less localised backscattered ions, resulting in the highest milling resolution.

An appropriate MoS₂ flake was selected in the HIM. On selecting a flake three criteria were assessed. The flake must be thin. It must be suspended over a hole in the carbon support film. Finally, it must have well defined edges. The edges typically align with either zigzag or armchair structure; this indicator can be used to cut along low order crystal directions.

The helium ion beam current was set to 0.5 pA. The probe size was measured before all experiments and was consistently 0.5 nm or less. The beam was scanned across the surface of the MoS₂ flake with a step size of 0.5 nm. The beam dwell time at each point was set to 1 ms in order to deliver a total dose of 1.3×10^{18} He⁺/cm² to the desired area. An area of 10×100 nm required ~ 5 s to mill.

TEM images of the milled areas, both bright-field TEM, as well HAADF-STEM, were acquired. The TEM was operated at 300 kV throughout the experiment.

7.1.3 Results and Analysis of Ion Milling

A single MoS₂ flake can be seen at the centre of figure 7.1(a). This is a HIM image. It was acquired at a low dose, as found in chapter 6, to minimise beam damage. From this image a pattern of two adjacent rectangles was aligned on the flake and milled. The dose of 1.3×10^{18} He⁺/cm² used here was found to be the lowest dose which could be used to remove a layer of MoS₂. The patterned flake was shown in the TEM image in figure 7.1(b). This value is very close to the calculated value of 1.83×10^{18} . This supports the results of the theoretical calculation of the MoS₂ milling dose. The assumption that the experimental dose would be lower than the calculated dose due to the simplifications of the model was also confirmed.

Figures 7.1(c) and (d) are HAADF-STEM images of the HIM milled rectangles. In figure 7.1(c) The brighter area on the right is thicker, where two flakes overlap. The milling in this area has not completed as the fabricated structure is not as wide as it is on the left. This is evidence of the thickness dependence on the milling. A higher dose is required to remove the thicker area. Figure 7.1(d) shows the structure along the milled edge of the flake. The edge shows a predominantly zigzag termination with no observable damage to the lattice structure. A model of the hexagonal lattice is overlaid on the image, while the edge structure can be clearly seen in the inset image.

Figure 7.2(a) shows the flexibility of the milling technique in its ability to fabricate structures with arbitrary orientations. These two rectangles were milled with a 60° rotation relative to each other. This allows features with zigzag or armchair edges, or a more complex combination of the two, to be produced. One such complex edge is shown in figure 7.2(b). The edge can be seen to remain intact and crystalline.

Figure 7.2(c) shows a nanoribbon of MoS₂ which was isolated on both sides by milling with helium ions. The ribbon is just 7 nm in width. Partial amorphisation

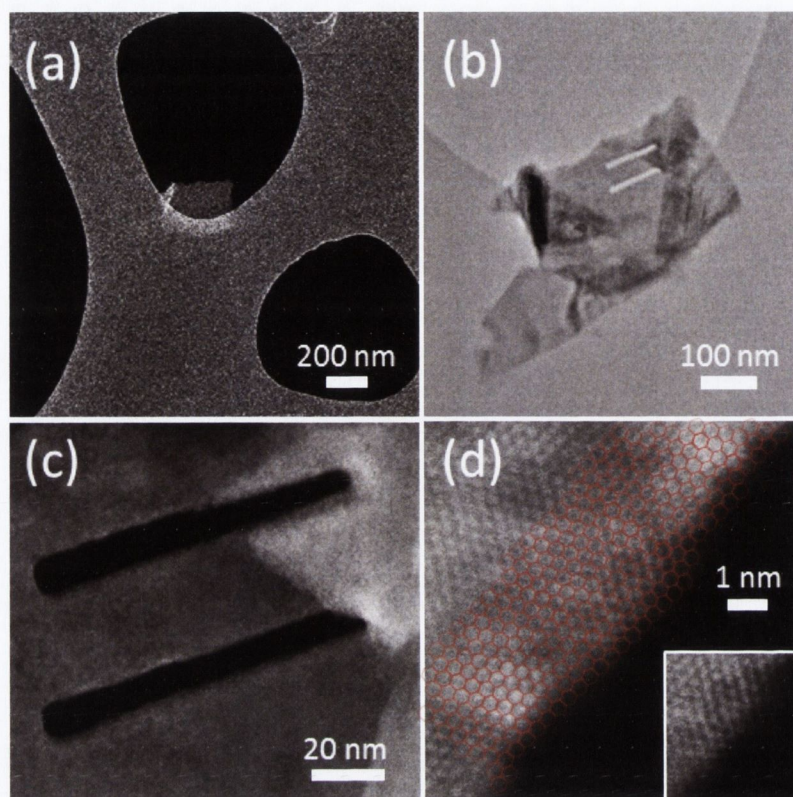


FIGURE 7.1: (a) An image of an MoS₂ flake suspended on a carbon support film acquired in the HIM. (b) The same flake imaged in TEM after helium ion milling. (c) HAADF-STEM of the two milled slots in the flake. (d) High Resolution HAADF-STEM of the configuration of the milled edge. It is predominantly zigzag structure.

was observed on the left side of the ribbon. The cause of this damage could be some exposure to helium ions, or perhaps strain was introduced during its isolation. A build up of contamination may also have occurred. Further studies will need to be undertaken in order to fully understand and perfect the milling technique.

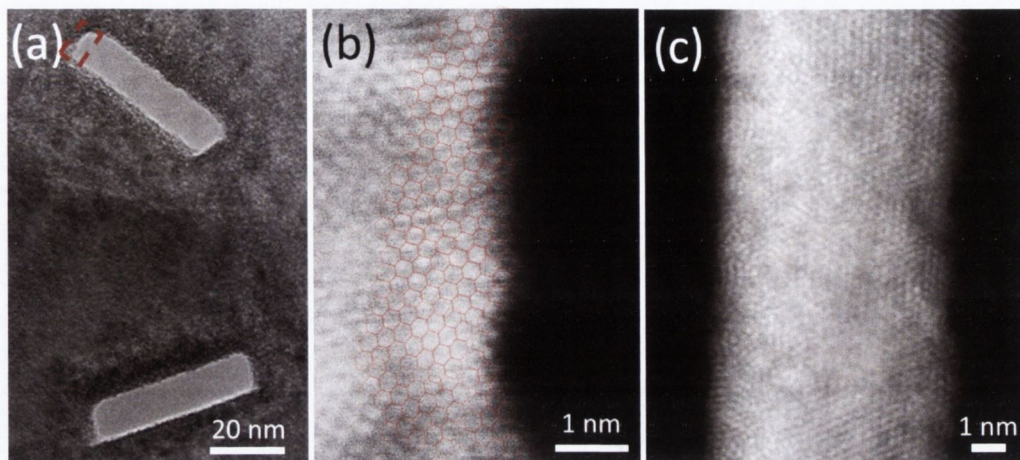


FIGURE 7.2: (a) TEM image of two HIM milled rectangles with a 60° rotation relative to each other. (b) The combined zigzag/armchair structure of an edge not cut along a high symmetry direction. Acquired at the region indicated in (a). (c) A 7 nm wide MoS₂ nanoribbon.

7.1.4 Outstanding Issues

Contamination is an issue which requires careful control. The environment within the TEM can be well controlled¹, however the sample storage conditions also require consideration. Figure 7.3(a) is an image of a hole milled within an MoS₂ flake by the HIM. After the milling process the sample was left in air for ~3 months. Over this time contaminants within the atmosphere had begun to fill the hole.

The hole in figure 7.3(a) is an example of a relatively large hole at $55 \times 35 \text{ nm}^2$. A pattern with smaller dimensions would be filled with contamination more quickly, perhaps even within days. This prevents the imaging of the edge structure of HIM milled features. The sample must be stored in an evacuated environment, such as a desiccator, to minimise this issue. Even more troubling is the long term viability of devices with such features. A method of isolating or passivating the milled structures may be required.

Figure 7.3(b) is an example of the deviation of the shape of the final milled feature

¹The chamber pressure in the TEM is typically on the order of 10^{-5} Pa

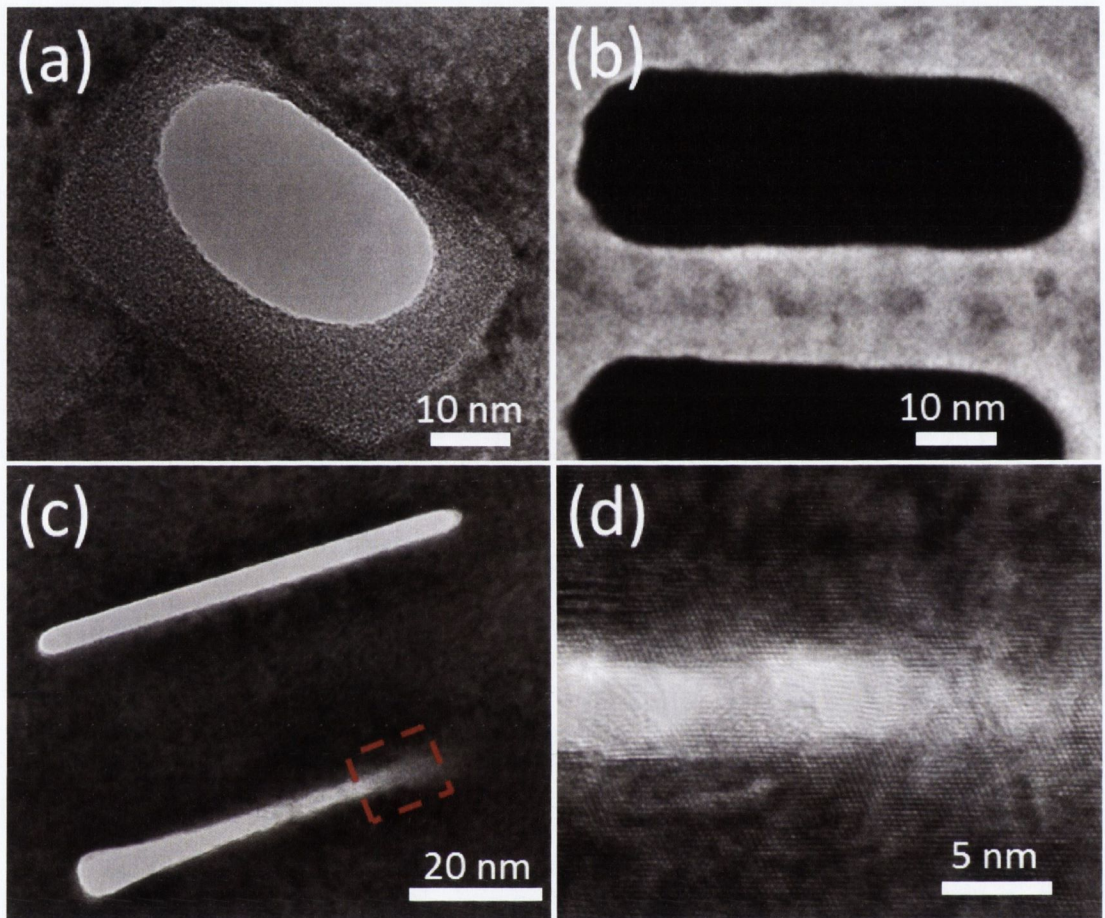


FIGURE 7.3: (a) Atmospheric contamination partially filling a HIM milled hole in MoS₂. (b) Rounding of the corners of a shape which was defined to be a rectangle was observed. (c) Different scanning strategies provide different results. Top: beam scans along length, bottom: beam scans perpendicular to length. (d) Partial removal of MoS₂ layers from the area highlighted in (c); an exfoliation process was observed.

from the input pattern. The black holes in this image were programmed to be rectangles, however the corners have a rounded shape. Whether this is related to some preferential milling direction in the MoS₂ crystal will require further experiments to investigate.

A simplification of the milling model described earlier in this chapter was that the beam scanning strategy was not accounted for. In figure 7.3(c) we see a clear example of how the beam control is an important factor in the milling process. Both of the rectangles were milled with the same dose. Both rectangles were

even milled in a single pass of the beam. The only difference was that in the top rectangle the beam scanned line by line along the length of the rectangle whereas in the bottom rectangle it was scanned perpendicular to the rectangle length. In the bottom rectangle the beam started on the right side and moved line by line towards its finishing point on the left. In this case the top rectangle appears to have been milled more efficiently. In the lower rectangle the beam did not fully penetrate the flake until almost half way along the pattern. This effect is most pronounced in thicker samples, i.e. more than three layers for MoS₂.

Figure 7.3(d) is a higher magnification of the region highlighted in 7.3(c). At this stage of the patterning the beam had yet to fully penetrate the sample. What was observed was partial removal of the MoS₂ layers. This regime of the milling can be considered a ‘beam exfoliation’ process. It can be seen that although strain and damage are introduced into the remaining layers, the crystal structure remains largely intact. Optimisation of this process could yield another application for the processing of nanomaterials with a beam of helium ions.

7.2 E-beam Annealing

After removing a region from an MoS₂ flake, that area can be filled with another material. The goal in this section is to describe the process of filling this hole and then annealing the structure of this new material using the energy supplied by electron beam irradiation.

7.2.1 Annealing Dose

In order to illuminate a well defined area of the sample during the annealing process the smallest available selected area aperture was inserted into a conjugate image plane. The beam current which flows through this area can be recorded.

The area and the beam current can be used to find the total electron dose to which the region was exposed. It should be noted that this aperture is in a plane which is below the sample. The aperture therefore does not physically limit the electron irradiation to the area measured, it simply allows an area through which a known beam current flows to be defined.

The selected area aperture used in our experiment defined an area with a radius of 64 nm on the sample, as measured by the CCD. A beam current of 25.8 nA was found to irradiate this area with the typical condenser lens settings. This is equal to 1.61×10^{11} e/s. The area through which this current flows, as defined by the selected area aperture, is $(\pi)(6.4 \times 10^{-8})^2 = 12,868 \text{ nm}^2$. This gives a dose rate of $1.25 \times 10^7 \text{ e.nm}^{-2}.\text{s}^{-1}$.

In our experiment a time of 2,490 s (41.5 min) was used, resulting in a total dose of 3.1×10^{10} e/nm². This is comparable to the dose of 10^{10} electrons/nm² used by Börrnert *et al.*[158] to anneal a thin carbon layer in a TEM. Our sample may have required a higher dose due to an increased thickness of the carbon layer in our sample. It was decided that this annealing time was reasonable so the beam current was left at 25.8 nA. The process could be accelerated by increasing the current.

7.2.2 Annealing Experiment

The *in situ* filling material used was carbon. Carbon can be produced by the beam induced decomposition of hydrocarbon material. It was found that a build up of carbon could be avoided during typical TEM imaging sessions. However, when carbon is required, as in our case, there are some approaches to enhance the deposition rate. Firstly, by imaging the sample when the cold-trap is warm. Secondly, shortly (a few mins) after loading the sample the vacuum has yet to fully recover from the sample loading process and more contaminants exist within the chamber.

An MoS₂ flake with a hole milled by the HIM was located in the TEM. The flake was left in the field of view under parallel illumination at 300 kV for 10 min. The hole was observed to fill completely during this time. An EDX map² was acquired to confirm the presence of carbon in the HIM milled hole.

The acceleration voltage was then switched to 80 kV for the annealing of the carbon. This was necessary in order to minimise the removal of carbon atoms from the newly filled region due to knock-on damage. A bright field TEM image was acquired at 80 kV after the annealing process in order to observe the modified structure of the carbon filled region. Further imaging or analysis at 300 kV was avoided to minimise damage to the newly-formed carbon structure.

7.2.3 Results and Analysis of Annealing

Figure 7.4(a) is a HAADF-STEM image of an MoS₂ flake with three separate rectangles milled in the HIM. The rectangle on the right hand side (outlined) was selected for the annealing experiment. Figure 7.4(b) is a bright field image which was acquired when conditions were optimal for deposition of contamination. The carbon was filled into the hole at the start of the experiment. Figure 7.4(b) shows the amorphous structure of this material before the annealing process.

EDX maps describing the distribution of Mo, S and C in the region of the hole are shown in figures 7.4(c), (d) and (e) respectively. These maps confirm that carbon is indeed the element present in the HIM fabricated hole within the MoS₂ flake.

The final image, shown in figure 7.4(f), was acquired at the same region as figure 7.4(b). After the annealing process it can clearly be seen that a change in the structure of the carbon occurred. Partial graphitization of the carbon was observed. With further optimisation the degree of crystallisation could most likely be improved.

²An acquisition time of 3 s per point was used to achieve a reasonable signal.

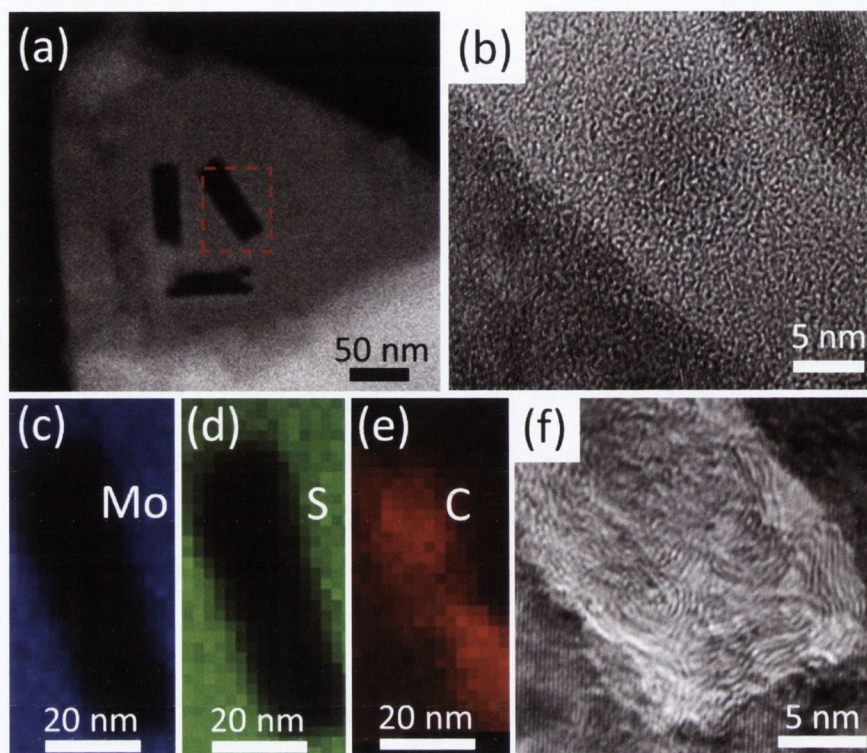


FIGURE 7.4: (a) An image of an MoS₂ flake acquired in HAADF-STEM mode. (b) The area highlighted in (a) after beam-induced filling with amorphous carbon. (c) – (e) EDX maps of the molybdenum, sulphur and carbon distributions around hole highlighted in (a). (f) HR-TEM image of the carbon structure after annealing.

It is worth noting that the structure of the carbon appears to follow the edge of the MoS₂ flake. This is particularly evident in the right hand corner of figure 7.4(f). The aligning, or relative misaligning, of the carbon and MoS₂ structures could be used to tailor the properties of the heterojunction.

The fabrication of nanostructures within 2D flakes of MoS₂ was demonstrated in this chapter. Edges terminated with a zigzag or more complex structure were shown. Ribbons of material with widths of 7 nm were also shown. This process can easily be applied to any of the family of the 2D materials, we have demonstrated this technique on graphene also. The analysis of the edge structure of graphene requires low voltage TEM with spherical aberration correction. This is required

to avoid edge damage and also to resolve single atoms at the edge.

Another issue is that of contamination. As outlined in this chapter contamination can either be avoided or exploited by careful consideration of the sample environment. In this case contamination was used to deposit a carbon layer into a nanostructured MoS₂ flake. The contamination was then annealed and imaged, all in the same session. The annealing was observed to change the structure of the carbon within the MoS₂ flake. This resulted in a unique heterostructure which can be tuned in order to modify its properties.

Further work could even be done to introduce different materials into these structures. Ultimately a broad range of materials systems, with more complex geometries, could be produced by this method. In the next chapter the modification capabilities of HIM irradiation will be extended to a 3D sample.

Chapter 8

3D Sample Modification With Focused Ion Beams

In the previous chapter the removal of material from MoS₂ flakes with nanoscale precision was demonstrated. The helium ion beam used introduces minimal damage to the structure of the material within the direct vicinity of the modification. In this chapter He⁺ beam modification will be extended to 3D samples. It will also be compared to 3D sample modification with the conventional Ga⁺ FIB. Applications of this technique will be described.

Generally speaking, energetic ions, both broad and focused beams, are widely used to modify the physical and chemical properties of the surface of materials with a high degree of control. They can be used to modify and control a material's optical[159], electrical[160], magnetic[161] and mechanical[162] properties. In particular, the gallium ion beam of a FIB microscope has been used for applications in a range of fields including biology[163], geology[164], materials science[165, 166] and the semiconductor industry[167], where micro/nano scale modification is demanded.

One common use of the FIB is in the preparation of thin sections of material, or lamellas, for TEM analysis. This can be achieved by the lift-out technique (the

conventional cross section lift-out is described in appendix C). In the first part of this chapter a new lift-out approach, the extraction of a plan view lamella by the Ga^+ FIB, will be described. The added information obtained by this lamella will be made evident by comparison with a cross section lamella from the same sample.

While the FIB has been adopted for many uses it is not without its limitations. The FIB uses gallium, a metallic element which is often considered a contaminant. The large momentum of the gallium ions in the FIB can have a very destructive effect on materials, greatly altering their crystal structure. The probe size of the FIB is limited by the energy spread of the gallium ions generated from the Liquid Metal Ion Source (LMIS). The sputter yield is also too large for acute patterning control over very short lateral distances. The probe of helium ions used in the helium ion microscope can be used to overcome these limitations. Helium ions have a lower mass and are therefore less destructive than gallium ions, they also do not contaminate the sample surface with metal ions.

In the second part of this chapter the interaction of a helium ion beam within a 3D sample will be studied. The HIM will be used to modify a Si lamella. Silicon was used as it is a well characterised material and is of fundamental importance to the semiconductor industry. We intend to develop a HIM based lamella polishing technique for high quality TEM characterisation.

The trajectory of the helium ions and their effect on the structure of the silicon sample will be studied. A range of techniques such as EDX, EFTEM and EELS will be used to characterise the sample modification process. The limitations of this technique will also be discussed.

8.1 FIB Preparation of TEM Lamellae

In this section the plan view FIB *in situ* lift-out technique will be demonstrated on a system consisting of Ag and Co nanoparticle arrays previously deposited on an optically transparent substrate (Al_2O_3)[168].

The sample was prepared as described in references [169–171]. The SEM image in figure 8.1 shows the surface morphology of the sample. The individual particles can be seen but their composition cannot be identified. Further analysis in TEM was required to determine the distribution of the two different materials on the sample. In order to protect the sample surface before FIB milling a thin gold coating would usually be sputtered on to the surface of the sample. However, the similar atomic masses of the gold coating and the deposited silver would lead to poor image contrast. Instead the surface was protected by coating the sample with a 75 nm layer of carbon using a Cressington 108 carbon/A carbon coater. A 5 nm layer of gold was deposited on top of the carbon layer in a Cressington 108 auto sputter coater.

A cross-section lamella was first extracted from the sample, as outlined in appendix C. This is the typical viewing direction afforded by a FIB lift-out. A cross-section view is perpendicular to the plan view shown in figure 8.1.

8.1.1 Plan View Lift-Out

During the FIB fabrication the sample needs to be tilted relative to the electron and Ga^+ beams. The sample was brought to the eucentric height, at which the tilt plane is on the sample surface, tilting therefore doesn't cause the sample to shift laterally. A 5 mm working distance was used. The electron and ion beams were aligned to co-incidence on the sample surface. A protective platinum layer was deposited on a larger area (compared to the cross-section procedure) of 5×9

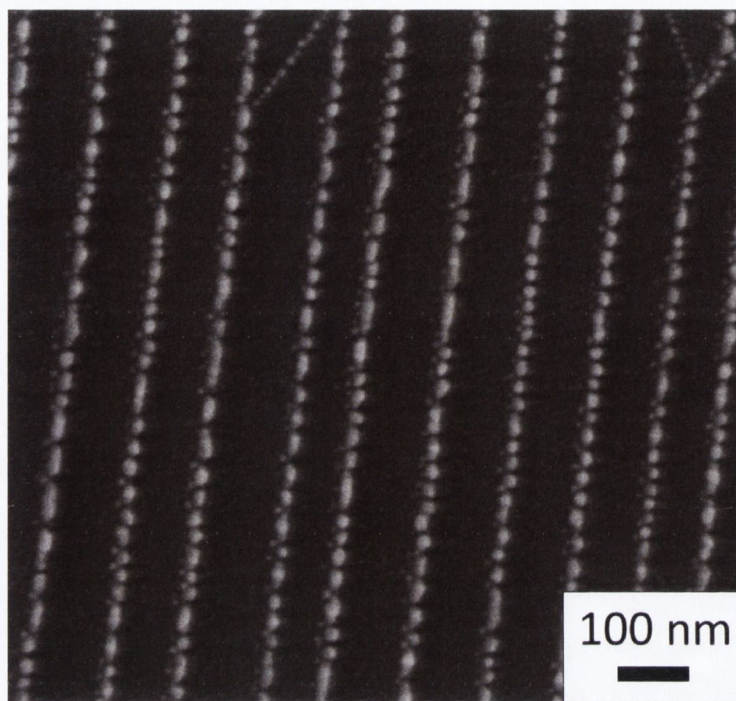


FIGURE 8.1: SEM image of the cobalt and silver nanoparticles deposited on a stepped sapphire substrate.

mm to protect the surface area for TEM analysis. 100 nm was first deposited by the e-beam, a further 1 μm was deposited by the Ga^+ beam.

An illustration of the milling geometry adopted in the next steps is shown in figure 8.2(a). A trench was milled either side of the protected region. Critically the ion beam was at 52° to the surface normal, as opposed to 0° in the cross-section technique, in order to cut under the region. The beam current used was 10 nA and the milling time allowed for each trench was 15 min. The sample was then tilted 15° such that the ion beam was at 67° to the surface normal. A 10 nA beam was used to mill each side of the protected region for a further 5 min in order to ensure the sample was fully under cut. The sample was eventually milled to the wedge shape shown in figure 8.2(b). One final trench was milled with a 10 nA beam for 10 min to free one side of the sample from the substrate, and also to verify undercutting had completed successfully.

A micromanipulator needle was brought in to contact with the free side of the

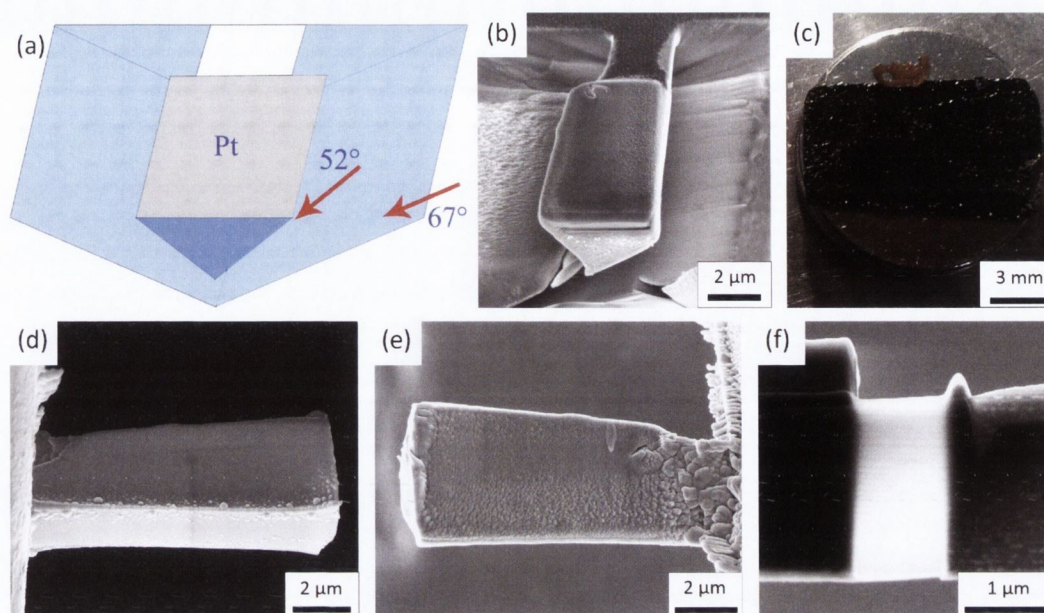


FIGURE 8.2: (a) Illustration of the ion beam angles used to undercut a wedge of material from the sample surface. (b) The wedge of material (coated with platinum) after undercutting. (c) Omniprobe TEM lift-out grid mounted horizontally on carbon tape on an SEM stub. (d) The bottom of the wedge of material after lift-out and transfer to the TEM grid. (e) The top of the wedge, the opposite side to (d). (f) The final lamella with a region thinned for TEM analysis.

sample and fixed with platinum, the sample was then cut free from the substrate. This time the sample was transferred to an Omniprobe TEM lift-out grid which was mounted horizontally on the sample holder. This was achieved by over hanging the grid over the edge of carbon tape, as shown in figure 8.2(c). The sample was affixed to the grid with platinum and the micro-manipulator needle was cut free. The grid was then unloaded from the microscope and mounted in the usual vertical position as shown in figure C.1(c).

The sample was thinned on the side with the wedge shape (the side observed in figure 8.2(d)) with a 200 pA ion beam in order to make the front and rear sides of the lamella parallel. A 20 pA beam was used to further thin this side until the nanoparticles could be observed with the electron beam. The rear side of the sample (observed in figure 8.2(e)) was thinned with a 20 pA beam until the sample was observed to be electron transparent at an electron beam energy of 5 keV, an

indication that the sample is thin enough for TEM analysis. Finally a 5 keV ion beam energy at a beam current of 20 pA was used to reduce the FIB induced damage on the sample. The finished sample is shown in figure 8.2(f). The sample was plasma cleaned for 3 min before insertion into the TEM.

8.1.2 Cross Section vs. Plan View Results

An overview of the cross section TEM lamella is shown in figure 8.3(a). In the TEM analysis of the sample prepared in cross section view the location of the nanoparticles can be clearly identified, as seen in the HAADF image in figure 8.3(b). The nanoparticles have high contrast with the surrounding carbon which we deposited on the sample. The Al_2O_3 substrate was tilted on to the [210] zone axis (see inset in figure 8.3(a)) before imaging. A high magnification bright field TEM image of a particle on the substrate step is shown in figure 8.3(c).

One of the problems TEM was required to solve is the distribution of the cobalt and silver on the sample. EDX mapping was used to analyse the distribution of the concentrations of each element. A pseudo coloured elemental colour map was generated to illustrate the results, shown in figure 8.3(d) (top right). From this map the cobalt and silver appeared to have come together to form a composite particle. There was very little separation between the locations of cobalt and silver in this viewing direction, suggesting close proximity between the two materials deposited on the steps of the substrate. Critically, in this viewing direction the sample orientation is such that a projection of approximately 2 to 3 nanoparticles was observed; information about an individual nanoparticle cannot be obtained from this sample.

When imaged in plan view, rows of individual nanoparticles were observed (see figure 8.4) and the number of particles observable was greatly increased over the cross section view, thus allowing for much greater sampling using a single lamella. The contrast between the particles and the surrounding material is high as shown

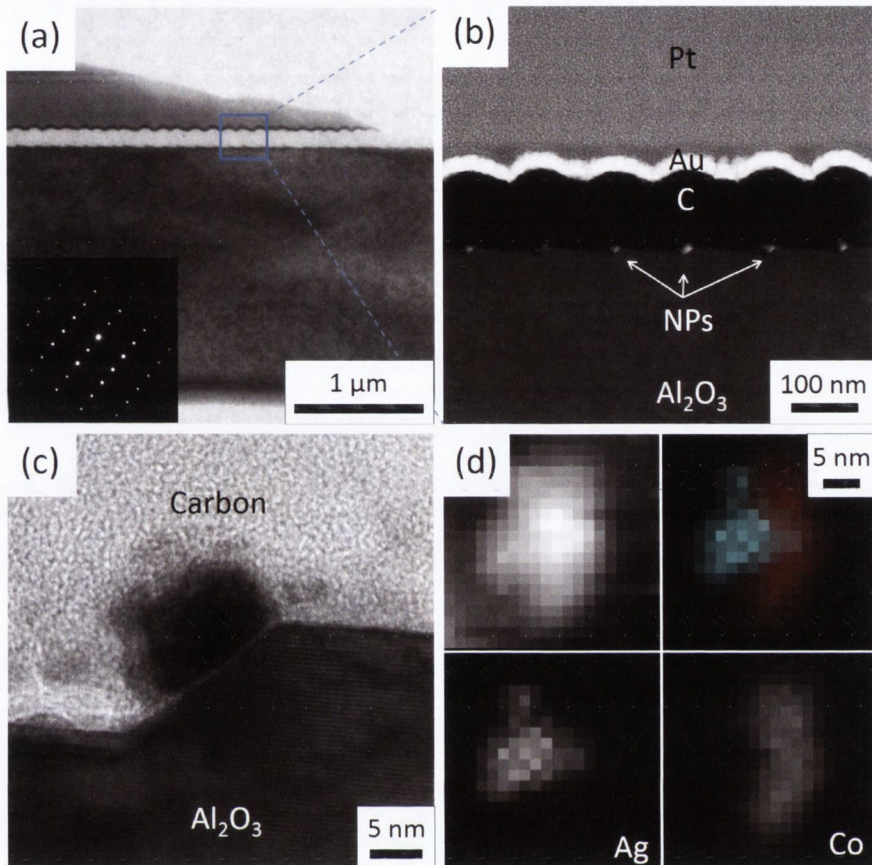


FIGURE 8.3: (a) Bright field TEM image of an overview of the cross section lamella, inset is the diffraction pattern from the substrate showing a [210] zone axis. (b) HAADF image of the region indicated in (a). The nanoparticles (NPs) are observed at the steps of the substrate. (c) High magnification image of a nanoparticle on a sapphire step. (d) Top left: HAADF image of a nanoparticle. Top right: Elemental colour map of the distribution of silver (cyan) and cobalt (red). Bottom left and bottom right: individual maps of the silver and cobalt locations, respectively.

in the bright field TEM image in figure 8.4(a) and the HAADF image in figure 8.4(b). A high magnification bright field TEM image is shown in figure 8.4(c).

We note that, due to this new viewing direction, EDX mapping can be used to observe the precise distribution of cobalt and silver on the sample, without the complication of multiple nanoparticles overlapping. The EDX map is shown in the second image in figure 8.4(d). This map shows a clear spatial separation between the two elements deposited on our sample. This information gives a clear understanding of the distribution of the deposited elements on the sample, thus

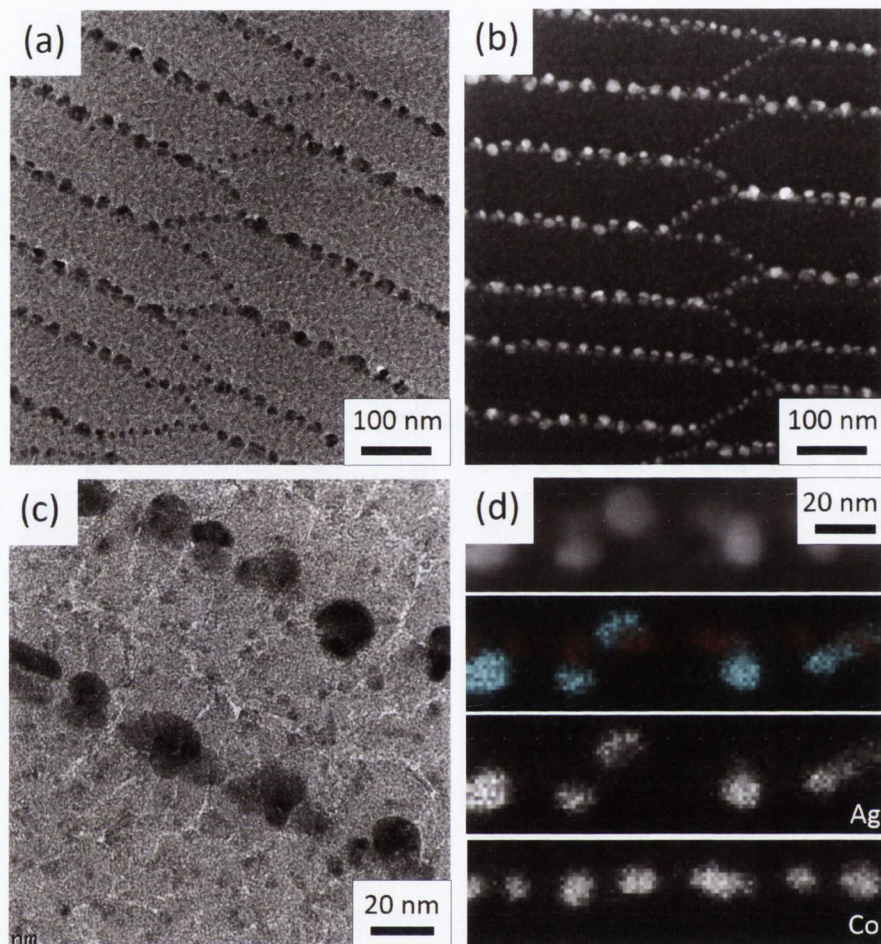


FIGURE 8.4: (a) Bright field TEM image of an overview of the plan view lamella. (b) HAADF image of the nanoparticle array. (c) High magnification image of individual nanoparticles. (d) First image: HAADF image of nanoparticles. Second image: Elemental colour map of the distribution of silver (cyan) and cobalt (red). Third and fourth images: individual maps of the silver and cobalt locations, respectively.

revealing the exact location of each nanoparticle. This TEM measurement can help to establish the origin of any coupling effect between the magnetic Co and the plasmonic Ag nanoparticles.

8.2 HIM Modification of Silicon Lamella

In order to demonstrate the advantages of HIM modification the *in-situ* FIB lift-out technique was used to prepare a lamella of silicon (see appendix C). The final lamella is shown in figure 8.5(a). The sample, sample 1 (see table 8.1), was plasma cleaned for 3 min in a Fischione model 1020 plasma cleaner to further reduce contamination before TEM analysis.

The TEM grid with the silicon lamella was then loaded into the HIM. The lamella was loaded with the normal of the sidewall surface perpendicular to the ion beam, the sample was then tilted 1° into the beam. This geometry has been shown to produce surfaces with minimal damage and implantation layer thickness and reduced surface roughness during ion milling[172].

A focused beam of 35 keV helium ions was scanned over a 500 nm wide region of the lamella sidewall. This step was conducted a number of times in adjacent regions in order to optimize the dose. The area used in our analysis was exposed to a dose of 3.4×10^{16} He⁺/cm². The beam current used was 1.2 pA. The beam was rastered in a single scan over the area with a pixel spacing of 1 nm and a dwell time at each point of 1.3 ms. The sample was rotated through 180° and the process was repeated on the opposite sidewall. The scanning time per sidewall was 68 seconds.

A second silicon sample, sample 2, was also produced by the *in-situ* FIB lift-out technique. An additional final step was performed in the FIB. A 5 keV gallium beam energy at a beam current of 20 pA was scanned at 2° relative to the sidewall of the sample on either side for one minute each side in order to minimise sample damage.

This sample was loaded into the HIM in the same upright manner. This sample sidewall was tilted 15° to the beam and a 300×200 nm area was exposed to a dose of 6.2×10^{18} He⁺/cm². The beam current used was 3.4 pA. The beam was rastered

in a single scan over the area with a pixel spacing of 0.7 nm and a dwell time at each point of 5 ms. The total scanning time was 612 seconds. This process produced a hole straight through the lamella. The purpose of this exposure geometry was to produce a wedge shape of silicon within the lamella so that we could observe the minimum thickness dimensions which can be fabricated by HIM. It also allows us to analyze the subsurface modification effects due to helium ion implantation. All helium ion patterning was performed with the integrated pattern generator on the tool.

A summary of the treatment processes employed in the preparation of the two Si samples is given in table 8.1.

Si sample	FIB treatment	HIM treatment
Sample 1	30 keV Ga ⁺ mill	35 keV He ⁺ polish @ 1° (on both sides)
Sample 2	30 keV Ga ⁺ mill & 5 keV Ga ⁺ polish	35 keV He ⁺ mill @ 15°

TABLE 8.1: The preparation methods used on the two different silicon samples.

8.2.1 Results and Analysis of Silicon Modification

Figure 8.5(a) is an SEM image of sample 1. It shows the silicon lamella after FIB lift-out and thinning. Figure 8.5(b) shows the STEM-HAADF image of the lamella after HIM modification. The three dark vertical grooves indicate the areas modified in the HIM. In figure 8.5(b) one effect of the helium ion modification process is clear; material is selectively removed from the sample sidewalls.

The thickness map of the modified area is shown in figure 8.5(c). From this map we can calculate thickness values based on the mean free path, λ , of a 300 keV electron in silicon ($\lambda = 180$ nm)[173]. The arrows on the image indicate the regions from which the integrated intensity profiles were plotted in figure 8.5(d). The dashed red line is from a region prepared by gallium ions only. The solid blue

line is from the helium ion modified area. The profiles both show an increase in thickness with increasing distance from the top of the lamella, indicating that the sample has a wedge shape. This shape is typical of FIB prepared samples. The increase in thickness is more gradual and noticeably smoother after helium ion modification. The modified area was observed to be consistently thinner than the unmodified region. The helium ion beam is therefore removing material from the sidewall of the sample while also leaving the surface smoother.

Figure 8.5(e) shows the EFTEM gallium map of the region. The areas of higher intensity in this map have a greater concentration of gallium contamination. The solid red arrow indicates the region from which the integrated intensity profile in figure 8.5(f) was plotted. The solid white line is below the FIB prepared areas, while the dashed green line is beneath the areas further modified by helium ions. In figure 8.5(f) the intensity profile from figure 8.5(e) was plotted with the corresponding ion beam used to modify the area indicated below. This graph clearly shows a significant reduction in gallium contamination implanted by the FIB lift-out process. Typically around a 32 % reduction in gallium concentration was achieved by HIM modification. This reduction occurs due to the sputtering of material from the Ga^+ implanted sample sidewall.

HRTEM was performed on the HIM modified grooves and the unmodified sidewalls to afford further insight into the material modification. Figures 8.6(a) and (b) are the HRTEM image of the unmodified region of silicon and its corresponding Selected Area Electron Diffraction (SAED) pattern respectively. Figures 8.6(c) and (d) are the HRTEM image of the HIM modified region of the sample and the corresponding SAED pattern respectively. Figure 8.6(a) displays a noisy HRTEM image when compared with that of figure 8.6(c) from the HIM modified region of the sample. The inset Fast Fourier Transform (FFT) of the images also show the increase in high frequency information attained from the modified region. The uniform background contrast of the modified area indicates that it has a more uniform thickness. These images indicate that the FIB induced amorphous layer

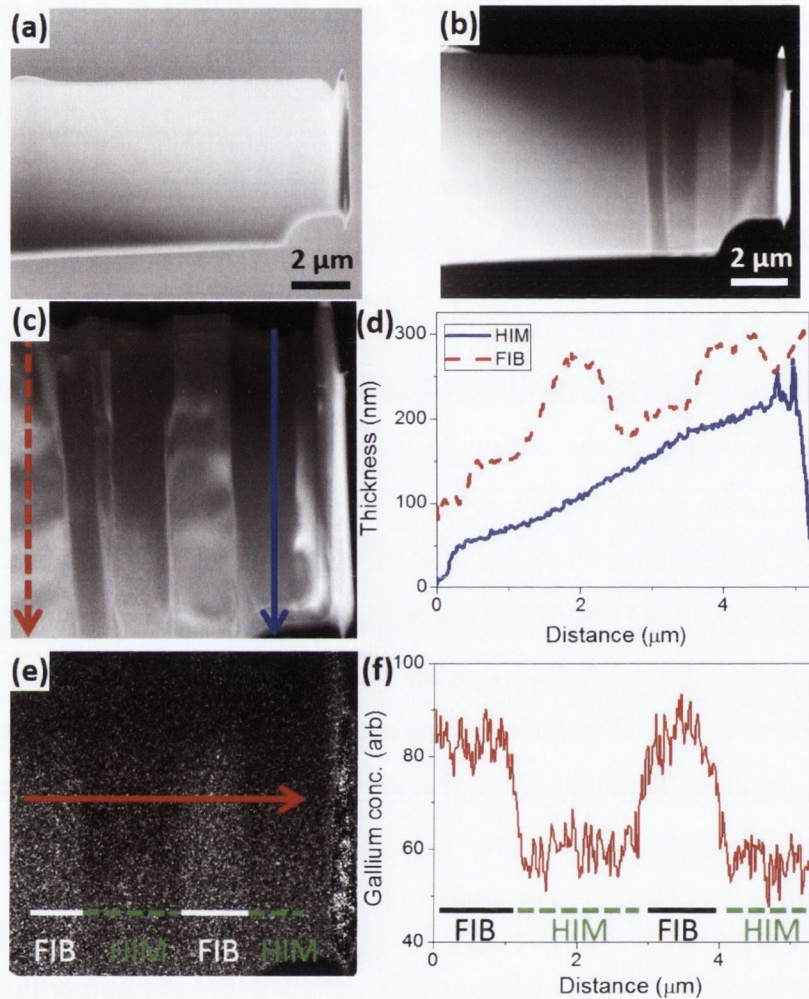


FIGURE 8.5: (a) SEM image of the silicon lamella after FIB preparation. (b) STEM HAADF image of the sample after three separate areas (observed as three vertical dark streaks) were modified by helium ions. (c) Thickness map of the modified area. The dashed red arrow is on an unmodified area of silicon. The solid blue arrow is on a HIM modified area. (d) The intensity profiles of the arrows from (c) are plotted, with the thickness calibrated. (e) EFTEM map indicating the distribution and concentration of gallium. The solid red arrow indicates the area from which (f) is plotted. The areas above the solid lines marked FIB have not been modified with helium ions, the areas above the dashed line marked HIM have been modified with helium ions. The integrated intensity profile from the arrow in (e) is plotted with the ion beam used to modify the region indicated below.

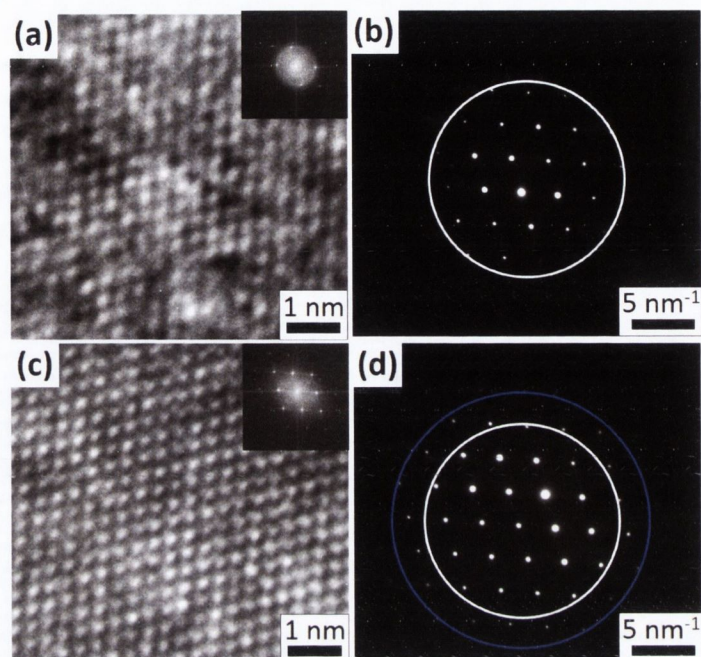


FIGURE 8.6: (a) HRTEM and (b) diffraction information from Ga^+ finished region. (c) HRTEM and (d) diffraction information from helium modified region. The area between the two circles in (d) shows the extra diffractions spots recorded after HIM modification.

of material on the sample, which contributes only noise, was reduced by HIM modification.

Similarly, the SAED pattern in figure 8.6(b) shows less information than that in figure 8.6(d). The extended high frequency information is represented in the diffraction pattern in figure 8.6(d) by the points which lie between the two circles. The diffraction spots which are furthest from the centre of the image represent the highest spatial frequencies. The diffraction pattern recorded from the HIM modified region in figure 8.6(d) indicates that this area of the sample is thinner, while still retaining its high quality crystalline structure. The diffraction patterns show that the sample was tilted to $[011]$.

This analysis of sample 1 clearly shows that HIM modification of a FIB prepared TEM lamella can be used to further reduce sample thickness while removing contamination and also retaining the crystallinity of the material.

In sample 1 a lamella finished only with 30 keV gallium ions in the FIB was used. A lower energy gallium ion beam can be used to produce lamellas with significantly less FIB induced damage[174]. FIBs with low energy capability have become more widely available over the past few years. We prepared the silicon lamella in sample 2 with a 5 keV gallium ion beam final polish in order to reduce FIB induced artefacts which would obscure our analysis of the patterning and subsurface modification effects of the HIM modification.

Sample 2 is shown after FIB lift-out in the SEM image in figure 8.7(a). The sample has uniform contrast. At 5 keV the average penetration depth of electrons in silicon is ~ 200 nm. For this 100 nm thick sample the secondary electron image shows the thickness variation across the lamella. The sample can therefore be seen to have a uniform thickness. Figure 8.7(b) is an image of the sample in the HIM. This is the sample before HIM milling, the surface is smooth and uniform. Figure 8.7(c) shows the sample after HIM irradiation. A hole can now be seen in the sample due to the HIM milling process. There is also a bulge in the sample beneath this hole. Figure 8.7(d) is an illustration of the beam-sample geometry used to modify the sample in the HIM. The sample sidewall was inclined 15° to the beam. This geometry was used in order to mill a wedge shape within the lamella in order to observe the minimum thickness dimensions which can be fabricated by HIM. This geometry also shows the extended effects of the modification process as the distribution of the ions within the sample can be observed.

Figure 8.8(a) is a bright field TEM image of the area of the sample after controlled sidewall modification by helium ion irradiation. Figure 8.8(b) is a HAADF image of the same area. A rectangular hole was observed at the centre of the image, this was fabricated due to the high dose used. Below this hole is a circular region with rapid variations in contrast. This circular area has been heavily modified by the HIM.

Figure 8.9 is a thickness map of the area. Below this map is the integrated intensity profile of the area indicated by the solid red arrow on the thickness map.

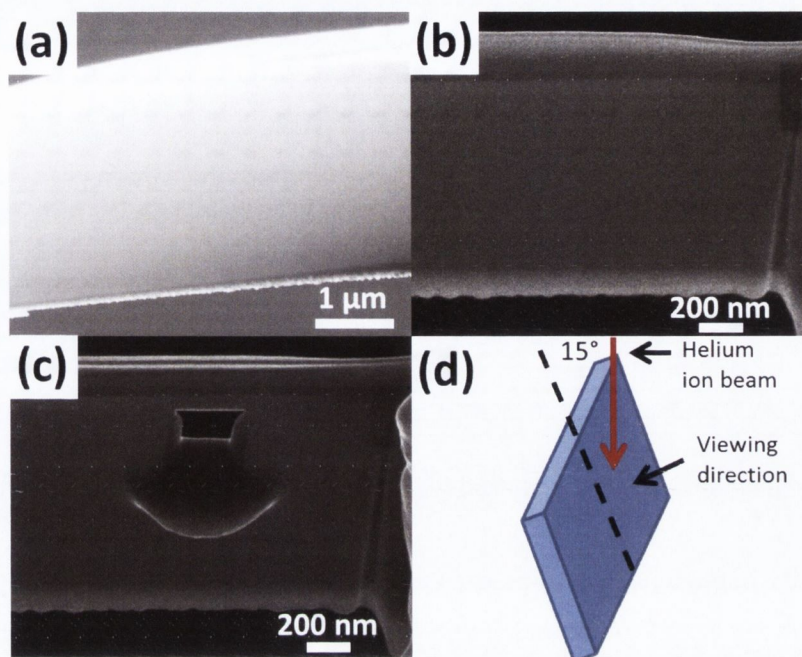


FIGURE 8.7: (a) SEM image of the silicon lamella (sample 2) after FIB lift-out. (b) HIM image of the sample. (c) HIM image of the sample after the modification process. (d) An illustration of the beam-sample geometry used to modify the sample in the HIM.

This profile shows the sloping thickness of the wedge fabricated by helium ion irradiation, followed by the hole where the beam penetrated the lamella. Finally, the circular feature is observed to have rapidly varying thickness. The hole has a non-zero thickness due to the limitations of the thickness mapping process, such as its tendency to overestimate the thickness of very thin areas[175].

It is well known that helium ion irradiation, with an appropriate beam energy, can produce helium bubbles beneath the surface of a sample[176]. In this case the centre of the circular feature is approximately at the mean implantation depth of 35 keV helium ions in silicon, 318 nm (SRIM)[122]. This is made clear by the SRIM simulation image inset in figure 8.8(b) showing the distribution of 35 keV helium ions in silicon; this simulation has the same scale as the image and correlates well with our experimental data.

What we observe in this region is the implantation of helium ions, where the incident helium ions have been scattered by the silicon and have come to rest

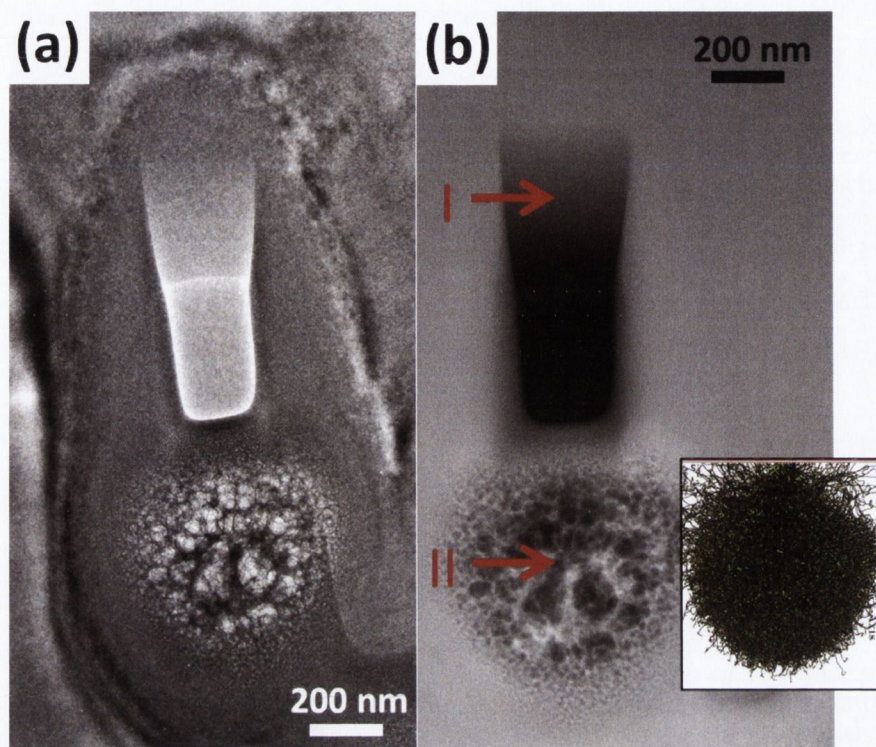


FIGURE 8.8: (a) Bright field TEM image of the area modified by helium ions. (b) HAADF image of the modified area. I shows the location of the wedge shape and II shows the circular area with bubbles. Inset is a SRIM simulation of 35 keV helium ions in silicon with the same scale as the image.

within the sample. These implanted ions then lead to the formation of bubbles beneath the surface which stretch and distort the silicon. The contrast observed corresponds to regions where helium bubbles have formed and silicon has been displaced. The swelling of this region is also apparent from the HIM image in figure 8.7(c).

At this point the morphological changes induced by a high dose of HIM irradiation on sample 2 have been described. We then investigated the effect of the HIM modification on the structure of the silicon. Figure 8.10(a) is a graph of the EELS spectra recorded from three different locations on the sample. The black solid line at the top was recorded at a region which was not modified by helium ion irradiation. The red dashed line in the middle was recorded from the wedge shape region fabricated by helium ion irradiation (marked I in figure 8.8(b)). And finally

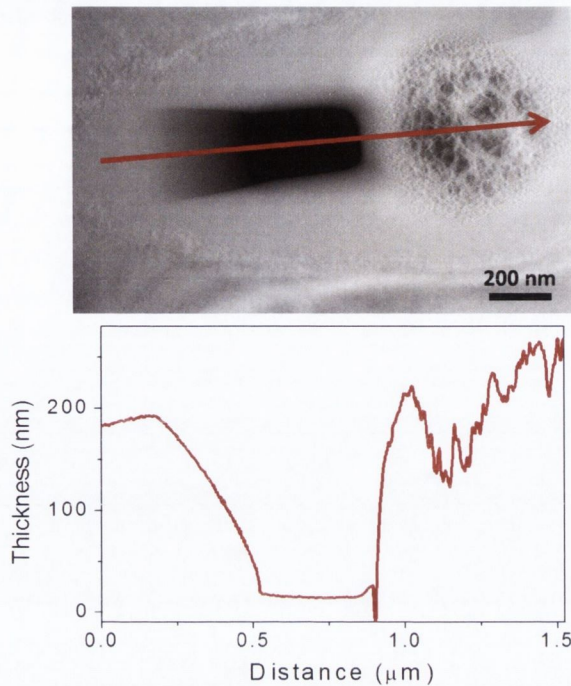


FIGURE 8.9: Thickness map of the modified region. The arrow indicates the area along which the integrated intensity profile below the image is plotted.

the blue dotted line at the bottom was recorded at the circular feature (marked II in figure 8.8(b)).

During analysis of the near-edge structure (ELNES) of the three EELS spectra in figure 8.10(a) (spectra are offset for clarity) the intensity of the first peak in the spectra at 99 eV (the pre-peak) was observed to degrade from the top spectrum to the bottom. We compared our data to the spectra for crystalline and amorphous silicon from a database[177]. The spectra from the database are shown in figure 8.10(b). The intensity of the pre-peak at 99 eV is used as an indication of the crystallinity of the silicon. A higher intensity indicates more crystallinity in that area, a lower intensity corresponds to an area which is more amorphous[178].

The top spectrum in our data corresponds to an area of high crystallinity, as indicated by the presence of the pre-peak in this region of the spectrum. The position of the pre-peaks are shown in figure 8.10(a) by small red arrows. This result was to be expected as the spectrum was recorded at a region unmodified by helium ions. However, the spectrum from the wedge shape area fabricated

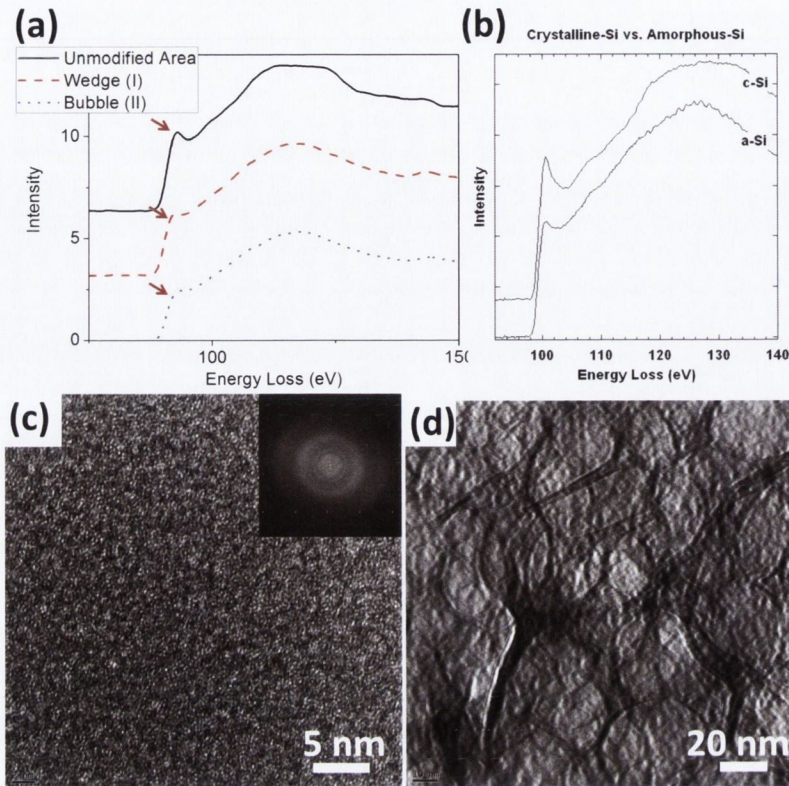


FIGURE 8.10: (a) EELS spectra of an unmodified area of silicon (solid black line), the HIM fabricated wedge marked I in figure 8.8(b) (dashed red line) and the circular featured marked II in figure 8.8(b) (dotted blue line). The red arrows indicate the position of the Si pre-peak. (b) EELS spectra of crystalline (top) and amorphous (bottom) silicon taken from the database in reference[177]. (c) HRTEM image of the wedge shaped area (I in figure 8.8(b)) and FFT inset. (d) HRTEM of the circular feature (II in figure 8.8(b)).

by the HIM (marked I in figure 8.8(b)) shows a high degree of amorphisation as the intensity of the pre-peak at 99 eV is greatly reduced. The spectrum from the area of the sample containing the bubbles (marked II in figure 8.8(b)) shows an area which is even more amorphous again as the pre-peak intensity has been further reduced. Another factor which will reduce the crystallinity measured is the sample thickness. As the sample gets thinner the amorphous layer remains the same thickness and the crystal region reduces in thickness. The proportion of amorphous to crystalline material therefore increases with decreasing thickness.

Figure 8.10(c) is a HRTEM image from the wedge area (marked I in figure 8.8(b)) with an inset FFT of the image. This image shows only amorphous material

is present at this location. Figure 8.10(d) is a HRTEM image of the area with the circular feature (marked II in figure 8.8(b)). This image shows the presence of circles created by the growth of helium bubbles. No crystal structure was observed in this region either.

It was observed that a high dose of HIM irradiation on sample 2 was used to fabricate a smooth wedge of material on a TEM lamella with minimum thickness dimensions of just a few tens of nanometres. This thickness may even be less than our thickness map indicates as significant errors may be present in the mapping process for very thin samples due to surface excitations, which can lead to overestimation of the thickness in this region[175]. The lateral dimensions of the pattern can also be tailored with a high degree of precision. The EELS spectra and HRTEM from the HIM modified areas show that the wedge fabrication process caused significant amorphisation of the sample in that region. The beam particles were also observed to implant in the sample below the wedge causing bubbles to form in the material, again resulting in significant amorphization of the silicon, as observed by EELS and HRTEM.

In the first part of this chapter the high level of control of a material's geometry by FIB was demonstrated. Cross sectional TEM analysis using FIB sample preparation is an invaluable microscopy technique for the characterisation of solid samples. The *in situ* FIB lift-out technique provides reproducible sample fabrication with high quality, good throughput, site-specificity, thickness control, sample dimension control, and a high sample yield. Critically, the orientation of the FIB prepared sample has typically been limited to a cross sectional view and may not provide sufficient information about the sample regardless of the TEM analysis technique employed.

An *in situ* lift-out for plan view TEM samples has been demonstrated to provide information beyond that observed in a conventional cross sectional sample. The

self-assembled nanoparticle arrays on the stepped template, investigated herein, is just one sample type which benefits from plan view TEM. Plan view TEM analysis can potentially be of great interest for a wide range of samples such as: sub 10 nm featured wire[179] and dot arrays[180] fabricated using block copolymer techniques, nanowires, nano-contacts, and a large variety of structures and geometries patterned using top down lithography[181]. This will lead to higher resolution imaging and enhanced understanding and control of these physical systems.

In the second part of the chapter it was demonstrated, using sample 1, that a focused helium ion beam can modify a surface's physical properties, such as crystallinity, roughness and thickness, in a controlled manner. The helium ion beam is non-contaminating and can even be used to selectively remove surface contaminants, such as the gallium contamination removal demonstrated here.

It has also been shown, using sample 2, that a finely focused beam of helium ions can sputter material from a sample with a high level of control, allowing sub 10 nm features to be patterned. This high dose irradiation can also be used to modify the structure of a material, as demonstrated by our EELS and HRTEM results. Helium ion irradiation is a widely studied field in nuclear physics. Helium ion irradiation has been used to modify mechanical[182], optical[176] and magnetic[183] properties of surfaces. The highly focused probe of the helium ion microscope provides a greater level of spatial control than previously available for such experiments.

These results clearly show the effect of the beam-sample interaction process. This chapter has defined some issues which are not present during the processing of 2D materials such as the beam broadening and helium bubble formation within the sample. This knowledge is required to further progress to the well controlled processing of 3D materials.

Chapter 9

Conclusion & Future Work

Within this thesis the suitability of a range of charged particle beams to the modification of various materials has been demonstrated. The advantages of using electron and ion beams is the high level of spatial, as well as dose, control.

A low-energy electron beam in the presence of a nitrogen atmosphere was used to remove carbon atoms from a graphene lattice. This effect was confined to within a few tens of nanometres of the beam location on the sample. Nanopores with a diameter of < 10 nm were fabricated. A high density of these pores can be fabricated in order to remove larger areas of material. A model was also developed to describe this etching method.

For a more controlled approach a beam of ions can be used to directly modify and mill a material. Raman spectroscopy was used to find the relationship between the dose of He^+ and the damage introduced into graphene's structure. Doses above $5 \times 10^{14} \text{ He}^+/\text{cm}^2$ were found to cause significant damage to the graphene lattice. The presence of a substrate beneath the graphene was observed to enhance the rate of damage. High magnification images exploiting the sub-nanometre resolution of the HIM were found to introduce significant damage to the graphene structure.

Freestanding graphene was used to produce GNRs 15 nm in width. The ribbons were patterned with various orientations and represent the flexibility of the patterning capabilities of the HIM. This milling capability was also demonstrated on MoS₂. The MoS₂ flakes were analysed by high-resolution STEM to determine the extension of the damage from the milled edge. It was found that zigzag edges with no observable damage could be fabricated.

An electron beam was used to deposit carbon in a hole milled by HIM in an MoS₂ flake. Further e-beam exposure caused partial annealing of the carbon structure. This fabrication technique enables the production of heterojunctions with unique properties.

The ion beam modification was then extended to 3D samples. A gallium ion beam was first used to demonstrate the arbitrary geometries into which materials can be patterned. A thin section of material was extracted from a sample to demonstrate the application of the technique to TEM sample preparation. The gallium ion beam can be used to extract not just the typical cross-section samples but also more complex sections such as plan view. A beam of helium ions was then used to afford further control of the thickness and quality of the lamella. Damage introduced by the aggressive milling of the gallium ion beam was reduced by exposure to the helium ions.

The electron, gallium ion and helium ion beams used herein were shown to provide the control required to tune the properties and geometry of both 2D and 3D materials.

The techniques developed in this work have been shown to provide a high level of control of the material systems investigated. Further work based on these results can lead to many new discoveries and applications. Examples of directions which may be taken to build on this work are given below.

An attempt to control the rate of the electron beam etching of graphene by changing the sample temperature was made. This could lead to a better understanding of the mechanism occurring. However, a change in etching rate due to a change in temperature was not observed. Perhaps with a greater temperature range an effect could be observed and studied systematically, the experiment in this work was limited to $-25 - +50^\circ$. It could then be incorporated into the model in chapter 5. The electron beam etching, as seen with graphene, was not demonstrated on any other materials. A suitable reaction between nitrogen and MoS_2 may not exist. Other materials such as MoSe_2 , MoTe_2 or BN could be investigated. As well as trying a range of materials, the gas species in the chamber could also be varied. A more reactive species may result in more efficient etching. This technique could be used to create porous 2D materials for filtration[3] or hydrogen storage[4].

The damage production rate as a function of helium ion dose was established for graphene. This relationship can be found for other materials such as MoS_2 . The ability to tune the structure of 2D materials can provide a means to tailor their electrical properties. *In situ* electrical characterisation during the ion irradiation can be used to confirm this effect. Devices with a specific electrical response could then be produced.

The milling of structures within graphene by HIM was preliminarily investigated. Fabrication of GNRs was achieved. Low-energy, aberration-corrected TEM or STEM is required to observe the extension of the damage created due to the milling. Electrical characterisation is also required in order to determine if a band gap was opened. A band gap in graphene is a very desirable feature required for switching operations. Graphene can be operated at very high frequencies due to its carrier mobility[55], if this could be coupled with a high on/off ratio ($>10^{-7}$ [10]) then it would be a strong contender for replacing silicon in semiconductor devices.

Milling of MoS_2 flakes was also demonstrated with a focused helium ion beam. The initial results show that the edges of the milled structures can be produced without observable structural damage. However, this was not always the case. It will need

to be investigated whether it is the instability of the beam in the HIM due to environmental influences, or the edge reactivity of the sample after milling, or even the beam-induced damage in the TEM which causes the inconsistencies observed in the current results. Nanostructured MoS₂, such as nanoribbons, have unique properties which can be tuned for specific applications[8]. Upon optimisation of the technique, a focused helium ion beam could be used to realise such structures.

Electron beam induced deposition of carbon into nanostructured MoS₂ flakes was demonstrated. The e-beam annealing needs to be optimised in order to fully crystallize the carbon structure in the milled hole in the MoS₂ flake. This technique can then be extended to a range of different materials. Not only can various types of flakes be milled, but a material other than carbon could be introduced into the hole by dropping a solution onto the sample. A large range of heterostructures with different properties could be created with this method.

Finally, a high level of control of a material's geometry using a combination of a focused Ga⁺ beam and a focused He⁺ beam was demonstrated. The TEM lamella preparation demonstrated in chapter 8 shows how extraction of sections of different geometries from a sample can provide an enhanced understanding of the original sample during TEM analysis. Different geometries of lamellas may provide further complementary information. HIM modification of the surface of 3D structures, such as TEM lamellas, by glancing angle irradiation requires further optimisation. Demonstration of the resilience of the HIM polishing technique using a range of materials would serve to greatly enhance its usefulness.

Overall it is clear that the many findings of this work pave the way for more investigations in order to build on these results. A deeper understanding of the results presented here can be gained from further modelling and experimentation as outlined above. Our focus has been on the development of fundamental modification techniques. Future work may focus on optimising these techniques and extending them to a greater range of material systems.

Appendix A

Tool Specifications

Tool Name	Manufacturer	Source	Resolution	Beam Energy Range	Beam Current Range	Acquisition Parameters
Scanning Electron Microscope	Carl Zeiss	Schottky FEG	1 nm @ 15 kV	0.5 – 30 kV	9 pA – 6 nA	1,024×768 scan resolution and 10 μ s dwell time
Helium Ion Microscope	Carl Zeiss	Gas Field Ion Source	0.35 nm @ 30 kV	5 – 35 kV	0.1 – 10 pA	1,024×1,024 scan resolution, 1 μ s dwell time and 64 line averages
Transmission Electron Microscope	FEI	Schottky FEG	0.14 nm in TEM, 0.12 in STEM (both @ 300 kV)	80 – 300 kV	1pA – 100 nA	2,048×2,048 image resolution and 1 s acquisition time in TEM mode. 1,024×1,024 scan resolution and 64 μ s dwell time in STEM
Raman Spectrometer	Horiba	633 nm HeNe Laser	1 μ m lateral, 0.1 nm spectral			10 s acquisition time and 2 spectrum averages
Energy Dispersive X-ray Spectrometer	EDAX		129 eV spectral			200 s acquisition time
Electron Energy Loss Spectrometer	Gatan		0.8 eV spectral			20 s acquisition time

TABLE A.1: Table of the specifications of the tools used throughout this work.

Appendix B

Source Building Procedure for the Helium Ion Microscope

The most commonly used ion microscope source is the Liquid Metal Ion Source (LMIS). In the LMIS of a FIB the gallium is heated to a liquid state and flowed to the apex of a sharp tungsten needle. An electric field is applied to this tip until gallium ions are field evaporated from the source. The LMIS is limited by a relatively large energy spread of 5 – 10 eV[184]. This energy spread leads to chromatic aberration whereby ions of different energies are focused onto different planes within the microscope. This results in the ions being focused on a disc area on the sample, instead of a single point. This chromatic aberration currently limits the resolution of the FIB to 3 – 5 nm at best[120]. The ion source in the HIM is a gas field ion source (GFIS). This type of source can produce an ion beam with an energy spread of just 0.5 eV[185], leading to a significant reduction in chromatic aberration and an order of magnitude enhancement in resolution over the FIB.

The HIM source consists of the emitter, a cryogenically cooled, sharpened tungsten tip, which is held at a positive bias of 25 – 35 kV during operation. The bias is adjusted outside of this range, from 10 – 50 kV, during the trimer building process.

B.1 Forming a Trimer

Before beginning this procedure the helium gas pressure should be reduced from the typical 5×10^{-6} Torr to 2×10^{-6} Torr. A reduced gas pressure helps to reduce the risk of an electrical arc between the source and the extractor. Arcing is very damaging to the source and can lead to a replacement source being required. The beam limiting aperture should also be removed as it would limit our view of the source during this procedure. All of the electronic beam alignments such as tilt, shift, pan, stigmators and scan rotation should be set to zero. New alignments will be required for the new trimer. It should also be ensured that a featureless, conductive surface is centred under the beam. This is required for viewing the source.

The first step is the ‘source forming’ process. During the source forming the emitter is heated while a bias is also applied. This allows the emitter geometry to be altered, making it either sharper or more blunt. A higher bias or a higher temperature will cause the emitter to elongate. During operation a bias is applied to the emitter in order to produce a sufficient electric field, within the immediate vicinity of the emitter tip, to ionise helium atoms. Assuming the same bias is applied, a sharper emitter will have a higher electric field at its tip. This results in a lower bias being required when a sharper emitter is formed.

Once the emitter has been shaped the ‘trimer forming’ procedure can begin. The bias on the emitter will be 10 kV after the source forming completes. This value is then increased manually. Initially the field at the emitter tip will not be sufficient to observe any helium ionisation. Typically at ~ 25 kV the first signs of emission are observed. The applied bias begins to field evaporate atoms from the tip until the surface is smooth and uniform. At ~ 35 kV the first observation of the atomic structure of the tip of the emitter is observed. this pattern is shown in figure B.1(a). This is often referred to as ‘the rose pattern’ and is indicative of a well structured tip.

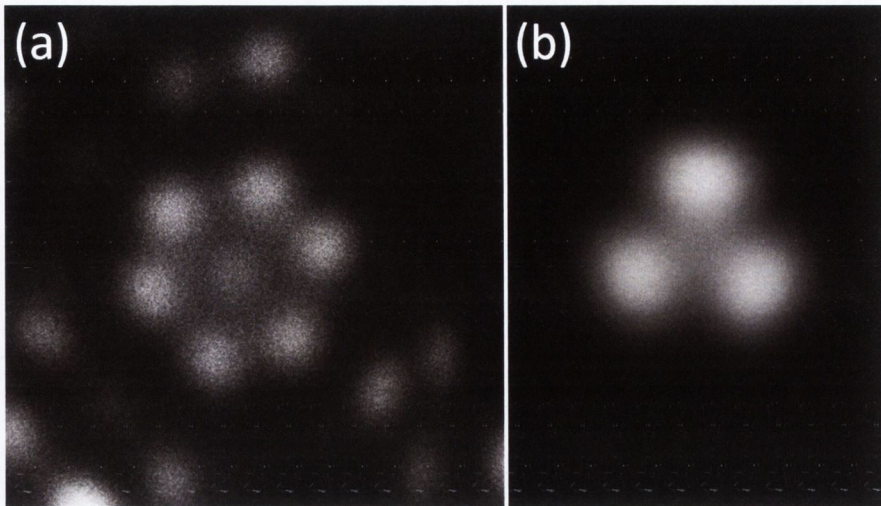


FIGURE B.1: (a) The rose pattern showing good crystallographic structure of the emitter in the HIM. (b) The trimer of atoms, one of which is used as the source of the HIM.

The bias is further increased, slowly enough that at this point individual atoms are being removed from the tip. Field evaporation will remove atoms until finally a stable arrangement of three atoms, the trimer, is observed. A trimer is shown in figure B.1(a). The tip bias is then adjusted, usually reduced by a few kV, in order to maximise the electric field strength at the trimer of atoms. This value is known as the Best Imaging Voltage (BIV).

As discussed earlier a sharper emitter will produce a sufficient ionisation field at a lower bias. In this case the BIV is also lower. A low BIV is typically not ideal for several reasons. Firstly, a low BIV results in a lower beam current. For milling, spectroscopic analysis or backscattered ion imaging a large beam current is a prerequisite. A larger beam current also affords more flexibility in the alignments, typically allowing a smaller probe to be formed while maintaining a useful beam current. Secondly, a large bias on the tip helps to keep it free of contaminants. A lower bias therefore leads to a shorter trimer lifetime. Finally, the BIV is the upper limit to the range of acceleration voltages which can be used during operation.

If it is the case that the BIV is too low (below 25–30 kV) then a procedure to make the tip more blunt is available. This is called annealing. Annealing the emitter

consists of heating it, with no bias, allowing it to both reflow to a more rounded shape, and also to recrystallize. The recrystallization effect may be required if the rose pattern is not observed when forming a trimer.

By careful optimisation of the source geometry a well shaped emitter tip can be formed. A trimer with a good beam current and a good lifetime should be the result of this optimisation. The beam current is measured when one of the atoms of the trimer is aligned to the optical axis of the column. A value from 10 pA up to 30 pA is considered good. The value which is determined by the manufacturer to be 'in spec.' is >5 pA. A good lifetime is 2–3 weeks. In fact in many cases the trimer may last much longer but the beam current diminishes over the lifetime of the trimer. As such, the trimer is typically of little use after more than three weeks and a new one must be formed.

When a new trimer is required the source forming process need not be attempted immediately. Instead the emitter bias can be slowly increased until the trimer is removed. The bias is then further increased until another trimer is isolated. If none is found the source forming must be done.

B.2 Aligning the Upper Column

Now that a good trimer has been formed the rest of the column must be aligned. The atom which appears brightest is the one which provides the greatest emission source. This is the atom to which the column is aligned. The voltage on the condenser lens, lens 1, is reduced such that the beam crossover point is in a plane below the beam limiting aperture. The trimer is observed on the screen and the source unit is physically tilted until the emission atom is centred on the screen. The lens 1 voltage is then increased in order to bring the crossover above the aperture. The image of the trimer will have inverted, and also moved. The source unit is manually shifted in order to recentre the emission atom. This is an

iterative process which brings the trimer approximately onto the optical axis of lens 1. Three to five iterations is typically sufficient.

A large ($20\ \mu\text{m}$) aperture is then inserted. This aperture must be aligned to the optical axis of lens 1¹. While viewing the source lens one can be focused onto the aperture plane so that the aperture can be seen. The aperture is then moved to the centre of the screen using the aperture positioning motors. The new aperture co-ordinates are saved.

B.3 Aligning the Lower Column

The beam must next aligned onto the optical axis of lens 2. Lens 1 is adjusted so that the aperture is no longer in focus and the trimer can once again be seen. The preset lens 1 value of spot 5 is selected. This value simply corresponds to a pre-defined lens 1 voltage which is set by the manufacturer. The emission atom of the trimer is electronically tilted to the centre of the screen. The sample is then viewed. The field of view should be around $\sim 10\ \mu\text{m}$. An oscillating voltage, or voltage wobble, is applied to lens to 2. The image will be observed to move laterally as the sample image goes in and out of focus. The electronic beam shifts are used to remove this movement and bring the beam into the centre of the lens. As with the lens 1 alignment this is an iterative process requiring several adjustments of tilt and shift, until no more improvements can be made.

The balance of the quadropoles is checked next. The sample is viewed at a higher magnification (Field of view $< 5\ \mu\text{m}$). A voltage wobble is applied to two of the segments of the quadropoles which are positioned opposite each other. This wobble causes the image to move laterally. The bias ratio applied to the two segments is adjusted to minimise this movement. The process is then repeated on the two remaining segments in the quadropole.

¹The reason that the aperture needs to be re-aligned is because the alignment of the trimer to lens 1 is not perfectly accurate.

A final check is performed to ensure that the trimer is still centred and that the lens 2 wobble produces no lateral movement of the image. The gas pressure is brought back up to 5×10^{-6} Torr. The lens 1 setting is adjusted to spot 4. The 20 μm aperture should still be inserted. These are the standard conditions at which the beam current is recorded. This is the value referred to earlier which should be greater than 5 pA.

The 10 and 5 μm apertures can be aligned in the same way as the 20 μm aperture. The aperture is inserted, focused on with lens 1 and moved into the centre of the screen. The electronic tilts and shifts are again optimised. It is not necessary to adjust the quadropole balancing.

The optimum parameters for high resolution imaging are a 10 μm aperture with a spot number (the lens 1 strength) which brings the beam current down to ~ 0.5 pA. The spot number required to achieve this will vary for each trimer but is typically 5–8.

The source building procedure requires experience to perfect. The shaping of the tip using successive builds and anneals is somewhat of a ‘dark art’. The patience required to slowly increase the extraction voltage in order to remove all but three atoms from the emitter tip is something that can’t be taught. However, the procedure does become routine after several attempts and a trimer can be formed and aligned in less than an hour if no issues are encountered.

Appendix C

FIB Lift-Out Procedure

This is an overview of the typical TEM sample preparation process carried out in the FIB. The Al_2O_3 sample introduced in chapter 8 will be used to illustrate the process. Electrically insulating samples were coated with ~ 5 nm of metal (typically Au or Au/Pd) in a sputter coater. The sample was loaded into the FIB. The sample was brought to the eucentric height, at this height the tilt plane is equivalent to the sample surface, tilting therefore doesn't cause the sample to shift laterally. A 5 mm working distance was used. The electron and ion beams were aligned to co-incidence with the sample surface perpendicular to the ion beam. The FIB was equipped with a Kleindeik Nanotechnik micromanipulator needle and a Picoprobe Gas Injection System (GIS) system for the lift-out procedure.

The first step in any lift-out procedure is to deposit a protective layer of platinum on the region of interest in the FIB. Electron beam induced decomposition of an organo-metallic precursor ($((\text{CH}_3)_3\text{Pt}(\text{CpCH}_3))$) was used to deposit a 100 nm thick layer of platinum over an area of $6 \times 1.5 \mu\text{m}$. The time taken to deposit this layer depends on the electron beam parameters. A higher beam current or a lower beam energy will increase the rate of deposition. Typical parameters used were 3 nA beam current and 2 keV beam energy. With these parameters the deposition time was ~ 3 min. E-beam platinum was deposited before turning on the gallium

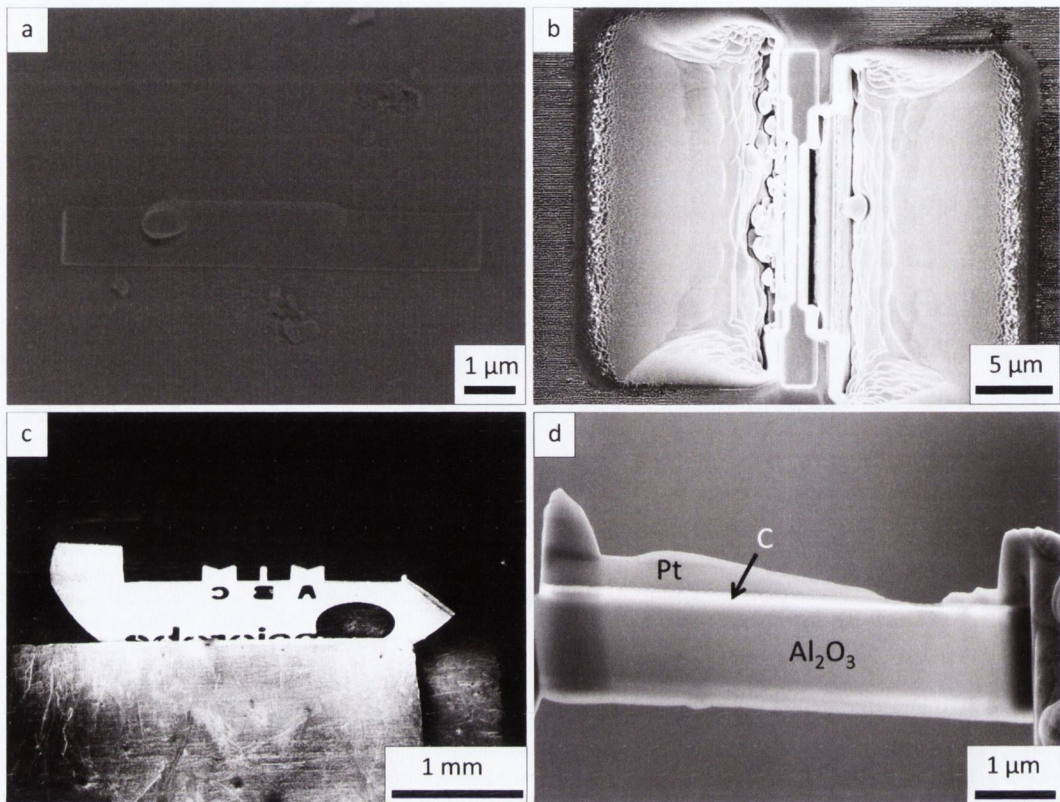


FIGURE C.1: (a) Platinum strap deposited on the substrate surface by electron beam and ion beam induced deposition. (b) Plan view of the two trenches cut with the ion beam leaving a thin section of material isolated at the centre. (c) Omniprobe TEM lift-out grid mounted vertically on a sample holder. (d) SEM image of the final lamella.

ion beam to ensure that the region of interest was protected from exposure to any damaging gallium ions. Ga^+ beam induced deposition was then used to deposit a further $1 \mu\text{m}$ thick layer of platinum over a $12 \times 2 \mu\text{m}$ area. A 100 pA , 30 keV ion beam requires ~ 5 minutes to deposit this layer. The resulting platinum rectangle can be seen in figure C.1(a).

A 10 nA Ga^+ beam was used to mill a trench to a depth of $10 \mu\text{m}$ either side of a $1.5 \mu\text{m}$ thick section of material. This lamella was thinned to $1 \mu\text{m}$ with a 2 nA ion beam. The trenches are shown in figure C.1(b). One side of the lamella was freed from the substrate with a 2 nA ion beam. The sample was tilted 49° relative to the ion beam and the lamella was undercut, leaving it supported on only one side. A micromanipulator needle was brought in to contact with the free side of

the lamella and affixed with platinum by electron beam induced deposition. The lamella was then cut free from the substrate with a 2 nA ion beam and transferred to an Omniprobe TEM lift-out grid mounted vertically in a sample holder as shown in figure C.1(c).

The sample was thinned to 300 nm with an ion beam current of 200 pA with the lamella sidewall at an angle of 1° relative to the ion beam. The sample was then thinned to 100 nm with a 20 pA ion beam at an angle of 0.7° .

In order to produce lamellas of the highest quality a low energy gallium ion polish was used. A 5 keV gallium beam energy at a beam current of 20 pA was scanned at 2° relative to the sidewall of the sample on either side for one minute each side. This step is known to reduce the FIB induced amorphisation and implant layer to just ~ 2 nm, roughly ten times less than the damage layer produced by 30 keV gallium ions[174]. The final lamella is shown in Fig. 2(d).

Bibliography

- [1] K. S. Novoselov, A. K. Geim, S. V. Morozov, D. Jiang, Y. Zhang, S. V. Dubonos, I. V. Grigorieva, and A. A. Firsov. Electric field effect in atomically thin carbon films. *Science*, 306(5296):666–669, 2004.
- [2] K. S. Novoselov, V. I. Fal’ko, L. Colombo, P. R. Gellert, M. G. Schwab, and K. Kim. A roadmap for graphene. *Nature*, 490(7419):192–200, 2012.
- [3] S. Blankenburg, M. Bieri, R. Fasel, K. Mullen, C. A. Pignedoli, and D. Passerone. Porous graphene as an atmospheric nanofilter. *Small*, 6(20):2266–2271, 2010.
- [4] A. Du, Z. Zhu, and S. C. Smith. Multifunctional porous graphene for nano-electronics and hydrogen storage: New properties revealed by first principle calculations. *Journal of the American Chemical Society*, 132(9):2876–2877, 2010.
- [5] G. F. Schneider, S. W. Kowalczyk, V. E. Calado, G. Pandraud, H. W. Zandbergen, L. M. K. Vandersypen, and C. Dekker. DNA translocation through graphene nanopores. *Nano Letters*, 10(8):3163–3167, 2010.
- [6] B. W. Ward, J. A. Notte, and N. P. Economou. Helium ion microscope: A new tool for nanoscale microscopy and metrology. *Journal of Vacuum Science & Technology B: Microelectronics and Nanometer Structures*, 24(6):2871–2874, 2006.

- [7] X. R. Wang, Y. J. Ouyang, X. L. Li, H. L. Wang, J. Guo, and H. J. Dai. Room-temperature all-semiconducting sub-10-nm graphene nanoribbon field-effect transistors. *Physical Review Letters*, 100(206803), 2008.
- [8] E. Erdogan, I. H. Popov, A. N. Enyashin, and G. Seifert. Transport properties of MoS₂ nanoribbons: edge priority. *The European Physical Journal B*, 85(1):1–4, 2012.
- [9] M. Di Ventra, S. Evoy, and J. R. Heflin, editors. *Introduction to Nanoscale Science and Technology*, chapter Nanoscale Fabrication and Characterisation, pages 5–100. Springer, 2004.
- [10] The international technology roadmap for semiconductors. Accessed August 2013. <http://www.itrs.net/>.
- [11] T. Pichler. Molecular nanostructures: Carbon ahead. *Nature Materials*, 6(5):332–333, 2007.
- [12] A. H. Castro Neto, F. Guinea, N. M. R. Peres, K. S. Novoselov, and A. K. Geim. The electronic properties of graphene. *Reviews of Modern Physics*, 81(1):109–162, 2009.
- [13] H. W. Kroto, J. R. Heath, S. C. O’Brien, R. F. Curl, and R. E. Smalley. C₆₀: Buckminsterfullerene. *Nature*, 318(6042):162–163, 1985.
- [14] S. Iijima. Helical microtubules of graphitic carbon. *Nature*, 354(6348):56–58, 1991.
- [15] R. H. Baughman, A. A. Zakhidov, and W. A. de Heer. Carbon nanotubes—the route toward applications. *Science*, 297(5582):787–792, 2002.
- [16] J. A. Spirko, M. L. Neiman, A. M. Oelker, and K. Klier. Electronic structure and reactivity of defect MoS₂: I. relative stabilities of clusters and edges, and electronic surface states. *Surface Science*, 542(3):192 – 204, 2003.

- [17] B. Radisavljevic, A. Radenovic, J. Brivio, V. Giacometti, and A. Kis. Single-layer MoS₂ transistors. *Nature Nanotechnology*, 6(3):147–150, 2011.
- [18] B. Chakraborty, H. S. S. R. Matte, A. K. Sood, and C. N. R. Rao. Layer-dependent resonant raman scattering of a few layer MoS₂. *Journal of Raman Spectroscopy*, 44(1):92–96, 2013.
- [19] R. S. Sundaram, M. Engel, A. Lombardo, R. Krupke, A. C. Ferrari, P. Avouris, and M. Steiner. Electroluminescence in single layer MoS₂. *Nano Letters*, 13(4):1416–1421, 2013.
- [20] H. P. Komsa, J. Kotakoski, S. Kurasch, O. Lehtinen, U. Kaiser, and A. V. Krashenninnikov. Two-dimensional transition metal dichalcogenides under electron irradiation: Defect production and doping. *Physical Review Letters*, 109:035503, 2012.
- [21] V. Nicolosi, M. Chhowalla, M. G. Kanatzidis, M. S. Strano, and J. N. Coleman. Liquid exfoliation of layered materials. *Science*, 340:6139, 2013.
- [22] J. S. Ross, S. Wu, H. Yu, N. J. Ghimire, A. M. Jones, G. Aivazian, J. Yan, D. G. Mandrus, D. Xiao, W. Yao, and X. Xu. Electrical control of neutral and charged excitons in a monolayer semiconductor. *Nature Communications*, 4:1474, 2013.
- [23] J. N. Coleman, M. Lotya, A. O'Neill, S. D. Bergin, P. J. King, U. Khan, K. Young, A. Gaucher, S. De, R. J. Smith, I. V. Shvets, S. K. Arora, G. Stanton, H. Kim, K. Lee, G. Kim, G. S. Duesberg, T. Hallam, J. J. Boland, J. J. Wang, J. F. Donegan, J. C. Grunlan, G. Moriarty, A. Shmeliov, R. J. Nicholls, J. M. Perkins, E. M. Grieveson, K. Theuwissen, D. W. McComb, P. D. Nellist, and V. Nicolosi. Two-dimensional nanosheets produced by liquid exfoliation of layered materials. *Science*, 331(6017):568–571, 2011.

- [24] D. R. Cooper, B. D'Anjou, N. Ghattamaneni, B. Harack, M. Hilke, A. Horth, N. Majlis, M. Massicotte, L. Vandsburger, E. Whiteway, and V. Yu. Experimental review of graphene. *ISRN Condensed Matter Physics*, 2012:56, 2012.
- [25] O. Kazakova, V. Panchal, and T. L. Burnett. Epitaxial graphene and graphene-based devices studied by electrical scanning probe microscopy. *Crystals*, 3(1):191–233, 2013.
- [26] SEM of CVD graphene. Accessed July 2013, http://www.products.cvdequipment.com/img/photos/cvdgraphene-cu-foil_1.png.
- [27] Y. Hernandez, V. Nicolosi, M. Lotya, F. M. Blighe, Z. Sun, S. De, I. McGovern, B. Holland, M. Byrne, Y. K. Gun'Ko, J. J. Boland, P. Niraj, G. Duesberg, S. Krishnamurthy, R. Goodhue, J. Hutchison, V. Scardaci, A. C. Ferrari, and J. N. Coleman. High-yield production of graphene by liquid-phase exfoliation of graphite. *Nature Nanotechnology*, 3(9):563–568, 2008.
- [28] K. V. Emtsev, A. Bostwick, K. Horn, J. Jobst, G. L. Kellogg, L. Ley, J. L. McChesney, T. Ohta, S. A. Reshanov, J. Rohrl, E. Rotenberg, A. K. Schmid, D. Waldmann, H. B. Weber, and T. Seyller. Towards wafer-size graphene layers by atmospheric pressure graphitization of silicon carbide. *Nature Materials*, 8(3):203–207, 2009.
- [29] A. Reina, X. Jia, J. Ho, D. Nezich, H. Son, V. Bulovic, M. S. Dresselhaus, and J. Kong. Large area, few-layer graphene films on arbitrary substrates by chemical vapor deposition. *Nano Letters*, 9(1):30–35, 2009.
- [30] Z. Li, P. Wu, C. Wang, X. Fan, W. Zhang, X. Zhai, C. Zeng, Z. Li, J. Yang, and J. Hou. Low-temperature growth of graphene by chemical vapor deposition using solid and liquid carbon sources. *ACS Nano*, 5(4):3385–3390, 2011.

- [31] J. W. Suk, A. Kitt, C. W. Magnuson, Y. Hao, S. Ahmed, J. An, A. K. Swan, B. B. Goldberg, and R. S. Ruoff. Transfer of CVD-grown monolayer graphene onto arbitrary substrates. *ACS Nano*, 5(9):6916–6924, 2011.
- [32] Y. Hernandez, M. Lotya, D. Rickard, S. D. Bergin, and J. N. Coleman. Measurement of multicomponent solubility parameters for graphene facilitates solvent discovery. *Langmuir*, 26(5):3208–3213, 2010.
- [33] A. O'Neill, U. Khan, P. N. Nirmalraj, J. J. Boland, and J. N. Coleman. Graphene dispersion and exfoliation in low boiling point solvents. *Journal of Physical Chemistry C*, 115(13):5422–5428, 2011.
- [34] J. N. Coleman. Liquid exfoliation of defect-free graphene. *Accounts of Chemical Research*, 46(1):14–22, 2013.
- [35] S. Park and R. S. Ruoff. Chemical methods for the production of graphenes. *Nature Nanotechnology*, 4(4):217–224, 2009.
- [36] Y. Dan, Y. Lu, N. J. Kybert, Z. Luo, and A. T. C. Johnson. Intrinsic response of graphene vapor sensors. *Nano Letters*, 9(4):1472–1475, 2009.
- [37] S. Forti, K. V. Emtsev, C. Coletti, A. A. Zakharov, C. Riedl, and U. Starke. Large-area homogeneous quasifree standing epitaxial graphene on SiC(0001): Electronic and structural characterization. *Physical Review B*, 84:125449, 2011.
- [38] A. N. Obraztsov. Chemical vapour deposition: Making graphene on a large scale. *Nature Nanotechnology*, 4(4):212–213, 2009.
- [39] O. Shenderova, D. Brenner, and R. S. Ruoff. Would diamond nanorods be stronger than fullerene nanotubes? *Nano Letters*, 3(6):805–809, 2003.
- [40] C. Lee, X. Wei, J.W. Kysar, and J. Hone. Measurement of the elastic properties and intrinsic strength of monolayer graphene. *Science*, 321(5887):385–388, 2008.

- [41] S. Ghosh, I. Calizo, D. Teweldebrhan, E. P. Pokatilov, D. L. Nika, A. A. Balandin, W. Bao, F. Miao, and C. N. Lau. Extremely high thermal conductivity of graphene: Prospects for thermal management applications in nanoelectronic circuits. *Applied Physics Letters*, 92(15):151911, 2008.
- [42] N. M. R. Peres. Graphene, new physics in two dimensions. *Europhysics News*, 40(3):17–20, 2009.
- [43] M. I. Katsnelson and K. S. Novoselov. Graphene: New bridge between condensed matter physics and quantum electrodynamics. *Solid State Communications*, 143(1-2):3–13, 2007.
- [44] P. Preuss. Surprising graphene. Accessed June 2013, <http://www.lbl.gov/Science-Articles/Archive/ALS-graphene.html>.
- [45] A. S. Mayorov, R. V. Gorbachev, S. V. Morozov, L. Britnell, R. Jalil, L. A. Ponomarenko, P. Blake, K. S. Novoselov, K. Watanabe, T. Taniguchi, and A. K. Geim. Micrometer-scale ballistic transport in encapsulated graphene at room temperature. *Nano Letters*, 11(6):2396–2399, 2011.
- [46] K. I. Bolotin, K. J. Sikes, Z. Jiang, M. Klima, G. Fudenberg, J. Hone, P. Kim, and H. L. Stormer. Ultrahigh electron mobility in suspended graphene. *Solid State Communications*, 146(9-10):351–355, 2008.
- [47] S. V. Morozov, K. S. Novoselov, M. I. Katsnelson, F. Schedin, D. C. Elias, J. A. Jaszczak, and A. K. Geim. Giant intrinsic carrier mobilities in graphene and its bilayer. *Physical Review Letters*, 100:016602, 2008.
- [48] M. A. Rafiee, J. Rafiee, Z. Wang, H. Song, Z. Z. Yu, and N. Koratkar. Enhanced mechanical properties of nanocomposites at low graphene content. *ACS Nano*, 3(12):3884–3890, 2009.
- [49] T. H. Han, Y. Lee, M. R. Choi, S. H. Woo, S. H. Bae, B. H. Hong, J. H. Ahn, and T. W. Lee. Extremely efficient flexible organic light-emitting diodes with modified graphene anode. *Nature Photonics*, 6(2):105–110, 2012.

- [50] K. J. Tielrooij, J. C. W. Song, S. A. Jensen, A. Centeno, A. Pesquera, A. Zurutuza Elorza, M. Bonn, L. S. Levitov, and F. H. L. Koppens. Photoexcitation cascade and multiple hot-carrier generation in graphene. *Nature Physics*, 9(4):248–252, 2013.
- [51] C. Ataca, E. Akturk, S. Ciraci, and H. Ustunel. High-capacity hydrogen storage by metallized graphene. *Applied Physics Letters*, 93(4):043123, 2008.
- [52] F. Schedin, A. K. Geim, S. V. Morozov, E. W. Hill, P. Blake, M. I. Katsnelson, and K. S. Novoselov. Detection of individual gas molecules adsorbed on graphene. *Nature Materials*, 6(9):652–655, 2007.
- [53] J. J. Yoo, K. Balakrishnan, J. Huang, V. Meunier, B. G. Sumpter, A. Srivastava, M. Conway, R. Mohana, L. Arava, J. Yu, R. Vajtai, and P. M. Ajayan. Ultrathin planar graphene supercapacitors. *Nano Letters*, 11(4):1423–1427, 2011.
- [54] L. Liao, Y. C. Lin, M. Bao, R. Cheng, J. Bai, Y. Liu, Y. Qu, K. L. Wang, Y. Huang, and X. Duan. High-speed graphene transistors with a self-aligned nanowire gate. *Nature*, 467(7313):305–308, 2010.
- [55] J. Zheng, L. Wang, R. Quhe, Q. Liu, H. Li, D. Yu, W. N. Mei, J. Shi, Z. Gao, and J. Lu. Sub-10 nm gate length graphene transistors: Operating at terahertz frequencies with current saturation. *Scientific Reports*, 3:1314, 2013.
- [56] S. H. M. Jafri, K. Carva, E. Widenkvist, T. Blom, B. Sanyal, J. Fransson, O. Eriksson, U. Jansson, H. Grennberg, O. Karis, R. A. Quinlan, B. C. Holloway, and K. Leifer. Conductivity engineering of graphene by defect formation. *Journal of Physics D-Applied Physics*, 43(4):045404, 2010.
- [57] R. Ansari, S. Ajori, and B. Motevalli. Mechanical properties of defective single-layered graphene sheets via molecular dynamics simulation. *Superlattices and Microstructures*, 51(2):274 – 289, 2012.

- [58] H. Feng, F. Daining, and X. Zhiping. Mechanical and thermal transport properties of graphene with defects. *Applied Physics Letters*, 99(4):041901, 2011.
- [59] M. M. Lucchese, F. Stavale, E. H. Martins, C. Vilani, M. V. O. Moutinho, R. B. Capaz, C. A. Achete, and A. Jorio. Quantifying ion-induced defects and raman relaxation length in graphene. *Carbon*, 48(5):1592 – 1597, 2010.
- [60] O. V. Yazyev and L. Helm. Defect-induced magnetism in graphene. *Physical Review B*, 75:125408, 2007.
- [61] X. Li, X. Wang, L. Zhang, S. Lee, and H. Dai. Chemically derived, ultrasmooth graphene nanoribbon semiconductors. *Science*, 319(5867):1229–1232, 2008.
- [62] F. Schwierz. Graphene transistors. *Nature Nanotechnology*, 5(7):487–496, 2010.
- [63] W. Y. Kim and K. S. Kim. Prediction of very large values of magnetoresistance in a graphene nanoribbon device. *Nature Nanotechnology*, 3(7):408–412, 2008.
- [64] D. Jiang, V. R. Cooper, and S. Dai. Porous graphene as the ultimate membrane for gas separation. *Nano Letters*, 9(12):4019–4024, 2009.
- [65] P. Reunchan and S. Jhi. Metal-dispersed porous graphene for hydrogen storage. *Applied Physics Letters*, 98(9):093103, 2011.
- [66] E. V. Castro, K. S. Novoselov, S. V. Morozov, N. M. R. Peres, J. M. B. Santos, J. Nilsson, F. Guinea, A. K. Geim, and A. H. C. Neto. Biased bilayer graphene: Semiconductor with a gap tunable by the electric field effect. *Physical Review Letters*, 99(21):216802, 2007.
- [67] O. Leenaerts, B. Partoens, and F. M. Peeters. Adsorption of H₂O, NH₃, CO, NO₂, and NO on graphene: A first-principles study. *Physical Review B*, 77(12):125416, 2008.

- [68] H. Pinto, R. Jones, J. P. Goss, and P. R. Briddon. *p*-type doping of graphene with F4-TCNQ. *Journal of Physics: Condensed Matter*, 21(40):402001, 2009.
- [69] H. E. Romero, N. Shen, P. Joshi, H. R. Gutierrez, S. A. Tadigadapa, J. O. Sofo, and P. C. Eklund. *n*-type behavior of graphene supported on Si/SiO₂ substrates. *ACS Nano*, 2(10):2037–2044, 2008.
- [70] V. A. Coleman, R. Knut, O. Karis, H. Grennberg, U. Jansson, R. Quinlan, B. C. Holloway, B. Sanyal, and O. Eriksson. Defect formation in graphene nanosheets by acid treatment: an X-ray absorption spectroscopy and density functional theory study. *Journal of Physics D: Applied Physics*, 41(6):062001, 2008.
- [71] D. Teweldebrhan and A. A. Balandin. Modification of graphene properties due to electron-beam irradiation. *Applied Physics Letters*, 94:013101, 2009.
- [72] J. D. Jones, P. A. Ecton, Y. Mo, and J. M. Perez. Comment on "modification of graphene properties due to electron-beam irradiation" [applied physics letters 94, 013101 (2009)]. *Applied Physics Letters*, 95(24):comments, 2009.
- [73] D. Teweldebrhan and A. A. Balandin. Response to "comment on 'modification of graphene properties due to electron-beam irradiation'[appl. phys. lett.[bold 95], 246101 (2009)]". *Applied Physics Letters*, 95(24):246102, 2009.
- [74] M. Stepanova and S. Dew, editors. *Nanofabrication: techniques and principles*, chapter Directions in Nanofabrication, pages 3–8. Springer, 2011.
- [75] L. Liu, S. M. Ryu, M. R. Tomasik, E. Stolyarova, N. Jung, M. S. Hybertsen, M. L. Steigerwald, L. E. Brus, and G. W. Flynn. Graphene oxidation: Thickness-dependent etching and strong chemical doping. *Nano Letters*, 8(7):1965–1970, 2008.

- [76] P. Nemes-Incze, G. Magda, K. Kamaras, and L. P. Biro. Crystallographically selective nanopatterning of graphene on SiO₂. *Nano Research*, 3(2):110–116, 2010.
- [77] R. F. Egerton, P. Li, and M. Malac. Radiation damage in the TEM and SEM. *Micron*, 35(6):399–409, 2004.
- [78] F. Banhart, J. Kotakoski, and A. V. Krasheninnikov. Structural defects in graphene. *ACS Nano*, 5(1):26–41, 2011.
- [79] A. W. Robertson, C. S. Allen, Y. A. Wu, K. He, J. Olivier, J. Neethling, A. I. Kirkland, and J. H. Warner. Spatial control of defect creation in graphene at the nanoscale. *Nature Communications*, 3:1144, 2012.
- [80] S. Liu, Q. Zhao, J. Xu, K. Yan, H. Peng, F. Yang, L. You, and D. Yu. Fast and controllable fabrication of suspended graphene nanopore devices. *Nanotechnology*, 23(8):085301, 2012.
- [81] N. Lu, J. Wang, H. C. Floresca, and M. J. Kim. In situ studies on the shrinkage and expansion of graphene nanopores under electron beam irradiation at temperatures in the range of 400 - 1200 C. *Carbon*, 50(8):2961 – 2965, 2012.
- [82] C. J. Russo and J. A. Golovchenko. Atom-by-atom nucleation and growth of graphene nanopores. *Proceedings of the National Academy of Sciences*, 109(16):5953–5957, 2012.
- [83] C. O. Girit, J. C. Meyer, R. Erni, M. D. Rossell, C. Kisielowski, L. Yang, C. H. Park, M. F. Crommie, M. L. Cohen, S. G. Louie, and A. Zettl. Graphene at the edge: Stability and dynamics. *Science*, 323(5922):1705–1708, 2009.
- [84] X. T. Jia, M. Hofmann, V. Meunier, B. G. Sumpter, J. Campos-Delgado, J. M. Romo-Herrera, H. B. Son, Y. P. Hsieh, A. Reina, J. Kong, M. Terrones,

- and M. S. Dresselhaus. Controlled formation of sharp zigzag and armchair edges in graphitic nanoribbons. *Science*, 323(5922):1701–1705, 2009.
- [85] Institute of Physics. Graphene nanoribbon edges. Accessed June 2013, <http://images.iop.org/objects/ntw/news/6/10/10/061010-2.jpg>.
- [86] Y. W. Son, M. L. Cohen, and S. G. Louie. Energy gaps in graphene nanoribbons. *Physical Review Letters*, 97:216803, 2006.
- [87] Z. H. Chen, Y. M. Lin, M. J. Rooks, and P. Avouris. Graphene nano-ribbon electronics. *Physica E-Low-Dimensional Systems & Nanostructures*, 40(2):228–232, 2007.
- [88] V. Barone, O. Hod, and G. E. Scuseria. Electronic structure and stability of semiconducting graphene nanoribbons. *Nano Letters*, 6(12):2748–2754, 2006.
- [89] X. Wang, Y. Ouyang, X. Li, H. Wang, J. Guo, and H. Dai. Room-temperature all-semiconducting sub-10-nm graphene nanoribbon field-effect transistors. *Physical Review Letters*, 100(20):206803, 2008.
- [90] L. Ci, Z. P. Xu, L. L. Wang, W. Gao, F. Ding, K. F. Kelly, B. I. Yakobson, and P. M. Ajayan. Controlled nanocutting of graphene. *Nano Research*, 1(2):116–122, 2008.
- [91] L. C. Campos, V. R. Manfrinato, J. D. Sanchez-Yamagishi, J. Kong, and P. Jarillo-Herrero. Anisotropic etching and nanoribbon formation in single-layer graphene. *Nano Letters*, 9(7):2600–2604, 2009.
- [92] N. G. Chopra, L. X. Benedict, V. H. Crespi, M. L. Cohen, S. G. Louie, and A. Zettl. Fully collapsed carbon nanotubes. *Nature*, 377(6545):135–138, 1995.
- [93] L. Jiao, L. Zhang, X. Wang, G. Diankov, and H. Dai. Narrow graphene nanoribbons from carbon nanotubes. *Nature*, 458(7240):877–880, 2009.

- [94] D. V. Kosynkin, A. L. Higginbotham, A. Sinitskii, J. R. Lomeda, A. Dimiev, B. K. Price, and J. M. Tour. Longitudinal unzipping of carbon nanotubes to form graphene nanoribbons. *Nature*, 458(7240):872–876, 2009.
- [95] W. S. Hwang, K. T., X. Li, H. Xing, A. C. Seabaugh, C. Y. Sung, and D. Jena. Transport properties of graphene nanoribbon transistors on chemical-vapor-deposition grown wafer-scale graphene. *Applied Physics Letters*, 100(20):203107, 2012.
- [96] A. E. Grigorescu and C. W. Hagen. Resists for sub-20-nm electron beam lithography with a focus on HSQ: state of the art. *Nanotechnology*, 20(29):292001, 2009.
- [97] D. Winston, B. M. Cord, B. Ming, D. C. Bell, W. F. DiNatale, L. A. Stern, A. E. Vladar, M. T. Postek, M. K. Mondol, J. K. W. Yang, and K. K. Berggren. Scanning-helium-ion-beam lithography with hydrogen silsesquioxane resist. volume 27, pages 2702–2706. American Vacuum Society, 2009.
- [98] D. Maas, E. van Veldhoven, P. Chen, V. Sidorkin, H. Salemink, E. van der Drift, and P. Alkemade. Nanofabrication with a helium ion microscope. *Proceedings of SPIE*, 7638:763814, 2010.
- [99] E. Drift and D. J. Maas. *Helium Ion Lithography*, pages 93–116. Springer, 2012.
- [100] W. D. Li, W. Wu, and R. S. Williams. Combined helium ion beam and nanoimprint lithography attains 4 nm half-pitch dense patterns. *Journal of Vacuum Science & Technology B*, 30(6):06F304, 2012.
- [101] L. Tapasztó, G. Dobrik, P. Lambin, and L. P. Biro. Tailoring the atomic structure of graphene nanoribbons by scanning tunnelling microscope lithography. *Nature Nanotechnology*, 3(7):397–401, 2008.

- [102] G. Dobrik, L. Tapaszto, P. Nemes-Incze, P. Lambin, and L. P. Biro. Crystallographically oriented high resolution lithography of graphene nanoribbons by stm lithography. *Physica Status Solidi (b)*, 247(4):896–902, 2010.
- [103] D. Fox, Y. B. Zhou, A. O’Neill, S. Kumar, J. J. Wang, J. N. Coleman, G. S. Duesberg, J. F. Donegan, and H. Z. Zhang. Helium ion microscopy of graphene: beam damage, image quality and edge contrast. *Nanotechnology*, 24(33):335702, 2013.
- [104] M. D. Fischbein and M. Drndic. Electron beam nanosculpting of suspended graphene sheets. *Applied Physics Letters*, 93(11):113107, 2008.
- [105] A. W. Robertson and J. H. Warner. Atomic resolution imaging of graphene by transmission electron microscopy. *Nanoscale*, 5:4079–4093, 2013.
- [106] D. Pickard and L. Scipioni. Graphene nano-ribbon patterning in the orion plus, 2009. Accessed June 2013, http://www.tcd.ie/Physics/people/HongZhou.Zhang/Teaching/PY5019/HIM/AN_ORION_PLUS_Graphene.pdf.
- [107] M. C. Lemme, D. C. Bell, J. R. Williams, L. A. Stern, B. W. H. Baugher, P. Jarillo-Herrero, and C. M. Marcus. Etching of graphene devices with a helium ion beam. *ACS Nano*, 3(9):2674–2676, 2009.
- [108] D. C. Bell, M. C. Lemme, L. A. Stern, J. R. Williams, and C. M. Marcus. Precision cutting and patterning of graphene with helium ions. *Nanotechnology*, 20:455301, 2009.
- [109] D. Pickard, B. Oezylmaz, J. Thong, K. P. Loh, V. Viswanathan, A. Zhongkai, S. Mathew, T. Kundu, C. Park, and Z. Yi. Graphene nanoribbons fabricated by helium ion microscope. *Bulletin of the American Physical Society*, 55, 2010.
- [110] L. Scipioni. Nano-machining of graphene in the orion plus, 2009. Accessed June 2013, <http://www.tcd.ie/Physics/people/HongZhou.Zhang/>

- Teaching/PY5019/HIM/Nano-Machining_of_Graphene_in_the_ORION_PLUS.pdf.
- [111] J. Yang, D. C. Ferranti, L. A. Stern, C. A. Sanford, J. Huang, Z. Ren, L. C. Qin, and A. R. Hall. Rapid and precise scanning helium ion microscope milling of solid-state nanopores for biomolecule detection. *Nanotechnology*, 22(28):285310, 2011.
- [112] Y. Zhou and K. P. Loh. Making patterns on graphene. *Advanced Materials*, 22(32):3615–3620, 2010.
- [113] M. Nastasi, J. W. Mayer, and J. K. Hirvonen. *Ion-Solid Interactions: Fundamentals and Applications*, chapter Dynamics of binary elastic collisions, page 48. Cambridge University Press, 1996.
- [114] J. Goldstein, D. E. Newbury, D. C. Joy, C. E. Lyman, P. Echlin, E. Lifshin, L. Sawyer, and J.R. Michael. *Scanning Electron Microscopy and X-Ray Microanalysis*, volume 1, chapter Electron Beam-Specimen Interactions, pages 63–65. Springer, 3rd edition, 2003.
- [115] P. Hovongton and D. Drouin. monte CARlo SIMulation of electroN trajectory in sOlids. Accessed June 2013, <http://www.gel.usherbrooke.ca/casino/index.html>.
- [116] Y. K. Kim and M. E. Rudd. Binary-encounter-dipole model for electron-impact ionization. *Physical Review A*, 50(5):3954, 1994.
- [117] W. Hwang, Y. K. Kim, and M. E. Rudd. New model for electron-impact ionization cross sections of molecules. *The Journal of Chemical Physics*, 104(8):2956–2966, 1996.
- [118] ImageJ homepage. Accessed July 2013, <http://rsbweb.nih.gov/ij/>.
- [119] L. Gianuzzi and F. A. Stevie. *Introduction to Focused Ion Beams*, chapter The Basic FIB Instrument, page 7. Springer, 2006.

- [120] J. Orloff, L. W. Swanson, and M. W. Utlaut. *High Resolution Focused Ion Beams: FIB and Its Applications : The Physics of Liquid Metal Ion Sources and Ion Optics and Their Application to Focused Ion Beam Technology*, chapter Field ionisation sources, pages 5 – 20. Springer, 2003.
- [121] S. Khizroev and D. Litvinov. Focused-ion-beam-based rapid prototyping of nanoscale magnetic devices. *Nanotechnology*, 15(3):R7, 2004.
- [122] James Ziegler. SRIM. Accessed June 2013, <http://www.srim.org/>.
- [123] R. Ramachandra. *A Study of Helium Ion Induced Secondary Electron Production*. PhD thesis, University of Tennessee, 2009.
- [124] D. Cohen-Tanugi and N. Yao. Superior imaging resolution in scanning helium-ion microscopy: A look at beam-sample interactions. *Journal of Applied Physics*, 104(6):063504, 2008.
- [125] M. Nastasi, J. W. Mayer, and J. K. Hirvonen. *Ion-Solid Interactions: Fundamentals and Applications*, chapter Cross-section, pages 62–87. Cambridge University Press, 1996.
- [126] D.B. Williams and C.B. Carter. *The Transmission Electron Microscope*, chapter 1, page 11. Springer, 2009.
- [127] J. Goldstein, D. E. Newbury, D. C. Joy, C. E. Lyman, P. Echlin, E. Lifshin, L. Sawyer, and J.R. Michael. *Scanning Electron Microscopy and X-Ray Microanalysis*, volume 1, chapter The SEM and its modes of operation, pages 21–60. Springer, 3rd edition, 2003.
- [128] H. Seiler. Secondary electron emission in the scanning electron microscope. *Journal of Applied Physics*, 54(11):R1–R18, 1983.
- [129] R. Hessel and B. Gross. Escape depth of secondary electrons from electron-irradiated polymers. *Electrical Insulation, IEEE Transactions on*, 27(4): 831–834, 1992.

- [130] D. B. Williams and C. B. Carter. *The Instrument*, chapter 9, pages 141 – 171. Springer, 2nd edition, 2009.
- [131] P. Schlossmacher, C. Kuebel, B. Freitag, D. Hubert, and R. Perquin. New developments in focal-series reconstruction. *Microscopy and Microanalysis*, 13 (SupplementS02):1170–1171, 2007.
- [132] S. Bals, S. V. Aert, G. V. Tendeloo, D. V. Dyck, A. Acute, and D. Vila Brande. Statistical estimation of oxygen atomic positions with sub angstrom precision from exit wave reconstruction. *Microscopy and Microanalysis*, 11 (SupplementS02):556–557, 2005.
- [133] D. B. Williams and C. B. Carter. *Amplitude Contrast*, chapter 22, pages 371–388. Springer, 2 edition, 2009.
- [134] Z. Y. Li, J. Yuan, Y. Chen, R. E. Palmer, and J. P. Wilcoxon. Direct imaging of core-shell structure in silver-gold bimetallic nanoparticles. *Applied Physics Letters*, 87(24):243103–243103–3, 2005.
- [135] T. C. Lovejoy, Q. M. Ramasse, M. Falke, A. Kaeppel, R. Terborg, R. Zan, N. Dellby, and O. L. Krivanek. Single atom identification by energy dispersive X-ray spectroscopy. *Applied Physics Letters*, 100(15):154101, 2012.
- [136] R. F. Egerton. *Electron Energy-Loss Spectroscopy in the Electron Microscope*, chapter 1, pages 1–110. Springer, 3 edition, 2011.
- [137] M. Boese, S. Kumar, A. O’Neill, M. Lotya, H. Z. Zhang, J. N. Coleman, and G. S. Duesberg. A simple method to measure graphite thickness with monolayer precision using plasmon energy loss imaging. *Microscopy and Microanalysis*, 16(SupplementS2):1540–1541, 2010.
- [138] R. Brydson. *Electron Energy Loss Spectrometry and Energy Dispersive X-ray Analysis*, chapter Elemental Analysis and Quantification using EDX. Wiley, 2011.

- [139] Y. Petrov and O. Vyvenko. Secondary electron emission spectra and energy selective imaging in helium ion microscope. In *Society of Photo-Optical Instrumentation Engineers (SPIE) Conference Series*, volume 8036 of *Society of Photo-Optical Instrumentation Engineers (SPIE) Conference Series*, May 2011. doi: 10.1117/12.886347.
- [140] Ranjan Ramachandra, Brendan Griffin, and David Joy. A model of secondary electron imaging in the helium ion scanning microscope. *Ultramicroscopy*, 109(6):748–757, 2009.
- [141] C. Rodenburg, X. Liu, M. A. E. Jepson, Z. Zhou, W. M. Rainforth, and J. M. Rodenburg. The role of helium ion microscopy in the characterisation of complex three-dimensional nanostructures. *Ultramicroscopy*, 110(9):1178–1184, 2010.
- [142] A. C. Ferrari and D. M. Basko. Raman spectroscopy as a versatile tool for studying the properties of graphene. *Nature Nanotechnology*, 8(4):235–246, 2013.
- [143] A. C. Ferrari, J. C. Meyer, V. Scardaci, C. Casiraghi, M. Lazzeri, F. Mauri, S. Piscanec, D. Jiang, K. S. Novoselov, S. Roth, and A. K. Geim. Raman spectrum of graphene and graphene layers. *Physical Review Letters*, 97:187401, 2006.
- [144] L. G. Cancado, A. Jorio, E. H. M. Ferreira, F. Stavale, C. A. Achete, R. B. Capaz, M. V. O. Moutinho, A. Lombardo, T. S. Kulmala, and A. C. Ferrari. Quantifying defects in graphene via raman spectroscopy at different excitation energies. *Nano Letters*, 11(8):3190–3196, 2011.
- [145] W. Wu, Q. Yu, P. Peng, Z. Liu, J. Bao, and S. Pei. Control of thickness uniformity and grain size in graphene films for transparent conductive electrodes. *Nanotechnology*, 23(3):035603, 2012.

- [146] L. Reimer and H. Kohl. *Calculation of Specimen Temperature*, chapter 11, pages 463–466. Springer, 5th edition, 2008.
- [147] H. W. Goldstein. The reaction of active nitrogen with graphite. *Journal of Physical Chemistry*, 68(1):39–42, 1964.
- [148] S. Kumar, E. Rezvani, V. Nicolosi, and G. S. Duesberg. Graphene resist interlacing process for versatile fabrication of free-standing graphene. *Nanotechnology*, 23(14):145302, 2012.
- [149] J. Fan, J. M. Michalik, L. Casado, S. Roddaro, M. R. Ibarra, and J. M. De Teresa. Investigation of the influence on graphene by using electron-beam and photo-lithography. *Solid State Communications*, 151(21):1574–1578, 2011.
- [150] N. Peltekis, S. Kumar, N. McEvoy, K. Lee, A. Weidlich, and G. S. Duesberg. The effect of downstream plasma treatments on graphene surfaces. *Carbon*, 50(2):395–403, 2012.
- [151] A. C. Ferrari. Raman spectroscopy of graphene and graphite: Disorder, electron-phonon coupling, doping and nonadiabatic effects. *Solid State Communications*, 143(1-2):47–57, 2007.
- [152] J. F. Ziegler, J. P. Biersack, and M. D. Ziegler. *Stopping and range of ions in matter*. SRIM Co., 2008.
- [153] K. Ohya, T. Yamanaka, K. Inai, and T. Ishitani. Comparison of secondary electron emission in helium ion microscope with gallium ion and electron microscopes. *Nuclear Instruments and Methods in Physics Research Section B: Beam Interactions with Materials and Atoms*, 267(4):584–589, 2009.
- [154] M.T. Postek, A. Vladar, C. Archie, and B. Ming. Review of current progress in nanometrology with the helium ion microscope. *Measurement Science and Technology*, 22:024004, 2011.

- [155] J. Kotakoski, D. Santos-Cottin, and A. V. Krashennnikov. Stability of graphene edges under electron beam: Equilibrium energetics versus dynamic effects. *ACS Nano*, 6(1):671–676, 2012.
- [156] C. Lee, H. Yan, L. E. Brus, T. F. Heinz, J. Hone, and S. Ryu. Anomalous lattice vibrations of single- and few-layer MoS₂. *ACS Nano*, 4(5):2695–2700, 2010.
- [157] A. Tseng. *Nanofabrication: Fundamentals and Applications*, chapter Focused Ion Beams and Interactions with Solids, pages 431–465. World Scientific, 2008.
- [158] F. Borrnert, S. M. Avdoshenko, A. Bachmatiuk, I. Ibrahim, B. Buchner, G. Cuniberti, and M. H. Rummeli. Amorphous carbon under 80 kV electron irradiation: A means to make or break graphene. *Advanced Materials*, 24(41):5630–5635, 2012.
- [159] H. J. Na, J. W. Lee, W. K. Lee, J. H. Lim, H. G. Park, B. Y. Kim, J. Y. Hwang, J. M. Han, and D. S. Seo. Titanium dioxide surface modification via ion-beam bombardment for vertical alignment of nematic liquid crystal. *Optics Letters*, 35(8):1151–1153, 2010.
- [160] A. Colli, A. Fasoli, C. Ronning, S. Pisana, S. Piscanec, and A. C. Ferrari. Ion beam doping of silicon nanowires. *Nano Letters*, 8(8):2188–2193, 2008.
- [161] B. Panigrahy, M. Aslam, and D. Bahadur. Controlled optical and magnetic properties of ZnO nanorods by Ar ion irradiation. *Applied Physics Letters*, 98(18):183109–3, 2011.
- [162] K. K. H. Wong, J. L. Hutter, M. Zinke-Allmang, and W. Wan. Physical properties of ion beam treated electrospun poly(vinyl alcohol) nanofibers. *European Polymer Journal*, 45(5):1349–1358, 2009.

- [163] V. Raffa, O. Vittorio, V. Pensabene, A. Menciassi, and P. Dario. FIB-nanostructured surfaces and investigation of bio/nonbio interactions at the nanoscale. *NanoBioscience, IEEE Transactions on*, 7(1):1–10, 2008.
- [164] R. Wirth. Focused ion beam (FIB) combined with SEM and TEM: Advanced analytical tools for studies of chemical composition, microstructure and crystal structure in geomaterials on a nanometre scale. *Chemical Geology*, 261(3-4):217–229, 2009.
- [165] D. Kiener, C. Motz, M. Rester, M. Jenko, and G. Dehm. FIB damage of Cu and possible consequences for miniaturized mechanical tests. *Materials Science & Engineering A*, 459(1–2):262–272, 2007.
- [166] C. Genet and T. W. Ebbesen. Light in tiny holes. *Nature*, 445(7123):39–46, 2007.
- [167] C. Yuan and Z. Xiaowen. Focused ion beam technology and application in failure analysis. In *Electronic Packaging Technology & High Density Packaging (ICEPT-HDP), 11th International Conference on*, pages 957–960, 2010.
- [168] N. Toshima and T. Yonezawa. Bimetallic nanoparticles-novel materials for chemical and physical applications. *New Journal of Chemistry*, 22(11):1179–1201, 1998.
- [169] R. Verre, K. Fleischer, R. G. S. Sofin, N. McAlinden, J. F. McGilp, and I. V. Shvets. *In situ* characterization of one-dimensional plasmonic Ag nanocluster arrays. *Physical Review B*, 83(12):125432, 2011.
- [170] R. Verre, K. Fleischer, J. F. McGilp, D. Fox, G. Behan, H. Zhang, and I. V. Shvets. Controlled in situ growth of tunable plasmonic self-assembled nanoparticle arrays. *Nanotechnology*, 23(3):035606, 2012.
- [171] D. Fox, R. Verre, B. J. O’Dowd, S. K. Arora, C. C. Faulkner, I. V. Shvets, and H. Z. Zhang. Investigation of coupled cobalt–silver nanoparticle system

- by plan view TEM. *Progress in Natural Science: Materials International*, 22(3):186–192, 2012.
- [172] M. J. Suess, E. Mueller, and R. Wepf. Minimization of amorphous layer in Ar⁺ ion milling for UHR-EM. *Ultramicroscopy*, 111(8):1224 – 1232, 2011.
- [173] C. W. Lee, Y. Ikematsu, and D. Shindo. Measurement of mean free paths for inelastic electron scattering of Si and SiO₂. *Journal of Electron Microscopy*, 51(3):143–148, 2002.
- [174] L. A. Giannuzzi, R. Geurts, and J. Ringnalda. 2 keV Ga⁺ FIB milling for reducing amorphous damage in silicon. *Microscopy and Microanalysis*, 11 (Supplement 02):828–829, 2005.
- [175] R. F. Egerton. *Applications of Energy-Loss Spectroscopy*, chapter 5. Plenum Publishing Corporation, New York, 1996.
- [176] R. Siegele, G. C. Weatherly, H. K. Haugen, D. J. Lockwood, and L. M. Howe. Helium bubbles in silicon: Structure and optical properties. *Applied Physics Letters*, 66(11):1319–1321, 1995.
- [177] D. A. Muller. Crystalline and amorphous silicon (Si) spectrum. Accessed June 2013. http://muller.research.engineering.cornell.edu/sites/WEELS/View/Si_c-Si_a-Si.html.
- [178] Y. Yan, M. Page, T. H. Wang, M. M. Al-Jassim, H. M. Branz, and Q. Wang. Atomic structure and electronic properties of c-Si/a-Si:H heterointerfaces. *Applied Physics Letters*, 88(12):121925–3, 2006.
- [179] D. Borah, M. T. Shaw, S. Rasappa, R. A. Farrell, C. O'Mahony, C. C. Faulkner, M. Bose, P. Gleeson, J. D. Holmes, and M. A. Morris. Plasma etch technologies for the development of ultra-small feature size transistor devices. *Journal of Physics D: Applied Physics*, 44(17):174012, 2011.

- [180] J. G. Son, J. B. Chang, K. K. Berggren, and C. A. Ross. Assembly of sub-10-nm block copolymer patterns with mixed morphology and period using electron irradiation and solvent annealing. *Nano Letters*, 11(11):5079–5084, 2011.
- [181] C. C. Faulkner, D. A. Allwood, and R. P. Cowburn. Tuning of biased domain wall depinning fields at permalloy nanoconstrictions. *Journal of Applied Physics*, 103(7):073914, 2008.
- [182] N. Li, E. G. Fu, H. Wang, J. J. Carter, L. Shao, S. A. Maloy, A. Misra, and X. Zhang. He ion irradiation damage in Fe/W nanolayer films. *Journal of Nuclear Materials*, 389:233–238, 2009.
- [183] J. A. Sundararajan, D. T. Zhang, Y. Qiang, W. Jiang, and J. S. McCloy. Magnetic stability of He⁺ ion irradiated FeO + Fe₃N granular films. *Journal of Applied Physics*, 109(7):07E324–3, 2011.
- [184] D. S. Jun, V. G. Kutchoukov, and P. Kruit. Ion beams in SEM: An experiment towards a high brightness low energy spread electron impact gas ion source. *Journal of Vacuum Science & Technology B: Microelectronics and Nanometre Structures*, 29(6):06F603, 2011.
- [185] R. Hill, J. Notte, and B. Ward. The ALIS He ion source and its application to high resolution microscopy. *Physics Procedia*, 1:135–141, 2008.

Abstract

Modification and Analysis of Layered Materials with Charged Particle Beams

Daniel Fox

In this work the controlled modification of 2D nanomaterials in order to tune their structure and control their geometry was demonstrated. This was achieved using a range of highly focused beams of electrons and ions.

The localised generation of nanopores within a sample using electron-beam activated gas etching was first described. The material used was graphene, a honeycomb lattice of carbon just one atom thick. A model of the etching was developed. Systematic investigations of the effect of the various parameters in the system were used to support the model. Structural modification of graphene was then demonstrated using a focused beam of helium ions (He^+). Raman spectroscopy was used to correlate the ion irradiation parameters with the sample damage. It was found that a desired density of defects can be introduced into graphene by this method. He^+ irradiation was also shown to be capable of fabricating nanostructures within graphene flakes.

The He^+ fabrication was then extended to thin (<3 layer) flakes of molybdenum disulfide (MoS_2). The irradiation of MoS_2 was modelled and this data was used to design an experiment. The experiment showed that nanostructures can be milled into these flakes. The damage produced at the edges of the milled features was investigated by high resolution scanning transmission electron microscopy (STEM). It was found that the extent of the damage can be controlled such that no observable edge damage was created. The nanostructures milled within the MoS_2 flakes were then filled with carbon and annealed with an electron beam. This shows that it is possible to use this technique to create unique new heterostructures.

Finally, the ion beam-induced modification technique was extended to a 3D material system. A focused beam of gallium ions was used to tailor the geometry of a section of silicon. This was shown to have applications in the preparation of samples for transmission electron microscopy (TEM). A He^+ beam was then used to provide further sample modification control, producing samples that reveal smaller feature sizes during TEM observation and less beam-induced damage than can be achieved by a gallium ion beam alone.